Torkan Shafighfard, M.Sc. Eng.

DIAGNOSTIC METHODS FOR FIBER REINFORCED COMPOSITE STRUCTURES WITH IMPERFECTIONS

A dissertation submitted to the Scientific Board of the Szewalski Institute of Fluid-Flow Machinery, Polish Academy of Sciences in partial fulfillment of the requirements for the Degree of Doctor of Philosophy

Supervisor:
Magdalena Mieloszyk, D.Sc. Ph.D. Eng.

September 2023

DEDICATION:

To Pain

ACKNOWLEDGEMENTS

I would like to express my gratitude to my thesis advisor DSc PhD Eng Magdalena Mieloszyk for the continuous support of my Ph.D. study and research guidance. I am thankful for all the opportunities that IMP PAN has provided which helped me to learn the research principles thoroughly. It was a great opportunity for me to work at IMP PAN, Gdansk, Poland and I would like to thank the IMP PAN Directors helped me finish my Ph.D. in its utmost excellence and made contribution to scientific society with several peer-reviewed high quality published papers.

Furthermore, I want to kindly acknowledge composite technologies center of excellence in Istanbul, Turkey (KORDSA) for providing materials and experimental tools for some parts of analysis conducted in this study. Besides, I would appreciate the jury members for giving their precious time for reviewing my work and providing feedback to improve this thesis.

The research presented in the thesis was partially supported by the following projects: 'Additive manufactured composite smart structures with embedded fibre Bragg grating sensors (AMCSS)' funded by the National Science Centre, Poland under M-ERA.NET 2 Call 2019, grant agreement 2019/01/Y/ST8/00075. Also, I would like to to acknowledge the partial support from the scientific and technological research council of Türkiye (TÜBİTAK) through project number 217.M211 for preparing samples utilized in second and third chapter of this thesis.

Also, I send my warm and kind words towards my family for providing me with continuous encouragement throughout my years of study. Foremost, I would express my profound gratitude to my spouse, Rana, for her support and believe that this achievement would not have been possible without her.

ABSTRACT

This thesis was intended to analyse diagnostic techniques for carbon fibre reinforced polymer (CFRP) structures with imperfections in order to explore the possible application of these materials in industry. The analysed structures have imperfections understood as voids, gaps between fibre bundles, delaminations, holes, etc. or inclusions in the form of embedded optical fibres with fibre Bragg grating (FBG) sensors. Such imperfections can be related to the manufacturing method features (e.g. voids in additive manufactured (AM) structure) or inclusions introduced intentionally (e.g. optical fibres) or the geometric characteristics of the structure (e.g. holes). All of the elements result in local stress/strain concentration, and changes in material mechanical and material properties that influence their degradation processes

The first part of this thesis aimed to determine the thermo-mechanic characteristics of CFRP samples with embedded FBG sensors fabricated by green method of manufacturing, 3D printing. Additionally, the influence of embedded FBG sensors on the mechanical strength of CFRP material was evaluated based on the tensile test results. This section included both numerical and experimental investigations. The second section was the investigation of the effect of drilling two holes in different configurations on the mechanical behaviour of plain weave composite structures. This part was mostly experimental, though a numerical analysis was also conducted for verification of the numerical model utility. The final part, which was a comparative study, was devoted to studying the application of machine learning (ML) algorithms on the prediction of the degradation process of the plain weave composites with different stacking sequences and two interacting holes.

A novelty in AM structures with embedded FBG sensors is related to the embedding process and application of the sensors for strain measurements of elements subjected to thermal and mechanical loading. Numerical simulation was conducted inside ABAQUS finite element method (FEM) software to complement numerous experimental investigations to verify the computational results for the samples under thermal loading. The numerical works results were in good agreement with the outcomes given by FBG sensors. Embedded FBG sensors were able to identify thermal strain accurately for additively manufactured composite structures. Additionally, the tensile test was performed on the samples exposed to elevated and sub-zero temperatures. The aim of the test was to determine the influence of embedded optical fibres on mechanical strength of the CFRP material. FBG sensors were also applied for strain measurements during the test. The achieved results were compared to strain values determined by the tensile machine with a good agreement between the methods. This AM method can be applied for fabrication elements with embedded FBG sensors also using the other fibre reinforcement material. Ad-

ditionally, FBG sensors can be used for strain measurements during both thermal and mechanical loadings.

Plain weave composite is a long-lasting type of fabric composite that is stable enough when being handled. On the other hand, composite laminates with notches have been employed in various industrial applications, e.g., swash plates, adaptor plates, and repair patches. These holes reduce the structural integrity of the composite structures. In woven composite laminate with two interacting circular cut-outs, the hole configurations influences the strength and stress concentration factor (SCF) of that structure. Drilling one notch in the loading direction improved the structural behavior of plain-weave composite structures as also observed by the SCF analysis through FEM. The main aim is to investigate, experimentally and numerically, the interaction between two notches in different configurations while the composite laminate was under tension. The location of the processing zone (the location of failure initiation) depends upon the orientation of the holes. The characteristic distance and processing zone for each specimen were identified for each sample integrating the FEM and Digital Image Correlation (DIC) method. Point stress criterion (PSC) and Extended-PSC (EPSC) approaches were employed to predict the failure strength of each specimen. The failure initiation and progression with through the interaction between two notches was studied via infrared thermography (IRT). Furthermore, IRT results were complemented through fractographic analysis and the type of fracture for each sample was discussed in detail.

Finally, composites with hole/s have been extensively employed in industry, though they have weak structural performance and complex design processes. Numerous number of geometry/material parameters have been used for designing composites with holes. Thus, an efficient computational tool is essential for prediction of the structures. Various ML approaches were developed to achieve the model with highest accuracy taking into account the maximum tensile stress of composite plates with two interacting holes. Also, the effectiveness of each technique was discussed. FEM simulations were performed through ABAQUS software integrating with the python macro code to provide a data-rich framework (8960 data). The predictions obtained through ML methods were compared with those extracted by the FEM simulations. An evolutionary algorithm (TPOT) and automatic neural network search (AuoKeras) were employed for predicting the tensile stress appeared in the vicinity of the holes. An automatic grid search method was employed to choose the most efficient method capable of predicting the material attribute target values (maximum stress) for different tests. Stacked model did provide the most accurate predictions among other techniques. The applicability of stacked algorithm in other composite materials was discussed.

Following an introductory chapter and a review of the state-of-the-art (Chapters 1-2), I am discussing my contribution to the field in Chapters 3-5, which consists of:

- determination of the possibility of embedding FBG sensors into CFRP samples fabricated using additive manufacturing technique – FDM

- determination of the diagnostic method for CFRP structures based on embedded FBG sensors including the analyses of the influence of the embedded optical fibres on the mechanical strength of the samples

- development of a numerical model of FRP structure with holes under loading

- application of theoretical models for strength prediction of woven structures with holes

- analysis of the degradation processes of FRP structures (AM with embedded FBG sensors and woven with holes) and determination of the dominant type (matrix cracking, fibre breaking, etc.)

- developing a novel method to accurately predict the maximum tensile stress of the woven composites with interacting holes under tension

The summary, conclusion, and future works required for further development of this thesis are discussed thoroughly in Chapter 6.

The results of the performed analyses can be also extended to the other types of fibre reinforcement used in FRP elements.

PUBLICATIONS

Journal Papers:

- Shafighfard, Torkan, and Magdalena Mieloszyk. "Model of the temperature influence on additively manufactured carbon fibre reinforced polymer samples with embedded fibre bragg grating sensors." Materials 15, no. 1 (2021): 222.
- Shafighfard, Torkan, and Faramarz Bagherzadeh. "Ensemble Machine Learning approach for evaluating the material characterization of carbon nanotube-reinforced cementitious composites." Case Studies in Construction Materials 17 (2022): e01537.
- Shafighfard, Torkan, and Magdalena Mieloszyk. "Experimental and numerical study of the additively manufactured carbon fibre reinforced polymers including fibre Bragg grating sensors." Composite Structures 299 (2022): 116027.
- Shafighfard, Torkan, Faramarz Bagherzadeh, Rana Abdollahi Rizi, and Doo-Yeol Yoo. "Data-driven compressive strength prediction of steel fiber reinforced concrete (SFRC) subjected to elevated temperatures using stacked machine learning algorithms." Journal of Materials Research and Technology 21 (2022): 3777-3794.
- Adibimanesh, Behrouz, Sylwia Polesek-Karczewska, Faramarz Bagherzadeh, Piotr Szczuko, and Torkan Shafighfard. "Energy consumption optimization in wastewater treatment plants: machine learning for monitoring incineration of sewage sludge." Sustainable Energy Technologies and Assessments 56 (2023): 103040.
- Khan, Raja Muhammad Awais, Torkan Shafighfard, Hafiz Qasim Ali, Magdalena Mieloszyk, and Mehmet Yildiz. "Strength prediction and experimental damage investigations of plain woven CFRPs with interacting holes using multi-instrument measurements." Polymer Composites (2023).
- Bagherzadeh, Faramarz, Torkan Shafighfard, Raja Muhammad Awais Khan, Piotr Szczuko, and Magdalena Mieloszyk. "Prediction of maximum tensile stress in plain-weave composite laminates with interacting holes via stacked

machine learning algorithms: A comparative study." Mechanical Systems and Signal Processing 195 (2023): 110315.

- Torkan Shafighfard, Faramarz Bagherzadeh, Magdalena Mieloszyk, Doo-Yeol Yoo. Chained machine learning model for predicting load capacity and ductility of steel fiber-reinforced concrete beams (Computer-Aided Civil and Infrastructure Engineering, revised version review)

- Torkan Shafighfard, Farzin Kazemi, and Doo-Yeol Yoo. Stacked machine learning-based model for estimating compressive strength, cost, and carbon emission of high-performance alkali-activated concrete (Cement and Concrete Composites, under review)

- Farzin Kazemi, Torkan Shafighfard, Robert Jankowski, and Doo-Yeol Yoo. Data-driven predictions of compressive strength of alkali-activated ultra-high performance concrete: a comparative study (Expert systems with applications, under review)

- Torkan Shafighfard, Farzin Kazemi, and Doo-Yeol Yoo. Machine learning-based prediction for pull-out behavior of steel fibers from concrete (Construction and Building Materials, under review)

- Farzin Kazemi, Torkan Shafighfard, and Doo-Yeol Yoo. Data-driven modeling of different mechanical properties of fiber-reinforced concrete: A critical review (Archives of Computational Methods in Engineering, revised version review)

Book chapters:

- Mieloszyk, Magdalena, Torkan Shafighfard, Katarzyna Majewska, and Artur Andrearczyk. "An Influence of Temperature on Fiber Bragg Grating Sensor Embedded into Additive Manufactured Structure." In European Workshop on Structural Health Monitoring, pp. 495-501. Cham: Springer International Publishing, 2022.

Conference papers:

- Torkan Shafighfard, Mieloszyk, Magdalena, "Influence of Temperature on FBG Sensor Embedded into Additive Manufactured Structure." In European Workshop on Structural Health Monitoring (EWSHM 2022189, Palermo, Italy)

- Torkan Shafighfard, Mieloszyk, Magdalena, Experimental and numerical study of the additively manufactured CFRPs embedded fibre Bragg grating sensors, ICCS24-24th International Conference on Composite Structures, Lisbon, Portugal

TABLE OF CONTENTS

LIST OF TABLES

LIST OF FIGURES

LIST OF ABBREVIATIONS

AI ARTIFICIAL INTELLIGENCE 4, 22

AM ADDITIVE MANUFACTURING 3, 9, 11, 16, 48

ANN ARTIFICIAL NEURAL NETWORK 24

CFRP CARBON FIBER REINFORCED POLYMERS .. viii, ix, x, 5, 12, 13, 27, 28, 30, 31, 32, 33, 35, 36, 37, 39, 40, 42, 44, 45, 46, 47, 97

CTE COEFFICIENT OF THERMAL EXPANSION 39

DIC DIGITAL IMAGE CORRELATION 15, 27, 95

DT DECISION TREE 25

EPSC EXTENDED POINT STRESS CRITERION 27, 95

FBG FIBER BRAGG GRATING SENSOR .. ix, 5, 16, 17, 26, 27, 31, 32, 39, 42, 47, 48, 49, 51, 95, 96, 97

FDM FUSED DEPOSITION MODELLING 12, 13, 30

FEM FINITE ELEMENT METHOD ..... ix, 27, 29, 35, 36, 38, 45

FRP FIBER-REINFORCED POLYMER ..... ix, 5, 6, 7

IRT INFRARED THERMOGRAPHY 27, 29, 95

MAE MEAN ABSOLUTE ERROR 77

ML MACHINE LEARNING 4, 27, 95, 96

NDT NON DESTRUCTIVE TECHNIQUE 4, 27, 95, 96

PSC POINT STRESS CRITERION 27, 59, 95

RF RANDOM FOREST 25

RMSE ROOT MEAN SQUARE ERROR 81

SCF STRESS CONCENTRATION FACTOR 22

SHM STRUCTURAL HEALTH MONITORING 3, 5, 15, 16, 17, 27, 95

SLA STEREOLITHOGRAPHY 12

NOMENCLATURE

λ_{B0}	Reference Bragg wavelength
λ_B	Bragg wavelength
$\Delta\lambda_B$	Wavelength difference before and after loading
ε^T	Thermal strain
α_c	Thermal expansion coefficient of the host composite material
α_f	Thermal expansion coefficient of an optical fiber
ξ	Thermo-optic coefficient
Λ	Grating period
n_{eff}	Effective refractive index
X_t	Tensile strength
κ	Thermal conductivity
C	Heat capacity
E_{11}	Longitudinal elastic modulus
E_{22}	Transverse elastic modulus

G_{12}	In-plane shear elastic modulus
G_{23}	Out-of-plane shear elastic modulus
ν_{12}	Poisson ratio
K_t	Stress concentration factor
d_0	Characteristic distance
r	Radius of hole
x_i	Values of the x-variable in a sample
$\bar{x}$	Average of the values of x-variable
$\bar{y}$	Average of the values of y-variable
r	Correlation coefficient
β	Model feature
$I(\beta)$	Regularization
R^2	Coefficient of determination
x_{ij}	Actual training data for i'th observation
y_i	Actual target value
y_1^*	First predicted Value

y_2^*	Second predicted Value
C_1	First split subtree
C_2	Second split subtree
I_{mi}	Input layer
O_{ni}	Output layer
w_{ij}	Weight magnitudes
(B_i)	Bias
g	Activation function
n	Total number of records
i	Number of observations
μ_a	Mean value

1. INTRODUCTION

Due to their superior strength, stiffness, light weight, high corrosion resistance, design flexibility, and low thermal conductivity, fiber reinforced composite laminated structures have gained popularity over traditional materials like metals and pure polymers. These materials include reinforcement in a form of long or short fibers, polymer, filler (nano-tubes), etc., all of which have different chemical or physical properties. Although composites offer a high strength-to-weight ratio, they have not yet shown to be a miraculous answer for industrial structures.

The inspection of these materials' flaws is a challenge. High costs associated with labor intensity and complexity, expensive fabrication equipment may serve as a deterrent to the use of composite materials. However, they have recently become widely used in a number of industries, including construction, orthopedic applications, automotive, aerospace engineering, and etc. For instance, more commercial aircraft now have composite materials as part of their structure, especially in the last ten years, e.g. Boeing 787 contains more than 50% of its volume of composite structures (Groves, 2018).

Understanding the complex behavior and degradation processes of these materials have been of interest of many researchers during the last decade. Therefore, it is required to further investigate the structural performance of composite structures subjected to different loading conditions. On the other hand, due to the verge of Industry 4.0 it is now possible to reduce the cost and time associated with the experimental and numerical works for composite structures. Prediction models could be very useful for understanding the structural performance of the advanced materials.

2. State of The Art

In this chapter, the motivation behind using the AM composite structures embedded FBG sensors was discussed. Comprehensive literature review was conducted.

2.1 Motivation

Superior strength, stiffness, light weight, high corrosion resistance, design flexibility, and low thermal conductivity of fiber reinforced polymer composites (FRP) results in their increasing over traditional materials like metals and glasses. Composite materials consist of components (reinforcement, resin, filler, etc.) with different chemical or physical properties. The inspection of the flaws in these structures is a difficult undertaking to begin with. Second, high costs associated with labor intensity and sophisticated, pricey fabrication equipment may serve as a deterrent to the use of composite materials. However, they have recently become widely used in a number of industries, including construction, orthopedic applications, automotive, aerospace engineering, and more. For instance, more commercial aircraft now have composite materials as part of their structure. Composite materials now make up half of the Boeing 787's material composition (Mazumdar, Karthikeyan, Pichler, Benevento & Frassine, 2017). Additionally, according to Airbus, the demand for carbon fiber increased to almost 20,000 tons in 2020 (Deane, Avdelidis, Ibarra-Castanedo, Zhang, Nezhad, Williamson, Mackley, Davis, Maldague & Tsourdos, 2019). The desire to use composite materials in Boeing and Airbus aircraft is shown in Figure. 2.1, which depicts the trend shift that began in 2010.

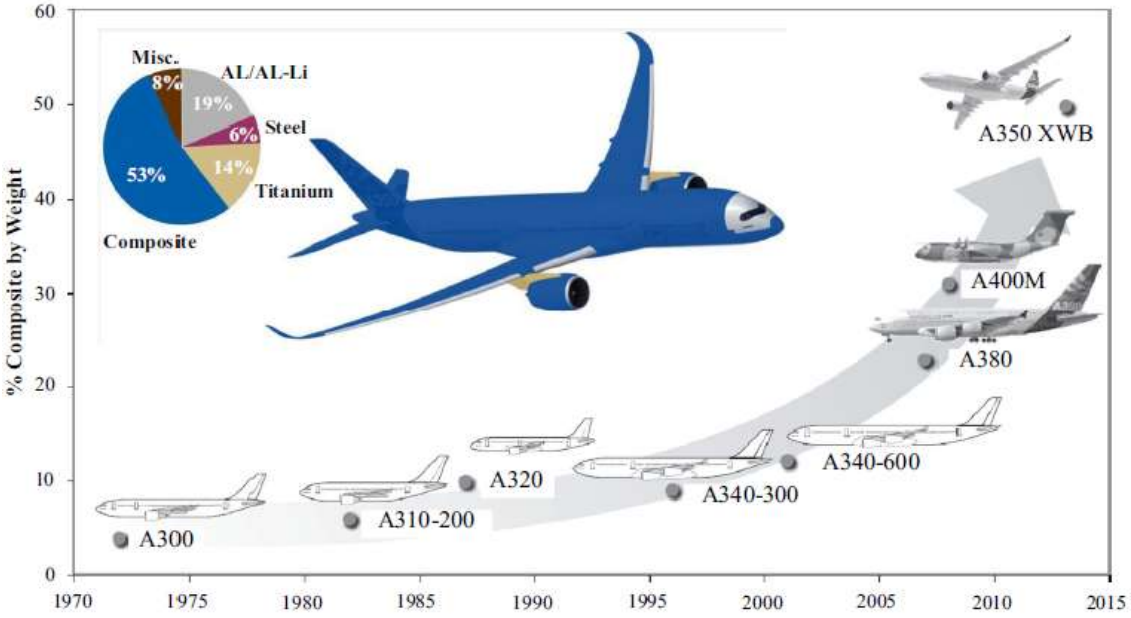

Figure 2.1 Trends in the use of composite materials in commercial aircrafts Airbus and Boeing (Xu et al., 2018)

Researchers were inspired to explore a developing method that can overcome the constraints that arose in the traditional fabrication processes, such as the fiber breakage and bandwidth restriction. Due to the flexibility, accuracy, cleanness, and capability of automated manufacturing techniques it is now possible to design novel advanced composite materials through green methods of fabrication, e.g. AM. AM is the construction of a 3-D objects which start from a CAD model. It could be conducted in a various procedures in which material is deposited, joined or solidified through the control of computer code. AM technique, that creates objects layer by layer from digital models. Traditional manufacturing methods often involve subtracting material through machining or molding, while AM builds up the material, urges the researchers around the world to overcome the challenges encountered in traditional composite manufacturing techniques. Their main advantage is related to minimum amount of waste and possibility of manufacturing elements with complex shapes.

Ensuring the safety, reliability, and longevity of infrastructure, and its continued development is of an utmost important while designing the additively manufactured composite structures. SHM uses conventional methods combined with sensors to examine a structure health; Hence it is useful to localize and quantify a variety of damages prevalent in composites-based structural models. SHM includes the observation of a system over time via sampled response measurements from time to time while monitoring the alterations to the geometric and material properties of engineering structures, e.g. buildings and bridges.

On the other hand, the problems associated with the composite structures with stress concentration region, e.g. holes make the analysis of these structures complicated. As previously mentioned, the holes are un-avoidable parts of several composite structures as they are required in different industrial application, specifically in aurospace engineering. Therefore, different tools could be developed to investigate the structural performance of these structures under various loading conditions. Measurement tools could be integrated with the numerical simulations to verify the results or utilize them as a further contribution to tests. NDT is used to evaluate the properties, integrity, and performance of materials, components, or structures without causing damage to them. These techniques are crucial in various industries to ensure the safety, reliability, and quality of materials and structures. Therefore, researchers are motivated to understand the behavior of those structures in detail.

On the other hand, understanding the degradation processes in composite laminates due to temperature or mechanical loading are of an utmost importance for industrial applications. Degradation processes refers to the changes in the material properties and structural integrity over time in composite laminates due to temperature or mechanical loading. Various damage types have been identified in composite structures including but not limited to matrix cracking, fibres breaking, thermal expansion mismatch, and debonding between matrix and fibre reinforcement. Understanding these degradation processes is essential for predicting the lifespan and performance of composite laminates, and it guides the development of materials and structures that can better withstand these environmental and mechanical challenges.

Finally, improvement of cutting-edge technologies brought about a novel prediction techniques. AI, neural network, and ML tools help in the post processing of data and decision making process. Researchers focused on ML approaches as a tool to predict the target variables provided that the input parameters are given to the ML algorithms. Needless to say that there is still more to do in order to make these techniques prevalent in industrial applications. However, recently composite materials have also been involved in this technology such that the prediction of the structural behavior of composite structures is of interest of many researchers.

2.2 Literature Review

In this section, the most important works related to composite materials, AM of these structures, SHM and its application in those structures were discussed later. The working principle of FBG sensor was explained in detail. For the parts related to chapter 2, the manufacturing techniques utilized for plain-weave composites with two interacting notches was discussed. Thereafter, the potential application of ML in composite structures was provided. Aims and objectives were summarized and based on that the outline of the thesis was structured.

2.2.1 Composite Materials

Manufacturing processes were not the only areas of technology progress. Making materials more effective—through, for example, the development of smart materials—has been one of the major objectives of research and industry associated with the fabrication techniques. Among various materials, which have been utilized in different industrial sectors (Shafighfard, Demir & Yildiz, 2019), composite materials have recently become widespread all around the world due to their outstanding properties which excel other conventional materials. The history of composite materials was turned back to the combination of straw and mud form bricks for building construction which was documented by Egyptians (Shaffer, 1993).

Composite materials have high strength-to-weight ratio, durability, thermal stability, corrosion resistance, and usage flexibility (Shafighfard & Mieloszyk, 2022). Composite materials typically consist of two or more materials in which each material possess its own property while merging these together generates new material with totally different s. This new material generally provides better structural performance than previous intact materials and could be utilized in applications which require better integrity. Different types of composite materials are utilized for various applications. Concrete is a well-known artificial composite material and generally has aggregates held with a matrix of cement. Another extensively used composite is FRP, which was also focused on in the present thesis, include CFRP which could either consists of thermoplastic or thermoset materials. Shape memory polymer composites (Zhang, Liu, Lan, Liu, Leng & Liu, 2022) is another type of composites in which fabric or fiber is used as reinforcement and shape memory

polymer resin as the matrix. Metal fibres reinforcing other metals, as in metal matrix composites or ceramic matrix composites (Azami, Siahsarani, Hadian, Kazemi, Rahmatabadi, Kashani-Bozorg & Abrinia, 2023) could also be utilized in composite materials. Natural fiber composites, which have recently been an interest of several research studies are another type of composite materials. Bamboo wood (Alencar, Rambo, Botelho, Barros, Sergio, Borges & Bertuol, 2023) fiber reinforced composite is one of well-known natural composite materials. A sandwich-structured composite (Rajpal, Lijesh & Gangadharan, 2018) is a another class of composites which is manufactured by attaching two thin and stiff skins to a lightweight and thick core. Particulate, advanced diamond-like carbon, and ferromagnetic composites (Koh & Sutradhar, 2022) are other type of composites which are not utilized in comparison to other composite materials. On the other hand, two different types of reinforcement including continuous and chopped carbon fibers are generally used inside matrix. Continuous fibers possess high aspect ratios with a specific orientation, while short fibers have low aspect ratios with a random orientation.

The application of these materials could be observed in bridges, buildings, boat hulls, racing car bodies, swimming pool panels, storage tanks, and so on. They are also being increasingly used in typical automotive applications. Advanced examples employed routinely on aircraft and spacecraft in demanding environments. Many industries have adopted composite materials, and by the end of the previous year (2022), the global market for composites had worth of $113.2 billion (Mazumdar et al., 2017).

Many researchers agree that traditional materials like wood, steel, and concrete as composite materials could not successfully resist corrosion. Thus, an alternative version called FRP composites, in particular, are employed in the construction, military, automotive, marine, and aerospace industries (Ahmed, Wang, Tran & Ismadi, 2021). On the otehr hand, FRP composites have a number of issues that require to be resolved in terms of structural analysis, material attributes, and design theory, comprising complex material composition, a high degree of discreteness in material properties, a lack of understanding of long-term performance in complex environments, and so forth (Zhou, Qian, Wang, Xiong & Wu, 2022).

Because of their intricate microstructure, it is more challenging to evaluate their structural performance than it is for a typical homogeneous material. Composite materials are generally composed of fiber (as a reinforcement) and matrix. The mechanical responses of the fiber bundle at the mesoscale are dictated by the microscopic fiber and the matrix (Figure. 2.2) that surrounds it, while the macroscopic mechanical responses of the composite materials—typical multiphase structural ma-

terials—are determined by the mesoscopic structure and matrix (Dong & Li, 2022). The fibers shown in Figure. 2.2, increases structural performance of overall material by adding reinforcement to the matrix.

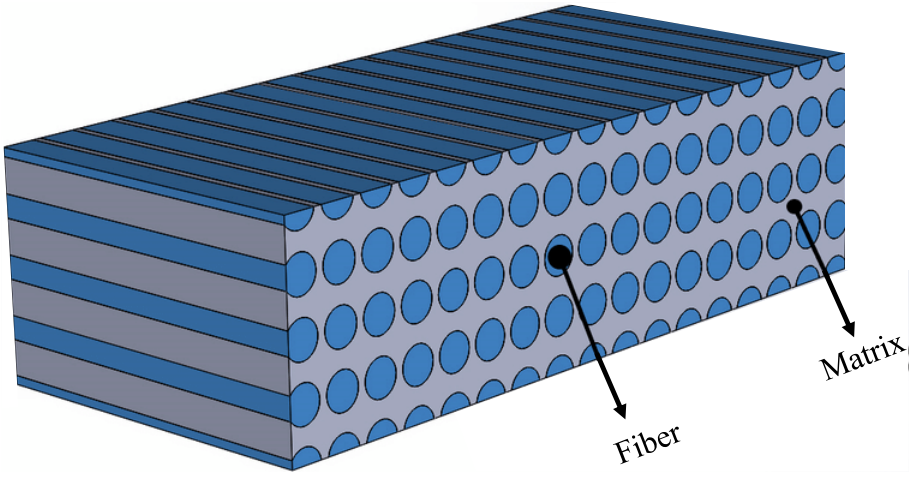

Figure 2.2 Schematic view of FRP including matrix and fiber reinforcement

As mentioned previously, damage mechanisms in composite structures are not as well understood like metals. Different types of damage happen in composite structures while manufacturing the sample or during the real life application of the component. The fabrication process has a vast potential to initiate defects in composite structures. These defects appeared in various methods of manufacturing. Porosity is one of the well-known defects reflected in a presence of a void within a matrix which is generally caused by incorrect curing parameters. Also, putting foreign bodies, e.g. backing film and/or finger marks in the matrix is another defect arised during the fabrication of composite specimens (Hakim et al., 2017). Common porosities appeared in composite structures are shown in Figure. 2.3.

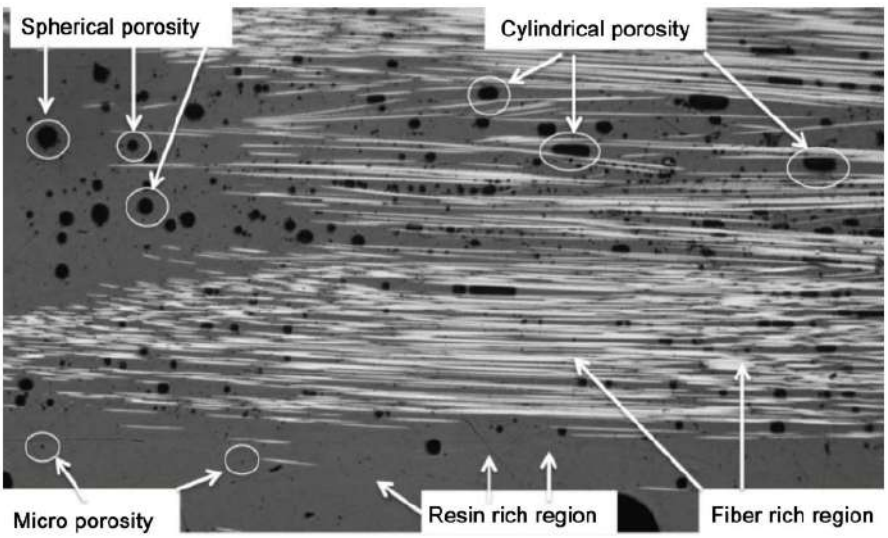

Figure 2.3 Different features and types of Porosity (Hakim et al., 2017)

Impact damage, is among the most happening defects appeared in composites due to the real life use. Delamination is among the highest possible defect because of the impact. In a laminated composite, delamination is failure which results in separation of the layers of plies and/or reinforcement material. Fiber-matrix debonding, fiber breakage, and matrix crack are other types of detects that could be captured in service life of the composite structures (Ma, Fu, Wang, Xu, He, Sun, Duan, Zhang, Jia & Zhou, 2022). All these defects are represented in Figure. 2.4. Fatigue, lightning strikes, compression, and bending also cause catastrophic fracture to composite structures and reduce their structural performance (Lu, Yuan, Yao, Li, Zhu & Zhang, 2023).

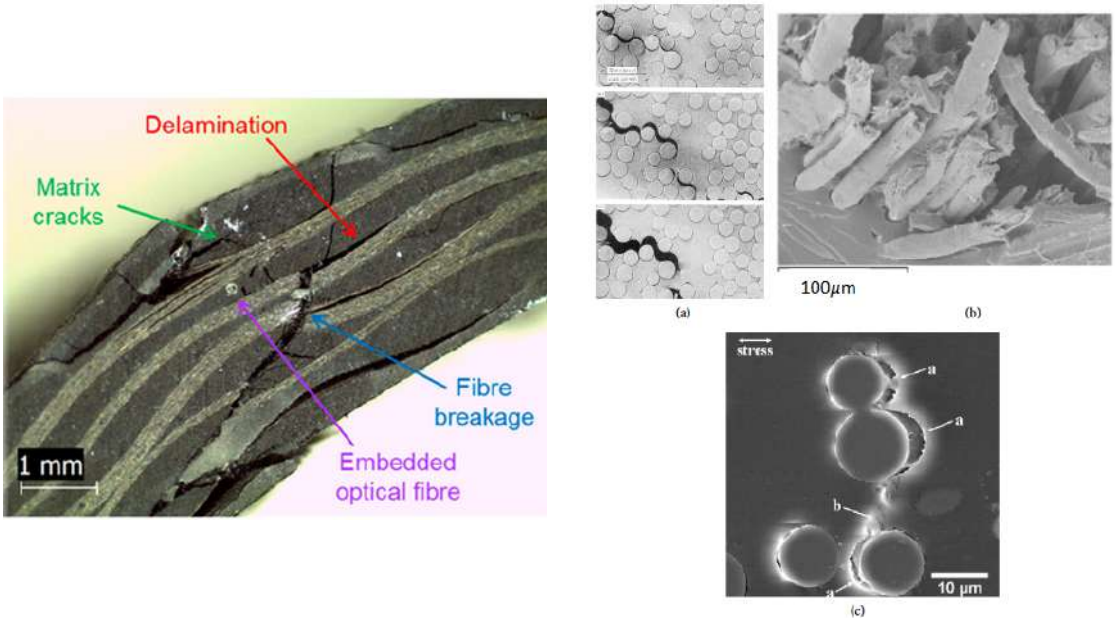

Figure 2.4 Different features of delamination (Chandarana et al., 2017) and a) Matrix crack; (b) Fiber breakage; and (c) Fiber-matrix debonding, "a" represents the matrix-fiber debonding and "b" shows matrix microcracks (Ghobadi, 2017)

As mentioned earlier, matrix, fiber, and interface damages are three categories into which defects can be systematically sorted. Thus, voids and incomplete curing in the matrix are examples of matrix defects. Misalignments, waviness, broken fibers, and inconsistencies in the distribution of fibers in the matrix are examples of fiber defects. defects as unbonded areas between layers and on fiber surfaces (delamination). On the other hand, each composite manufacturing methods causes defects on composite structures.

2.2.2 Additive Manufacturing

AM, so-called 3D printing, as a standard version (ASTM-F2792) of rapid prototyping (RP), is a layer-by-layer fabrication process in which successive layers of the material are deposited above each other taking advantage of a computer aided design to form the final product (Mieloszyk, Andrearczyk, Majewska, Jurek & Ostachowicz, 2020). AM efficiently creates 3D products from materials, already designed in 3D CAD softwares, by adding layers on top of each other, minimizing the complexity of the product development cycle, supply chains, tool modification, and labor costs (Hosseini, Cederberg, Hurtig & Karlsson, 2021). In contrast, the term subtractive manufacturing was used for the large family of machining processes with material removal as their common process. Thanks to the recent development in technology, AM has been widely utilized in various industrial applications such as aeronautical, automotive, dental, architectural, and medical for fabrication of special parts, particularly with complex geometries (Shafighfard, Cender & Demir, 2020).

In early 2000, the term 3D printing referred just to the polymer technologies (Pokkalla, Hassen, Nuttall, Tsiamis, Rencheck, Kumar, Nandwana, Joslin, Blanchard, Tamhankar & others, 2023), and the term AM was more likely to be used in metalworking and end-use sample production contexts than among polymer, and stereolithography enthusiasts. By the early 2010s, the terms "additive manufacturing"or "3D printing" evolved senses in which they were alternate terms for additive technologies which are utilized interchangeably (Hassen, Betters, Tsiamis, West, Smith, Billah, Nuttall, Kumar, Smith & Kunc, 2022). Pioneer AM tool and materials were developed in the 1980s (Kodama, 1981) and they have been developed during four decades of technological improvement.

Different materials such as metals, ceramic, and polymers have been utilized for AM fabrication of specimens as depicted in Figure. 2.5.

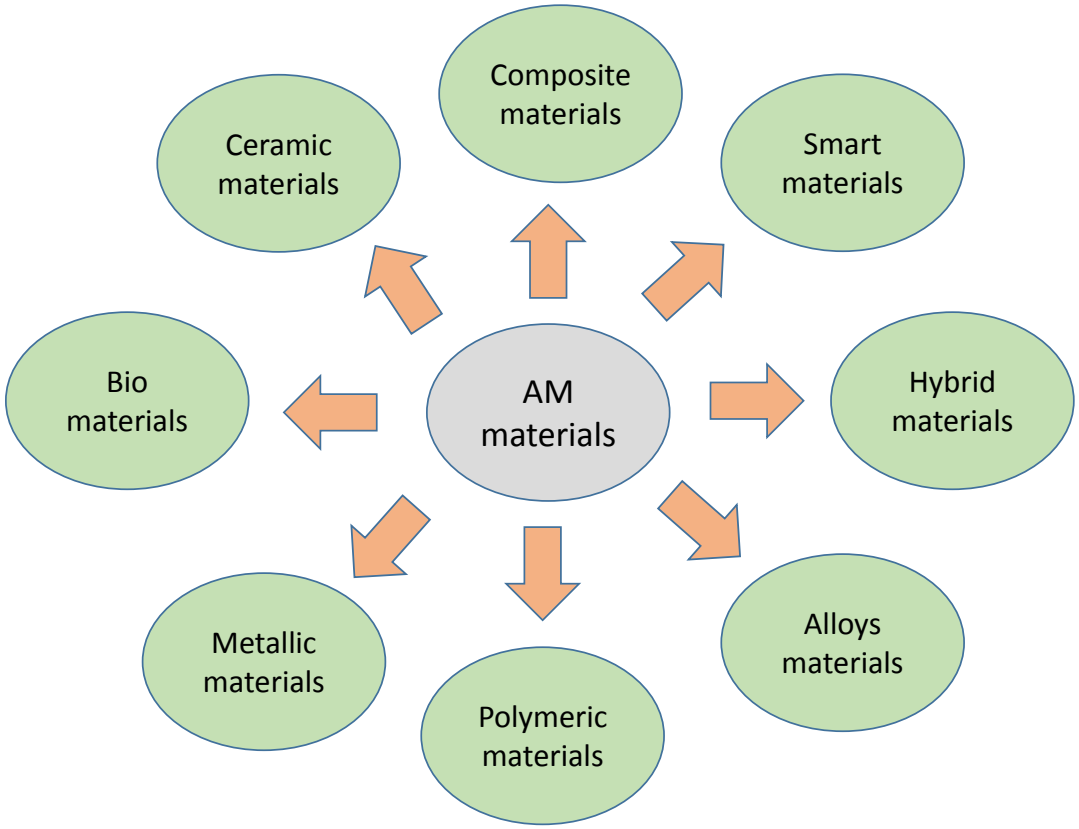

Figure 2.5 Different materials utilized in AM process

3D printing based on the vat photopolymerization, powder bed fusion, material extrusion, material jetting, binder jetting, sheet lamination, and directed energy deposition are the main AM techniques utilized for manufacturing samples with different materials. Classification of 3D printing techniques based on the raw material is illustrated in Figure. 2.6. The techniques classification presented here originated from the paper written by (Dizon, Espera Jr, Chen & Advincula, 2018). The laser melting method includes bulk material. The printing types are direct metal deposition (DMD), Laser Engineered Net Shaping (LENS), layer plastic deposition (LDP). Powder material type includes selective laster sintering (SLS), selective laser melting (SLM), direct metal laser sintering (DMLS). For the liquid part integrated with the laser polymerization, stereolithography (SLA), solid ground curing (SGC), and liquid thermal polymerization (LTP) are mostly utilized. The well-known techniques for material jetting are 3DP Binder Jetting (3DP), inkjet printing (IJP), multi jet modeling (MJM), ballistic particle manufacturing (BPM), and jet printing (JET). Thermal extrusion based methods are fused deposition modeling (FDM), and fused filament fabrication (FFF). Electron beam (EBM), laminated object manufacturing (LOM), and solid foil polymerization (SFP) are the other methods of 3D printing.

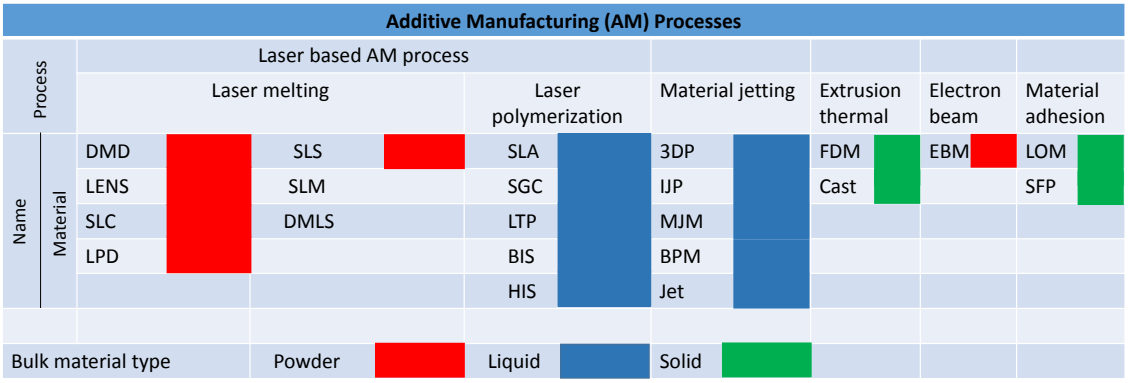

Figure 2.6 Schematic view of AM division on the basis of type of materials

AM provides superior design flexibility comparing to conventional manufacturing methods; Hence providing an opportunity to improve structural performance of fabricated structures (Shafighfard et al., 2020) while being much more environmentally friendly. From the beginning (an early 1970s), many researchers have been interested in using AM technique to fabricate specimens with simple and/or complex geometries and/or functions as well as with various materials, such as polymers (Park & Fu, 2021), metals (Gardner, 2022), ceramics (Hofer, Kocjan & Bermejo, 2022), composite materials (N'dri, Charpentier, Hirsinger, Gilbin & Barriere, 2023), and others, which can be in any form including but not limited to powder and filament. Recently, sustainability of AM has been among the most well-known discussions within the research society. This technique has the ability to decouple the creation of social and economic value from the environmental effect of corporate operations and is intrinsically less wasteful than conventional subtractive techniques of production. Three main benefits of this method in the view of sustainability were offered as: improved resource efficiency, extended product life, and reconfigured value chains (Ford & Despeisse, 2016).

The disadvantages associated with the AM technique has hindered them from applying in several industries. There should be much more research in AM on composite structures will lead to the applicability of these structures fabricated by 3D printing in more industrial works. The surface finish of an additively manufactured samples have been investigated over the last years. However, there are two major challenges to be tackled. One is the overall finish capability of the additive manufacturing printing material itself. It is rough with respect to traditional powder metal materials. The other is the layering effect in AM part construction. Also, due to the contraction, sample experiences further friction during 3D printing. The mechanical attributes of a final sample depend on the printing parameters. Therefore, trial and error might be required to fabricate the composite structures with AM. The possi-

bility of voids and layer gaps is more in additively manufactured specimen than conventional fabricated one. Materials characterization of 3D printed samples is further challenged by AM machine. Process variability needs high level of customization of the methods for in situ measurement (Tofail, Koumoulos, Bandyopadhyay, Bose, O'Donoghue & Charitidis, 2018).

Almost thirty distinct technologies are now accessible for AM, having begun the revolution's journey with SLA in the 1980s. However, the fundamental steps which include designing, cutting, constructing, and finishing, remain the same (Kumar, Pandey & Wimpenny, 2019). In light of this, AM is a versatile and quick technology for manufacturers to build new items because it eliminates the need for additional manufacturing processes like molding and fittings.

2.2.3 Fused Deposition Modeling

The conventional techniques for fabricating CFRP composites are expensive, involve a complicated preparation procedure, and are challenging to design structurally. Thus, following the pillars of Industry 4.0, AM could be adopted to fabricate composite materials (Mieloszyk, Shafighfard, Majewska & Andrearczyk, 2023). The advantages associated with both AM, in comparison to conventional methods of manufacturing, and CFRP, comparing with the conventional isotropic materials pave the way for integrating these to design and manufacture low cost high strength structures. Because of their benefits in process control and low cost, extrusion-based techniques among a wide range of 3D printing processes show tremendous potential in producing CFRP composites. One of the widely used, easily accessible, low surface porosity, and affordable extrusion-based processes is FDM.

This process involves extruding a continuous strand of material into the print bed using a bowden tube. The original substance is a flexible filament that is gently melted in the hot end before being extruded onto the building plate through a warm nozzle. The molten material is immediately cooled, solidified, and attached to the nearby rasters while the phase change occurs. The liquifier head is raised in the following phase, and until the desired final sample is obtained, another layer is extruded on top of the preceding layer (Shafighfard & Mieloszyk, 2022).

In the standard FDM technique generally two nozzles are employed: one for polymer and the second for fiber. This method typically led to a porosity, cracks, and etc. in the fabricated samples due to the thermal stress and residual stress appeared while

fabricating specimens (Mieloszyk, Majewska & Andrearczyk, 2022).

Over the past ten years, there has been a significant amount of research on FDM technology for producing composite materials (Krajangsawasdi, Blok, Hamerton, Longana, Woods & Ivanov, 2021). Damage analysis under different loading conditions (Caminero, Chacón, García-Moreno & Rodríguez, 2018; Hu, Ladani, Brandt, Li & Mouritz, 2021; Luan, Yao, Zhang, Wang & Fu, 2019), thermal analysis (Compton, Post, Duty, Love & Kunc, 2017; Heidari-Rarani, Rafiee-Afarani & Zahedi, 2019; Tambrallimath, Keshavamurthy, Saravanabavan, Koppad & Kumar, 2019), electrical analysis (Santo, Penumakala & Adusumalli, 2021; Sezer & Eren, 2019; Yang, Li, Zhou, Liu, Li, Yang, Yuan & Zhang, 2019), failure behavior (Hao, Liu, Wang, Guo, Chen & Fang, 2019; Saleh, Anwar, Al-Ahmari & Alfaify, 2022), microstructural analysis (Li, Zhao, Li, Yang & Wang, 2019; Peng, Bin, Shouling, Lei & Huang, 2021), defect detection (Lu, Hou, Yuan, Yao, Li & Zhu, 2023; Zou, D'Antino & Sneed, 2021), etc. are among the research studies carried out for mechanical and thermal characterization of different composite materials fabricated through FDM process.

Two different kind of fiber reinforcements called chopped and continuous are generally utilized to 3D print the CFRP materials. Even though the most well-known and prevalent type of the fibers is chopped (short) one (Christ, Schnabel, Vorndran, Groll & Gbureck, 2015), the continuous fibers provide higher structural integrity (Hou, Tian, Zhang & Li, 2018) since they have high stiffness to weight ratios, high fatigue life, and stability under force. FDM offers a new technique for the integrated manufacture of complicated CFRPs by producing a regulated distribution of a continuous fiber through a path design. The schematic view of FDM tool/process is illustrated in Figure. 2.7.

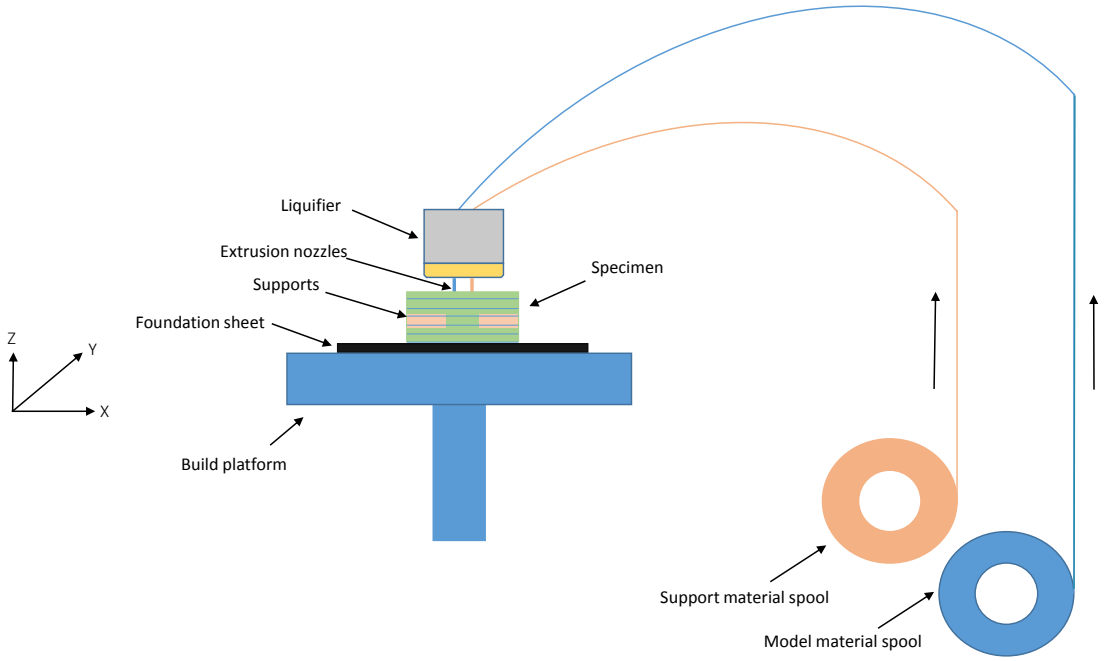

Figure 2.7 Standard configuration of FDM process/tool

2.2.4 Structural Health Monitoring

Despite the substantial benefits of using composites, CFRP composites can develop complicated flaws throughout the manufacturing and assembly processes or experience wear and tear while in use (Kamath, Sundaram, Gupta & Subba Rao, 2010). Aging, poor service conditions, incorrect manufacture, and incorrect assembly can all lead to defects in composite materials over time, including porosity, inter-laminar voids, fiber waviness, wrinkles, de-bonding, and delamination. Similar to other manufacturing methods, there have been different defects associated with the FDM technique which provide adverse effect on the strength and quality of the printed part (Wickramasinghe, Do & Tran, 2020).

It was shown that the advancement of AM technology has been hampered by the lack of trustworthy in-situ monitoring for purposes of managing the building process and end product quality (Quan, Wu, Keefe, Qin, Yu, Suhr, Byun, Kim & Chou, 2015). The importance of damage detection during AM process has been highlighted in several positions (Safaee, Schock, Joyee, Pan & Chen, 2022; Yuan, Li, Zhu & Tang, 2021), though according to (Kousiatza, Tzetzis & Karalekas, 2019), there is still significant ongoing research on in-situ process monitoring for AM technologies, and its capability is still limited. In general, non destructive testing procedures are applied

to an object to identify and characterize surface and internal defects without damaging the inspected sample. Acoustic emission, infrared thermography, ultrasonic, shearography test, terahertz imaging, DIC, eddy current, and X-ray are among the well-known techniques developed for damage detection and failure analysis (Ahmed et al., 2021). However, limitations have been observed for this techniques. First, only surface-level defects can be found by it. Second, preparation is required before a test which could be expensive and time-consuming.

SHM approaches could be a solution for some of the aforementioned problems. SHM uses conventional methods combined with sensors to examine a structure's health; Hence it is useful to localize and quantify a variety of damage prevalent in composites-based structural models. SHM includes the observation of a system over time via sampled response measurements from time to time to while monitoring the alterations to the geometric and material properties of engineering structures, e.g. buildings and bridges. In the SHM method the following diagnostic levels can be distinguished:

1.1 detection – detection of existing damage : SHM involves the continuous or periodic monitoring of a structure's condition using various sensing technologies. The primary goal is to find any anomalies, defects, or damage that may compromise the structural integrity

1.2 localisation – determination of the damage location: Determining the location of damage in a structure using SHM involves the analysis of sensor data to pinpoint the area where damage or anomalies are occurring

1.3 identification – damage type classification (size or type) : This technique often involves assessing the size and nature of the damage.

1.4 prediction – determination of time of the structure safe work: Predicting the remaining safe working time of a structure in SHM involves assessing the current condition of the structure, analyzing the rate of deterioration or damage progression, and making predictions about when the structure may no longer meet safety standards

1.5 self-healing (optional) – reaction to damage by removing its effects: Self-healing materials in the context of SHM refer to materials that have the ability to react to damage by mitigating its effects, thereby restoring or maintaining their structural integrity.

The long-term goal of SHM could be explained as the outcome which is, from time to time, updated data regarding the ability of the structure to conduct its function

to explore the inevitable aging and degradation resulting from operational environments. After catastrophic happenings, e.g. blast loading, SHM could be employed for quick condition screening while aiming to provide reliable information regarding the integrity of the structure in a short period of time.

SHM is extensively employed for composite materials but for AM composites it is still under development. Regardless of the application, the common purposes of SHM systems could be summarized as following: recognize the severity of deterioration, identify the stage of structural devastation, and assess the need for further inspection or advance maintenance of the condition based on dangers that possibly results in catastrophic failure.

2.2.5 FBG working principles

Optical fiber sensors have been one of the well-known SHM tools which is mostly utilized for the capture of strain (Mieloszyk, Majewska & Ostachowicz, 2020) and temperature (Liang, Liu, Wang, Zhang, Wu, Qing & Wang, 2022) of any structure. Fiber-optic sensors are immune to electromagnetic intervention while not conducting electricity; Hence they could be utilized in flammable material or high voltage electricity applications (Mieloszyk et al., 2023). Fiber-optic sensors can be designed to withstand high temperatures as well. These sensors can be divided into various categories. Intrinsic, extrinsic, chemical, and biosensors are among the well-known optical sensors. Intrinsic fiber-optic sensors could provide distributed sensing throughout very long distances. On the other hand, extrinsic fiber-optic sensors provide very high protection of measurement signals against noise corruption. Chemical sensors disturb the light propagation, thus an interaction of the light with the near area and constructing fiber-optic sensors are enabled.

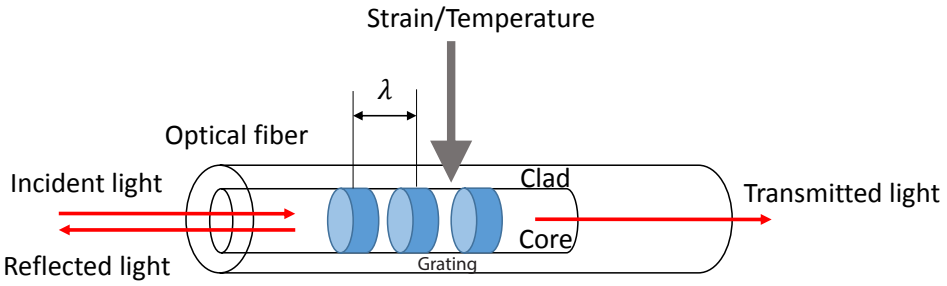

Figure 2.8 Schematic view of FBG sensor

FBG sensors are one of the most well-known sensors which have been employed in SHM as an effective monitoring tools. FBG sensors are lightweight, tiny in size, durable, tolerate high temperatures, and immune to electromagnetic fields. They also have great corrosion resistance without further need for calibration (Liao, Liang, Luo & Xiao, 2022). The measurement equipment and conventional electrical sensors are replaced by this optical technology and in particular, damage detection and localization are two applications for these sensors, which can be used to measure the strain on structures. The schematic view of an FBG sensor is represented in Figure. 2.8.

The pioneer fiber Bragg grating was shown in 1978 (Chan, Yu, Tam, Ni, Liu, Chung & Cheng, 2006). Firstly, the gratings were manufactured by a observable laser distributing along the fiber core. Later on, much more flexible transverse holographic inscription technique where the laser illumination came from the side of the fiber was demonstrated. In this method, the interference pattern of ultraviolet laser light was employed to generate the periodic structure of the FBG (Meltz, Morey & Glenn, 1989). Portion of the optical fiber that implements a periodic core refractive index modulation is found inside a uniform FBG sensor. Different types of FBG sensors are widely utilized for the measurement purposes including uniform, chirped, tilted, and superstructure. FBGs are fabricated through inscribing systematic (periodic) variation of refractive index in the core of a specific kind of an optical fiber employing an intense ultraviolet (UV) source, e.g. UV laser. Two techniques are typically utilized: interference (Meltz et al., 1989) and masking (Hill, Malo, Bilodeau, Johnson & Albert, 1993). The preferred technique depends upon the type of grating to be fabricated. However, germanium-doped silica glass fiber is most commonly utilized. Also, fibers could be utilized in case the photosensitivity is increased through soaking the fiber in hydrogen. FBG sensor (os-1100 micron optics) is illustrated in Figure. 2.9.

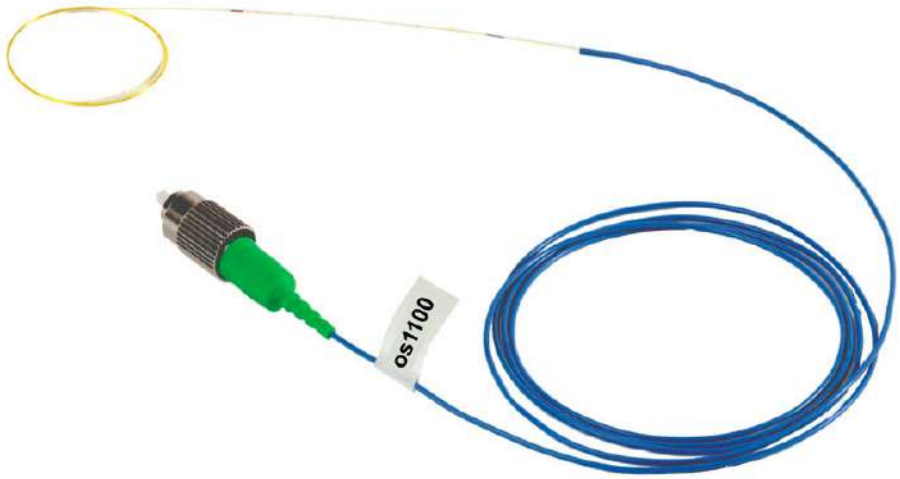

Figure 2.9 FBG sensor (os-1100)

The center wavelength shift of the Bragg gratings is the basis for how FBG sensors operate. When light passes through a Bragg grating, its primary function is to selectively reflect only a narrow spectral component of a broadband source. A huge reflection at a certain wavelength is created by the combination of all the reflected light signals, called the bragg wavelength, λ_{B0}. As specified by the Bragg condition, the spectral response of a uniform FBG in its free state is a signal peak centered at the Bragg wavelength (Measures & Abrate, 2002) as following:

$$\lambda_B = 2n_{eff}\Lambda. \tag{2.1}$$

Λ is the grating period and n_{eff} is the effective refractive index for the guided mode of interest. All light signals at wavelengths other than the Bragg wavelength are transmitted unmodified; only those wavelengths that satisfy the Bragg condition are impacted and back-reflected. Strain and/or temperature changes have an influence on both the n_{eff} and Λ parameters, which makes the Bragg wavelength sensitive to those changes. Therefore, its reflected spectrum represents a shift in the Bragg peak without changing the wavelength shape when uniform alterations in the aforementioned magnitudes occur along the FBG (Udd & Spillman Jr, 2011). Generally disturbances in spectra shape of the FBG sensors could be observed. The problems can be related to inconsistent strain distribution along FBG sensor gauge length and its deformation (Mieloszyk, Majewska & Ostachowicz, 2021).

The following equation can be used to calculate the difference between the Bragg wavelength in chosen moment in time, λ_B, and the reference one, λ_{B0}. These were

obtained from the peak shift of the spectra, before and after the mechanical and thermal loading, when a uniform FBG is subjected to a homogeneous axial strain, ε_x, and temperature changes, ΔT:

$$(\lambda_B - \lambda_{B0})/\lambda_{B0} = \Delta\lambda_B/\lambda_{B0} = (1-p_\varepsilon)\varepsilon_{res} + (1-p_\varepsilon)\varepsilon^T + (\alpha_f + \xi)\Delta T. \tag{2.2}$$

The equation is valid by assuming ε_z=$\varepsilon_y = -\nu_f\varepsilon_x$, transverse strains applied to the optical fiber is related to the axial strain by ν_f (Poisson ratio of optical fiber). It should be noted that the short length (3 mm) of the inserted Bragg grating and the absence of a peak split in the recorded wavelength support the aforementioned assumption of a uniform axial strain applied to the FBG. α_f=8×10^{-7} is an expansion coefficient of optical fiber (Lai, Friedrich, Botsis & Burkhart, 2010), ξ=8×10^{-7} is the thermo-optic constant for the fiber (Shibata, Shibata & Edahiro, 1981), p_ε=0.215 is the strain-optic constant for the fiber (Giaccari, Dunkel, Humbert, Botsis, Limberger & Salathé, 2004), ε_{res} is the solidification induced residual strains, $\Delta\lambda_B$ stands for the wavelength difference before and after loading, and ε^T is the thermal strain propagated because of a mismatch in thermal expansion coefficient of the host composite material, α_c, and the optical fiber, α_f:

$$\varepsilon_T = (\alpha_c - \alpha_f)\Delta T. \tag{2.3}$$

Total strain ϵ_c for the FBG sensor was given by:

$$\varepsilon_c(T) = \frac{\lambda_p(T) - \lambda_b(T)}{\lambda_b(T)}. \tag{2.4}$$

in which λ_b and λ_p were base and measured Bragg wavelengths, respectively.

Strain values associated with the thermal effect on the host material was calculated through:

$$\varepsilon_m(T) = \varepsilon_c(T) - \varepsilon_f(T). \tag{2.5}$$

It is worth adding that the calculations presented in the thesis are performed on

sensors embedded into composite structure. Where index m is material related component, whereas index f is correlated with the effect of the temperature on the FBG sensor and optical fibre material.

During the FDM manufacturing process of Polylactic acid (PLA) material (Brischetto & Torre, 2020) and composite structures (Oromiehie, Prusty, Compston & Rajan, 2018), FBG sensors could be incorporated using conventional techniques. FBG sensors could also be embedded into 3D printed composite structures fabricated through the FDM method during the 3D printing process. Even though FDM of CFRP composites has demonstrated rising progress and has attracted the researchers' intensive attention over the past few years, there are still significant issues which are related to the mechanical performance of 3D printed composite structures that need to be investigated. The ultimate mechanical performance of composites produced by 3D printing is significantly influenced by the natural temperature fluctuations and thermal gradients of the FDM process. The bond formation quality at the fiber-matrix interface, between neighboring reinforced rasters, and the level of interlayer adhesion are all significantly affected by the frequent heating and quickly cooling cycles that take place during the fabrication process. Additionally, the internal residual strains and stresses in the fabricated composites, accumulate as a result of the thermal gradients created during the layerwise FDM deposition process. In addition to having an effect on the final mechanical performance of composites, residual strains and stresses can lead to dimensional error and part distortion (Zhang, Wu, Sun, Quan, Gu, Sun, Cotton, Heider & Chou, 2017).

2.2.6 Plain-Weave composites with two interacting notches

Due to their exceptional qualities, textile composites, which three main types of which are shown in Figure. 2.10, have become very popular structural materials that are used in the automotive and energy industries. These applications include different components that should be assembled into larger assemblies to provide the desired final design. Thus drilling holes are an unavoidable part of composite structures.

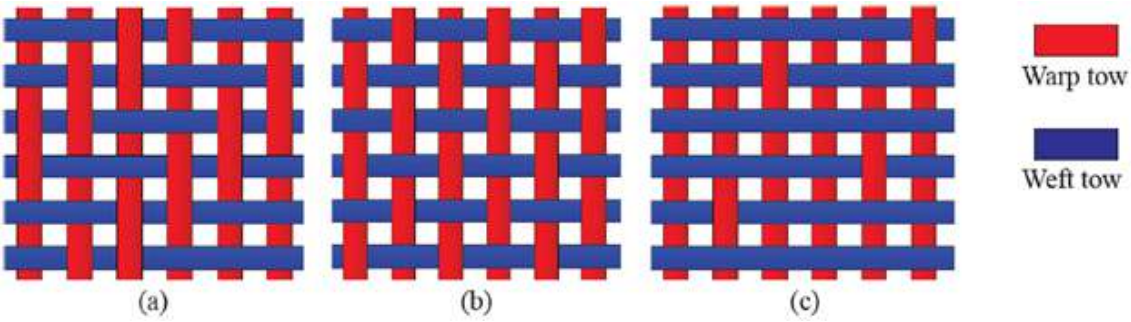

Figure 2.10 Three common woven composites (a) Twill weave, (b) Plain weave, (c) Satin weave

Plain weave composite has one by one weave with each warp strand floating over 1 fill strand then under 1 fill strand. The frequent over and under weaving decreases the overall strength of the fabric. This weave creates a fabric that will fray the least and works well for flat surfaces but is the least pliable and does not drape well over shaped molds. Weave structure, plain woven fabric is similar to a checkerboard pattern of straight interlacing threads going under and over each other in right angles, similar to a woven basket. Examples of plain weave fabric are organdy, chiffon, flannel, twill and satin, and seersucker.

Generally the most cheap textile for a variety of applications are woven materials. These fabrics could be treated with substances to offer them characteristics such as waterproofing and breathability. Also, they are easily available and convenient to source from an extensive-ranging supply chain.

Despite having advantageous physical characteristics, these composites are prone to failing under load, and their complex behavior sets them apart from isotropic materials. The performance of these materials would therefore need to be analyzed using further computations. This behavior becomes more complex for designs with holes, which causes the strength to decrease as a result of stress concentration around the notch (Liu, Zhang, Li, Chen, Huang & Guo, 2022). Understanding the behavior of these materials is therefore necessary in order to create designs with outstanding structural response. Significant amount of research have been conducted to investigate the structural performance of open-hole composite structures in different loading conditions (Galos, 2020). SHM of these structures have drawn the attention of researchers in the subject of composite structures.

However, there have been a limited number of studies about the mechanical performance of composite structures with two interacting notches which makes it hard to understand the performance of open-hole composites after adding an additional notch. This is specifically a case for plain-weave composites. The failure load of

composite laminates with two holes with different shapes was investigated in several works (Ataş, Arslan & Sen, 2009; Ghezzo, Giannini, Cesari & Caligiana, 2008; Karakuzu, Taylak, İçten & Aktaş, 2008; Xu, Man & Yue, 2000). Damage evolution of composite structures including two notches were also studied in a few literatures (Amaro, Reis, De Moura & Neto, 2013; Kouka, Abbassi, Demiral, Ahmad, Soula & Al Housni, 2021; Özaslan, Yetgin, Acar & Güler, 2021; Pal & Ray, 2002; Solis, Barbero & Sánchez-Sáez, 2020). A few researchers studied the effect of an additional hole on the SCF of composite structures. Different geometry of holes, stacking sequences, material, and etc. were compared in different works to capture the distribution of stress around the cut-outs of composite plates (Achache, Boutabout & Ouinas, 2013; Maksymovych & Illiushyn, 2017; Özaslan, Güler, Yetgin & Acar, 2019).

Finite element models were developed to numerically understand the structural behavior of composites with multiple notches. Experimental studies including different measurement equipment were also utilized for this purpose. However, there is still a requirement to understand the integrity of plain-weave composites including two circular holes in different configuration and for different stacking sequences of composite layers while subjected to tension.

2.2.7 Machine Learning application in composite structures

The entire field of composite structure design and analysis is expected to undergo significant changes over the next decade as a result of the extensive number of numerical simulations and experiments, improvements in computing power, and emerging sophisticated algorithms (Avci, Abdeljaber, Kiranyaz, Hussein, Gabbouj & Inman, 2021; Bagherzadeh & Shafighfard, 2022a; Haywood-Alexander, Dervilis, Worden, Cross, Mills & Rogers, 2021). On the other hand, due to the vast digital data and algorithms connected to AI and ML systems, there have been notable advancements in the last ten years in the fields of automated data analysis and ML (Bagherzadeh & Shafighfard, 2022b). Artificial intelligence (AI) is the imitation of human intelligence functions by machines, particularly computer systems. Learning, reasoning, and self-correction are some of these processes.

ML is generally categorized as supervised learning, unsupervised learning and reinforcement learning, based upon the type of data (output and input), and the kind of problems to be solved. In supervised learning, which was employed here, a dataset containing input and output, is utilized to build an algorithm. Finding the best

mapping function possible to match the input and output pair is the final goal. Depending on their purpose, algorithms could be divided to regression models (linear and nonlinear regression, Bayesian, decision trees, deep learning, etc.) or classifiers (Bayesian, neural networks, decision trees, deep learning, etc.). Figure. 2.11 represents the algorithms of ML which are categorized efficiently, while listing well-known methods in different sub-fields. Bayesian models include Bayesian network, Bayesian belief net (BBN), Generative bridging Network (GBN), and Naive Bayes (NB). Decision trees contain a classification and regression tree, decision stump, conditional decision trees, and Chi-squared automatic interaction detection algorithms, Instance based are K-nearest neighbor, support vector machine, and learning vector quantization models. Deep learning includes convolutional neural network (CNN), stacked, recurrent neural network (RNN), and generative adversarial network (GAN). Linear, ridge, logistic, and multivariate adaptive regression splines are inside the regression models. Perceptrons, back propagation, hopfield, and radial basis function network are included inside the neural networks. Clustering contains k-means, k-medians, hierarchical, and centroid algorithms. Finally, ensemble techniques are random forest, gradient boosting machine (GBM), adaboost, and other boosting models.

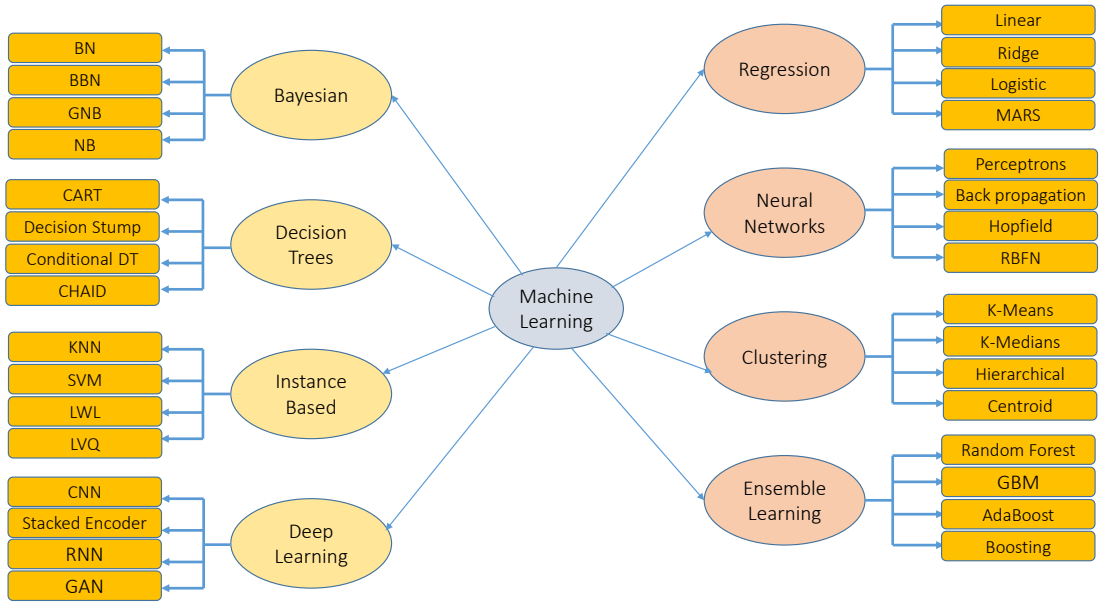

Figure 2.11 Machine Learning models mind map

The main interest in many research problems in both fiber reinforced polymer composites and ML is to propose predictive algorithms for one or more variables of interest using relevant independent parameters or inputs. However, these two contexts have often take different methods such that the modeling of the behavior of composites relies on physics-based models and phenomenological theories. Although these physical models are more accurate and robust, they are constrained to a specific set of conditions, which often limits their predictive power. ML algorithms, on the other hand, could be more efficient during the design phase because they can manage large, high-dimensional datasets to extract optimal or predictable behavior for the application at hand.

Thanks to the supervised ML, time-efficient processing techniques and computationally low-cost methods have been developed, especially for composite structures (Zimmerling, Dörr, Henning & Kärger, 2019), make contribution to the prediction of structural performance of these materials. Several studies have been carried out on the application of ML methods for mechanical characterization of composite structures with and without cut-outs (Lee, Lim, Skinner, Chattopadhyay & Hall, 2022). Overall, majority of the works concentrate on the application of ML approaches on the prediction of structural integrity of different composite structures under various loading and boundary conditions. ML techniques have been helpful in understanding the behavior of composite materials without further conducting lab tests and complex numerical studies. They are perceived as a prominent tool for the design and exploration of advanced materials for an extensive range of applications. This is important due to the fact that designing advanced materials with outstanding attributed is the final aim of modern engineering applications in this era.

Material characteristics and the geometrical arrangement, e.g. composite stacking order, length-to-width ratio, hole orientation, etc. affect the composite design's structural performance in a significant way. As a result, numerous studies have been performed to analyze the material characterization of these structures. ANN has been one of the well-known approaches, which has been utilized for the prediction of strcutural behavior of composite structures with hole in the past decade (Califano, Chandarana, Grassia, D'Amore & Soutis, 2020; Zhang, Ma, Song, Gao, Zhou, Liu & Tao, 2022). Progressive damage prediction using ANN for the composite structures with two holes was investigated in (Nguyen & Waas, 2020; Shirazi, Khatir, Benaissa, Mirjalili & Wahab, 2023; Zhang et al., 2022). Ultimate strength of reiforced composites was studied through ANN algorithms (Brahim, Belaidi, Khatir, Le Thanh, Mirjalili & Wahab, 2023; Hosseinpour, Daei, Zeynalian & Ataei, 2023; Liu, Lei, Zhu, Shang & Bai, 2022). For the purpose of predicting the mechanical performance of composite structures with and without notches that were subject to

mechanical loading, various ML techniques were employed. Convolutional neural networks (Yang, Kim, Ryu & Gu, 2020), DT and adaptive boosting (AdaBoost) regressor (Daghigh, Lacy Jr, Daghigh, Gu, Baghaei, Horstemeyer & Pittman Jr, 2020), k nearest neighbors (Balcıoğlu & Seçkin, 2021), RF, DT, and deep learning (Kaveh, Eslamlou, Javadi & Malek, 2021).,

2.3 Aims and objectives

The aim of the thesis is to explore the possibilities for applications of diagnostic techniques (SHM and NDT) for FRP elements manufactured using standard and additive manufacturing methods. The analysed structures have imperfections understood as voids, gaps between fibre bundles, delaminations, holes, etc. or inclusions in a form of embedded optical fibres with FBG sensors. Such imperfections can be related to the manufacturing method features (e.g. voids in AM structure) or inclusions introduced intentionally (e.g. optical fibres) or the geometric characteristics of the structure (e.g. holes). All of the elements results in local stress/strain concentration, changes in material mechanical and material properties that influenced on their degradation processes.

This Ph.D. thesis contains three main sections. The first part is devoted to show an importance of the application of AM on fabrication of composite material with embedded FBG sensors and the effect of FBG sensors on the durability of the material. In the second part, autoclave curing was conducted to manufacture plain-weave composites containing two interacting holes. The influence of the holes on the fracture mechanism is discussed in this section. In the final section, the application of ML in reducing the time and labour cost of experimental and numerical works is provided.

The primary goal of the first section is to use computational and experimental investigations to examine the structural performance and degradation process of 3D printed CFRP specimens that include embedded FBG sensors. Thermal and tensile strain of the UD composite specimens fabricated by FDM is investigated. The novelty of the AM method is the embedding process of FBG sensors that is performed during the AM process. Therefore, the theoretical and experimental investigations will be focused on the influence of the embedded FBG sensors on the mechanical properties of the elements in comparison to the samples without embedded sensors. The AM structures with embedded FBG sensors were manufactured in cooperation with Kaunas University of Technology (Lithuania). At the IMP PAN a measurement stand for experimental investigation of the thermal loadings influences on AM FRP structures was built.

The aim of the second section is to understand the structural performance of the plain-weave composite materials fabricated through autoclave curing containing one hole and two interacting holes in different configurations. The holes have significant role in industrial applications of composite structures. Most part of this section is

an experimental work. There has been no research on the multi-instrument investigation of damage propagation of plain-weave composites with two interacting holes. In final section, stacked ML algorithms were utilized for the first time to highlight the important application of AI in the prediction of the structural integrity of plain-weave composite structures with interacting holes under tension. As a novelty, the possibility of performing continuous monitoring of loadings and degradation processes of FRP woven composites using SHM and NDT diagnostic methods were investigated. Additionally, various manufacturing and diagnostic methods of FRP woven composites were presented. The degradation processes of FRP structures with interacting holes were analysed through the integration of numerical methods and multi instrumental investigation techniques. The experimental works, which were the combination of IRT, DIC, and FEM methods were utilized to further compliment the results given by numerical models. The PSC and EPSC techniques were applied to predict the strength of woven composite structures and the deficiencies of these models were shown through the experimental investigations. Fractography analysis were later discussed to analyze the damage initiation and failure propagation for different samples.

The final goal of the final chapter of this thesis is to show the potential application of new ML model through employing a large data-set given by the combination of numerical simulation and Python Macro code. The possibility of using small number of data to predict large domain of data-set was studied and the prediction accuracy was given. Overall, this model leads to less experimental and labor cost while decreasing the time required for numerical simulations.

Based on the literature review, the following thesis could be formulated.

It is possible to perform continuous monitoring of loadings and degradation processes of FRP composites using SHM and NDT diagnostic methods.

Research of this thesis poses various challenges and rise several questions. How FBG sensors embedded while AM process and how temperature gradient affects the structural performance of CFRP specimens? Furthermore, the influence of temperature and embedded FBG sensors on fracture mechanism of CFRP structures was investigated during the tensile test. It was shown how CFRP elements with embedded FBG sensors can be treated as simple smart structures. The degradation process of woven composites with two interacting holes are investigated for the first time. Stacked ML algorithms are applied to these structures to predict the maximum tensile stress in the vicinity of the holes. These challenges are tackled as below:

- Modelling and simulation of AM smart composites
- Manufacturing technology of CFRP with embedded FBG sensors
- Identification of mechanical properties of AM smart structures
- Environmental factors influence on AM smart structures
- Verification of the proposed AM method for CFRP structures
- Manufacturing of woven composites
- Numerical modelling of the woven composite
- Application of different measurement techniques to verify the numerical models developed for the woven composites with interacting notches
- Application of ML for the prediction of maximum tensile stress in the vicinity of drilled holes in different configuration in the woven composite plates

2.4 Outline of the thesis

There are six chapters in this thesis. An introduction, motivation, and literature background to AM of CFRP embedded FBG sensors, structural performance of plain-weave composites with two interacting notches, and ML prediction of mechanical performance of these structures are provided in Chapter 1 and Chapter 2.

In Chapter 3, the method used for the fabrication of CFRP through FDM and the process of embedding FBG sensors are explained in detail. An experimental study using an environmental chamber is further discussed. FEM is utilized to model the sample and the verification with an experimental study is provided. For further complement this chapter, the influence of temperature on the composite material mechanical properties was analysed after tensile test.

The application of multi-instrument techniques including IRT and DIC is studied in Chapter 4, to understand the damage propagation of plain-weave composites with two interacting holes in different configurations and predict the SCF for each specimens under tension. FEM is also employed to obtain SCF for each sample and the comparison is carried out between numerical and experimental works.

In Chapter 5, the stacked ML model is used to predict the maximum tensile stress in the vicinity of the holes and an experimental verification is also provided for the numerical simulations.

The summary, conclusion, and future works required for further development of this thesis are discussed thoroughly in Chapter 6.

3. AM for CFRP embedded FBG

The AM method utilized for fabrication of CFRP structures embedded FBG sensors following with the comprehensive results and discussion of the thermal and tensile tests were discussed in this part.

3.1 Materials and methods

FDM technique used for manufacturing the samples, thermal loading test, numerical simulation using ABAQUS were explained in this section.

3.1.1 Additive Manufacturing of CFRP

The CFRP sample was additively fabricated through the adjusted FDM strategy created by the project partner (Kaunas College of Innovation, Lithuania) by using their printing head (Rimašauskas, Kuncius & Rimašauskienė, 2019). The view of additive manufacturing tool (ECREATOR2 Shenzhen Getech Technology) and the CFRP samples is represented in Figure. 3.1. Two types of continuous fiber could be used in FDM method: non-impregnated carbon fiber and pre-impregnated carbon fiber. The first solution required proper impregnating conditions in the printing head. Therefore, the structure of the 3D printer is more complex but the whole process is performed in one place. Pre-impregnation of fibers allows for better control of the process but the whole process could not be conducted at one place and is more time consuming. On the other side, the structure of the 3D printer is more simple and technological process of manufacturing of elements is easier, due to the surface properties of the fibres. The main idea of the 3D printer modification performed

by the KTU team, was related to replace two separated heads (for polymer and fibre) by one designed for pre-impregnated fibre. The impregnation process was also designed by KTU. It contains heating of the non-impregnated fibre to 220 °C, chemical treatment of the fibre surface and covering the fibre by PLA layer. Such prepared fibres are then used in the AM process.

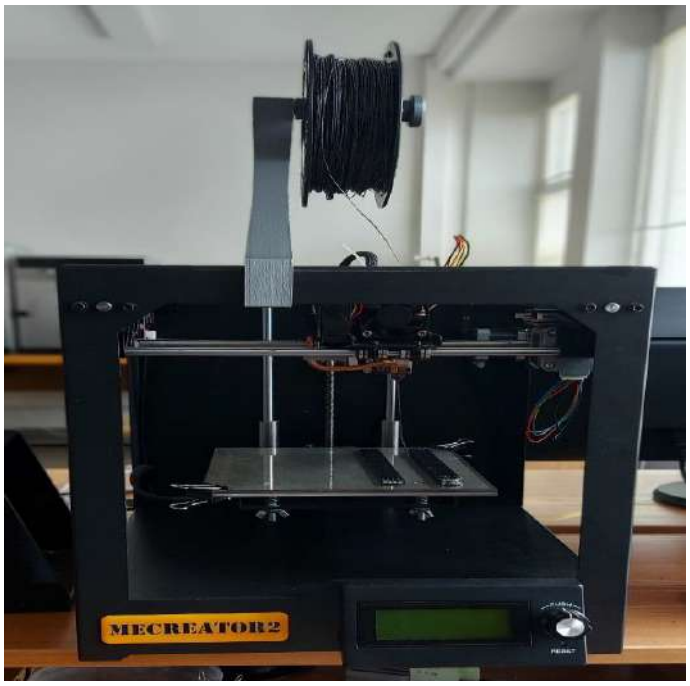

Figure 3.1 AM machine (MECREATOR2 Shenzhen Getech Technology Co.,Ltd) with an additively manufactured sample while printing (Taken from Kaunas University AM lab)

Its advantage is that the carbon fiber and polymer are blended in a secured space at high pressure and temperature, enhancing the adhesion and bringing down the chance of delamination. Dimensions of the printing head are decreased and 3D printing process will not be complicated due to the one-nozzle nature of the system. Fabricated CFRP specimens are consisted of four layers of Polylactic Acid (PLA) matrix and continuous carbon fibre reinforcement. PLA was chosen since it is bio-degradable and environmentally friendly polymer, which might be produced by natural resources. Each layer has 0.5 mm of thickness and the specimens has total thickness of 2 mm. The length and width of the samples were 150 MM and 15 mm respectively. Five specimens with same conditions were printed in order to ensure the repeatability of the results. For the purpose of determining the influence of embedded FBG sensor on the material durability, five different samples were manufactured without optical sensors and five included them. The number of specimens were selected to fulfill the requirements of statistical tests.

The novelty of this part is to ensure the applicability of embedded FBG sensors to strain measurement of the CFRP materials under thermal and mechanical loading. For the embedded FBG sensor, which was located in the mid-layer of the specimen the following steps are taken: print half of a specimen, insert the FBG sensor in the through-hole while maintaining tension, then bond the FBG in place using cyanoacrylate before printing the other half of the specimen. The FBG is kept tensioned by taping both ends to defined areas on the 3D printer bed. The printing process is very slow, and since the print chamber is open, it was not necessary to interrupt the printing process to embed the FBG sensor. Table. 3.1 provides the printing parameters. It should be mentioned that the printing speed was set to a low value in order to have the least amount of voids and defects during the printing.

Table 3.1 Printing parameters for manufacturing the CFRP specimens

Layer height (mm)	First layer speed (mm/s)	Printing speed (mm/s)	Extruder temperature ($°C$)	Bed temperature ($°C$)	Extrusion multiplier (mm)	Extrusion width (mm)	Fan speed (%)
0.5	1.20	4	200	70	0.6	1.6	50/80/100

An example of FBG sensor spectra after and before embedding is shown in Figure. 3.2. It was seen that embedding resulted in the decrease of sensor reflectivity or amplitude for ca. 50%. However, the spectrum shape was not affected. Thus, the embedded sensors could be used for measurement purpose.

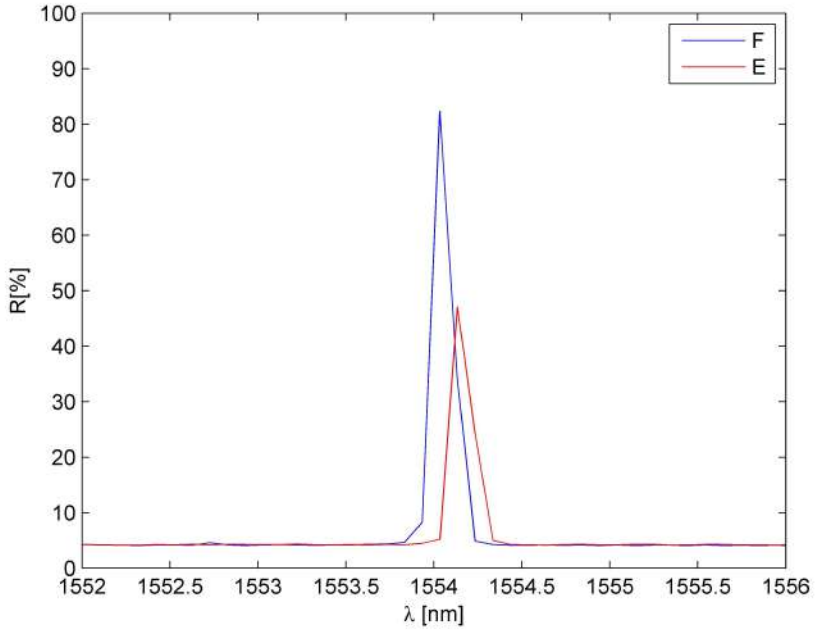

Figure 3.2 FBG sensor spectra: E – after embedding, F – free,

Additively manufactured CFRP sample embedded FBG sensor is represented in Fig. 3.3. The primary axis of the samples was parallel to the orientation of the FBG sensor and the polymer sample was reinforced with carbon fibers.

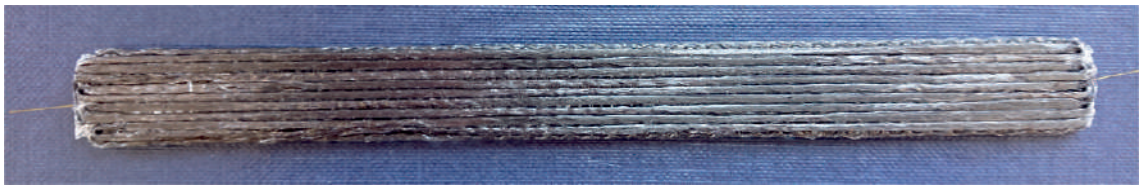

Figure 3.3 3D printed CFRP specimen containing FBG sensor

As the reinforcement, Toray's T300B-1000 carbon fiber with a diameter of 1.75 mm was chosen, while PLA with DR3D Filament of 1.75 μm was used for the matrix. Table. 3.2 provides the mechanical properties of the CRFP constitutes for 20 °C, which were given by both an in-house experimental tests and manufacturer recommendation. As obviously seen, the mechanical performance of fiber are way much higher than the polymer matrix except for the heat capacity. 25% carbon fiber volume fraction was utilized for all the fabricated specimens.

Table 3.2 Mechanical properties of matrix and fiber

	E [GPa]	ρ [g/cm^3]	ν	X_t [MPa]	v [%]	κ [W/mK]	C [J/Kg.C°]
Fiber	230	176	0.33	3530	24.5	10.46	794
Matrix	2.315	1.24	0.29	51	75.5	0.13	1800

3.1.2 Environmental chamber (thermal loading)

An environmental chamber, the MyDiscovery DM600C (made in Italy by Angeltoni Test Technologies Srl), was utilized to measure the effect of temperature gradient on the AM CFRP samples. It was illustrated in Figure. 3.4 provided by IMP PAN thermal laboratory.

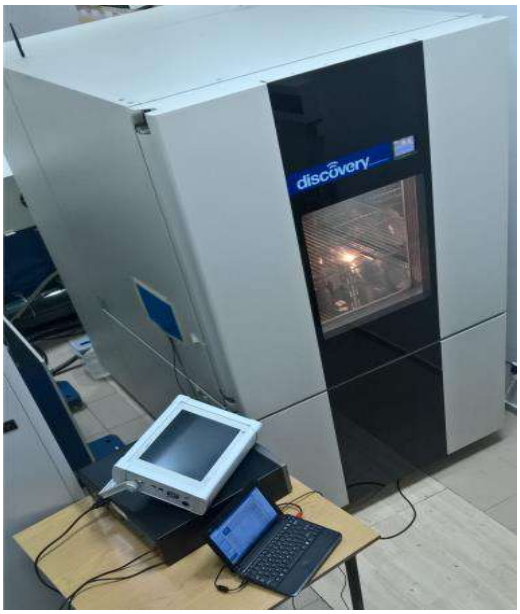

Figure 3.4 MyDiscovery DM600C chamber (IMP PAN laboratory)

specification parameter of this chamber was shown in Table. 3.3.

Table 3.3 MyDiscovery DM600C parameters

parameter		value
temperature		-75°C±180°C
temperature fluctuations		±0.1°C±0.3°C
relative humidity		10%+98%
temp change rate	heating	4.5°C/min -70°C+180°C
	cooling	4°C/min +180°C-70°C
relative humidity fluctuations		±1%±3%

The temperature influence test was separated into two sections: elevated temperatures enhancing from 10 °C to 50 °C, and subzero temperatures falling from 10 °C to -50 °C. It should be highlighted that the temperature increasing/decreasing process was slow enough to ensure quasi-static conditions. The temperature in the whole sample volume was the same. The assumption in both situations was a 5°C step between consecutive temperatures and the heating/cooling velocity of ca. 0.2°C/min. The sample was kept on a shelf throughout the investigation to allow it to expand or contract in all directions. FBG temperature probe was used to measure the temperature around the sample. The measurement was conducted through an Interrogator

si425-500 from Micron Optics. The measurement frequency was 1 Hz during the experiment. Also, the relative humidity was set to be 20%. Analyzed specimens for elevated and sub-zero temperatures were subjected to temperature as illustrated in Figure.3.5.

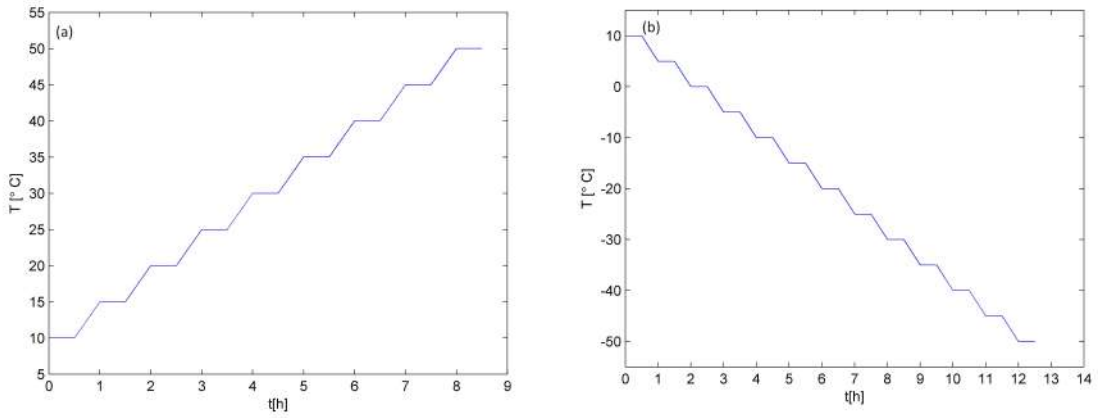

Figure 3.5 Program assigned for an environmental chamber for the CFRP specimens (a) elevated, and (b) sub-zero

3.1.3 Numerical Simulations

FEM is a well-known technique for numerically resolving differential equations that appear in mathematical and engineering problems. FEM is generally utilized to solve the complex problems, which could not be easily solved analytically or the costs associated with experimental tests impedes conducting numerous tests to evaluate a design. In order to solve a problem, the FEM breaks down a complex system into smaller, more easily understood parts known as finite elements.

FEM was employed to describe the thermal performance of the CFRP samples and compare it with the experimental outcomes. The effect of temperature (elevated and sub-zero) on the CFRP sample could be analyzed in ABAQUS CAE software through coupled displacement-thermal solver. Thus, the numerical calculations for both sub-zero and elevated temperatures were conducted by Abaqus CAE software. Ply-by-ply method was used in order to model the composite structure within the software. In this approach, 3D deformable solid is partitioned to the number of layers in the composite structure, which are 4 layers here. Thereafter, based on the stacking sequences the of the CRFP structure, orientations were input for each layer separately. Uni-directional sample was considered for test.

Also, the emissivity of $\varepsilon = 0.96$ was taken into account for the CFRP specimen because it was subjected to the thermal radiation inside an environmental chamber. It is worth noting that the radiation was implemented to all surfaces because they were exposed to the ambient temperature. For the thermal conductivity which is an important factor in thermal behavior of composite, serial and parallel techniques were employed to find the composite properties. The thermal conductivity along the transverse and longitudinal directions to the fibre were provided by:

$$\kappa_t = \frac{k_f k_m}{k_m v_f + k_f v_m}, \tag{3.1}$$

$$\kappa_u = k_f v_f + k_m v_m. \tag{3.2}$$

Moreover, the coefficient of thermal expansion for transverse and longitudinal direction to the fiber were given by:

$$\alpha_{11} = \frac{v_f \alpha_f E_f + v_m \alpha_m E_m}{v_f E_f + v_m E_m}, \tag{3.3}$$

$$\alpha_{22} = \alpha_f v_f + \alpha_m v_m. \tag{3.4}$$

where α_m, α_f, v_m, and v_f are the coefficient of thermal expansion and volume fraction of matrix and fiber, respectively. These data were input to the ABAQUS in material module. The CTE values strongly depends on temperature and the values used in ABQUS were achieved experimentally. It was determined for dense number of Temperatures than for CFRP to have possibility to calculate CTE for ranges of temperatures.

Coupled displacement temperature solution is selected to run the simulation. FEM model consists of Quadratic hexahedral completely integrated elements (9000 numbers of (C3D20RT) elements) containing a total number of 45069 nodes. The boundary conditions were adopted based on the settings of experimental study. The sample position in the environmental chamber on the shelf was also considered while defining the boundary conditions in ABAQUS CAE. One side of the sample was

restrained to move along the fiber direction (x-direction) while the perpendicular side was restricted in y-direction to allow expand or contract. Finally, the bottom part of the sample was restricted from moving in the thickness direction since it was put on the shelf as shown in Figure. 3.6.

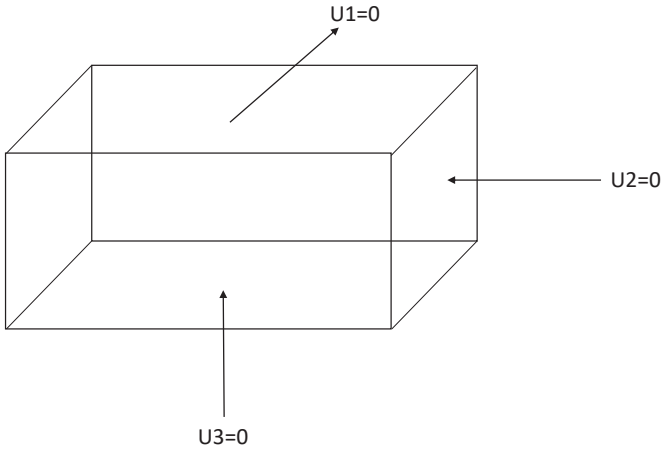

Figure 3.6 Boundary conditions

Furthermore, time-amplitude loading was applied for sub-zero and elevated temperatures. These temperatures were same as the ones given to the settings of the environmental chamber. Predefined temperature of 20 °C was assigned to the sample as it indicated an ambient temperature and the sample was exposed to this temperature initially. The mechanical attributes were given to ABAQUS within properties module, were provided in Table. 3.2, which was given to the software through properties module. Mesh independency check was needed in order to ensure the correctness of the results. Therefore, a mesh convergence study was carried out to find an optimum number of elements inside the model and to ensure that the mesh is dense enough. 1 mm edge seed size was chosen to input inside mesh module in ABAQUS in order to get correct result values. Reduction of the mesh numbers did not influence the results and it was not justified since it affect the costs associated with the computation. Figure. 3.7 illustrates the mesh dependency study for CFRP sample.

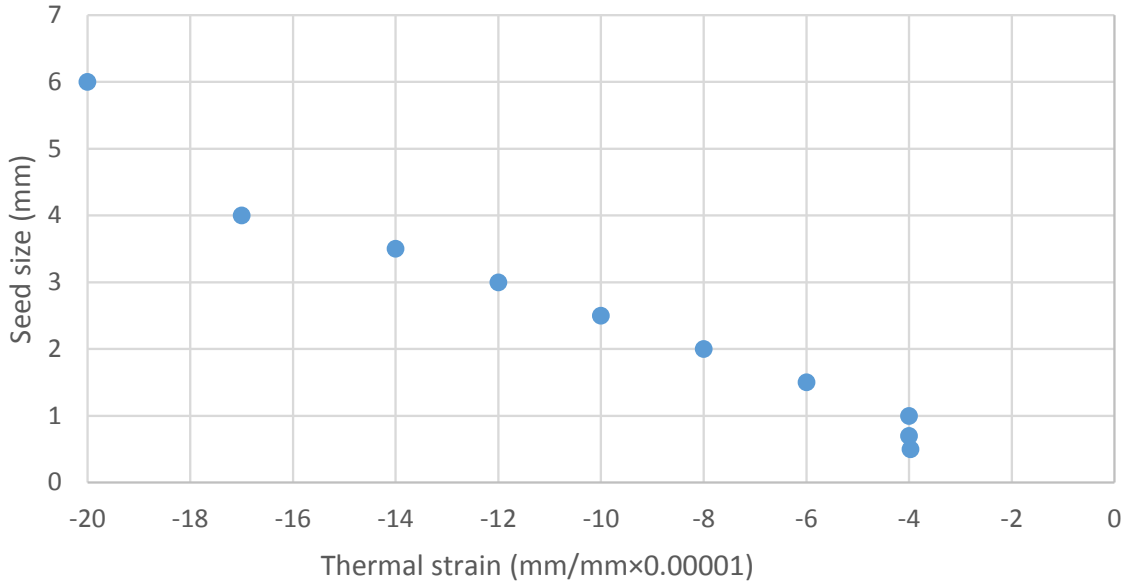

Figure 3.7 Mesh independency study

Fig. 3.8 displays the sample that was modeled in Abaqus as well as the boundary conditions. For both the elevated and sub-zero temperatures the same model with the same mesh were utilized, but with different temperature gradient for each sample. The temperature was read through the environmental chamber during the experiment in each defined time-slot and input to the amplitude section of the ABAQUS in numerical simulation.

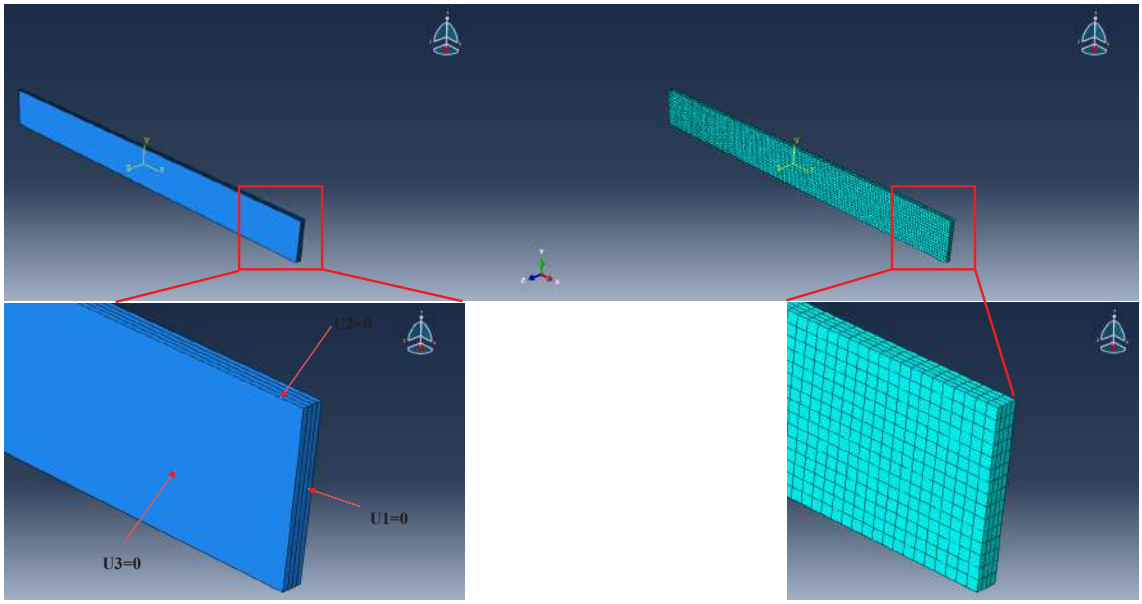

Figure 3.8 FEM model, Boundary conditions and mesh

3.2 Results and discussion

In this section, results of the thermal tests as well as the tensile test conducted on the CFRP samples embedded FBG sensors were explained.

3.2.1 Thermal test

As previously mentioned, the effect of temperatures on the CFRP specimens was investigated numerically and experimentally. The specimens were subjected to various temperature values. It should be mentioned that, the maximum temperature was attributed to glass transition temperature (T_g) of the PLA material. Typically, the Tg of PLA is within 50 °C and 70 °C range (Cristea, Ionita & Iftime, 2020). PLA has approximately low deflection temperature value as of 42 °C based upon the dynamic Mechanical Analysis (DMA), carried out on the PLA material.

The CTE of the PLA was taken by experimental tests. These tests were performed on the sample fabricated on the exactly same conditions as for CFRP specimens. The only difference was that there was no fiber reinforcement in this sample. The width, length, and thickness of the fabricated sample were 20mm, 50mm, and 10mm, respectively. As usual, an FBG sensor was put between layer two and three of the sample. It is worth highlighting that despite the fact that the reflectivity was lower there was no spectrum distortions. Therefore such sensors can be used for strain measurements. The sample photo of PLA sample included FBG sensor is shown in Figure. 3.9.

Figure 3.9 PLA sample embedded FBG sensor

The correlation between the strain and temperature for the host material was calculated through:

$$\varepsilon_T = \frac{1}{n}\sum_{i=1}^{n}\varepsilon_n(T_i)\ for\ i = 1,...,m;\ n = n_1,...,n_n; \tag{3.5}$$

It is worth mentioning that the values for CFRP were calculated in the same way. Additionally, all measurements in the environmental chamber were repeated twice. Temperature level T_i was attributed to the averaged temperature value from n points for stable temperature conditions for the duration of 300 s. The error measured for temperature was 0.36 °C, while for the strain it was $3.6\times\ 10^{-6}$. The measurement accuracy of the interrogator is $1\times\ 10^{-6}$ m/m.

Figure. 3.10 represents the strain values determined for the PLA material. It is obvious that after 42 °C, the correlation behavior between temperature and strain was not same as below 42 °C. It could be attributed to the following:

$$\varepsilon^a_{PLA}(T) = P_1T + P_2. \tag{3.6}$$

Where, P_1 and P_2 are the varaibles utilized for approximation. The linear approximation is represented with a black line in Figure. 3.10. The measurement point for 45 °C did not lay on the previous straight line; hence, a correction was introduced. This anomaly was attributed to the deflection temperature of the PLA material. Therefore, the connection between temperature and strain for above 40 °C temper-

atures was approximated employing linear correlation but with different polynomial constants. This is called piecewise linear interpolation. The approximation was depicted as a red line in Figure. 3.10. Polynomial constants are provided in Table. 3.4.

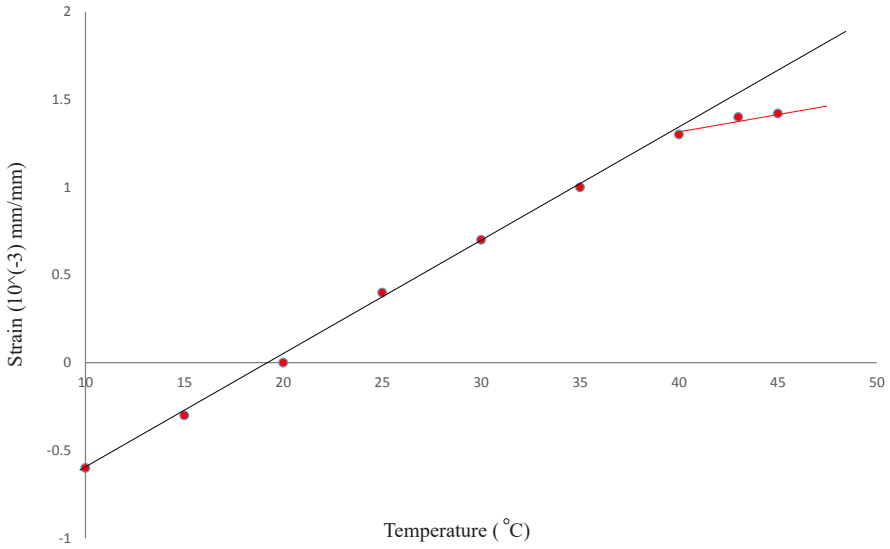

Figure 3.10 strain-temperature graph for PLA material

Table 3.4 Polynomial constants

	First approximation	Second approximation
P_1	7.4	2.2
P_2	-149.55 0	59.58
Corresponding line	black	red

The CTE was the first derivative of Eq. 3.6 calculated by:

$$\alpha(T) = \frac{\partial \varepsilon(T)}{\partial T}. \tag{3.7}$$

Therefore, the CTE for the PLA matrix was 2.20x10^{-5} m/m°C for temperatures above 40°C and 7.40x10^{-5} m/m°C for temperatures below 40°C. This behaviour was same as what discussed in (Economidou & Karalekas, 2016) which it was given by FBG sensor put into ABS via FDM technique. There are observed differences between the PLA material behaviour and the previously exterminated M3 crystal, also manufactured using a 3D printer (Mieloszyk et al., 2020). The correlation between

temperature and strain for for M3 crystal was defined through second degree polynomial specifically for the temperatures lower than the glass transition temperature. This difference not only associated with the material attributed but also the utilized fabrication method. The M3 crystal specimens were manufactured using multijet printing technique, whereas the PLA was fabricated via FDM. The MJP provided high accuracy of elements (the layer thickness is equal to 16 μm). However, it could not be employed to the fabrication of CFRP elements (Mieloszyk et al., 2020).

The behavior of CFRP sample in sub-zero temperature was relatively different in elevated temperatures such that in the sub-zero temperatures, the strain gradually decreased but in the elevated temperature after gradual enhancement until around 40°C the thermal strain showed different behavior and it started to decrease sharply. This anomaly is possibly associated with low heat deflection temperature of PLA inside CFRP. PLA itself has heat distortion temperature nearly at 55 °C, whereas mixing the carbon fibres decrease the temperature to around 42 °C. The procedure of carbon fibres preparation before printing process influenced cross-lining. It influenced heat distortion and glass transition temperatures of PLA matrix. It is worth mentioning that the strain gauge factor of the FBG sensor was equal to 1.3 pm/ε. Furthermore, the temperature sensitivity of the FBG was 11.2 pm/°C.

An average thermal strain given by numerical simulation for one time slot of elevated temperature is represented in Figure. 3.11. The constant value of strain for that time-slot was observed, as an averaged thermal strain was captured for the results since it could give insight for the comparison of numerical and experimental results.

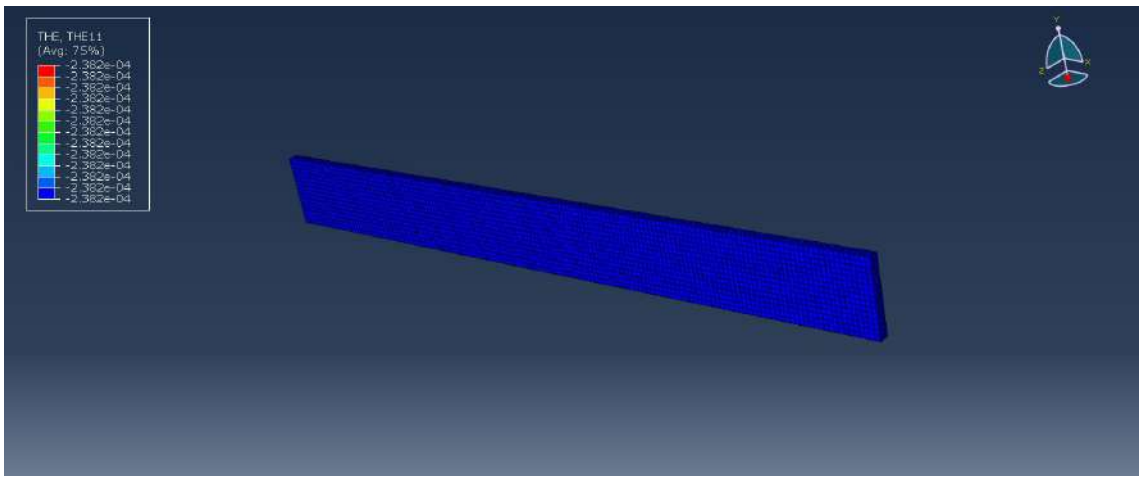

Figure 3.11 Average thermal strain for the first time-slot in elevated temperature

Strain values given by experimental test and simulation in above zero temperature for CFRP sample with embedded FBG sensors is provided in Table. 3.5. The thermal strain obtained by numerical work in each time-step was the average strain

calculated by the software within the specimen. The average difference between the experimental and simulation was around 6%. The difference was found by subtracting the value of numerical outcome from the result given by experimental test in which the result was divided by the experimental result for each temperature as following:

$$Err = (\frac{\varepsilon_{num} - \varepsilon_{exp}}{\varepsilon_{exp}})100\%. \tag{3.8}$$

Then, the average of all values was taken into account as a final outcome. There are several reasons associated with the difference between the thermal strain extracted by the embedded FBG sensor and those given by Abaqus simulation. In the Abaqus the specimen was considered to be an ideal specimen and any possible voids/gaps were neglected. Furthermore, environmental effects were not considered in Abaqus modeling. It is worth mentioning that the difference was negligible enough to be disregarded; Hence the numerical study was verified with experimental test. The experimental values were determined as arithmetic average from 3 samples. The average difference between strain values was 5×10^{-6}m/m.

Table 3.5 Exp. versus Num. strain values (elevated temp.)

Temperature (°C)	Num. ($\times10^{-5}$)	Exp. ($\times10^{-5}$)	Error (%)
	ABAQUS	FBG	
10	-3.95	-4	1.25
15	-2.38	-2.3	3.3
20	0.1	0.12	16
25	1.95	2	2.5
30	4	4.1	2.4
35	6	5.94	1
40	6.12	6.16	0.6
45	8	8.2	2.4

Figure. 3.12 shows the numerical and experimental values for the elevated temperatures. Though the difference is a bit more than the subzero temperatures, but still it could be claimed that for elevated temperatures FBG sensors could be utilized to capture the thermal strains.

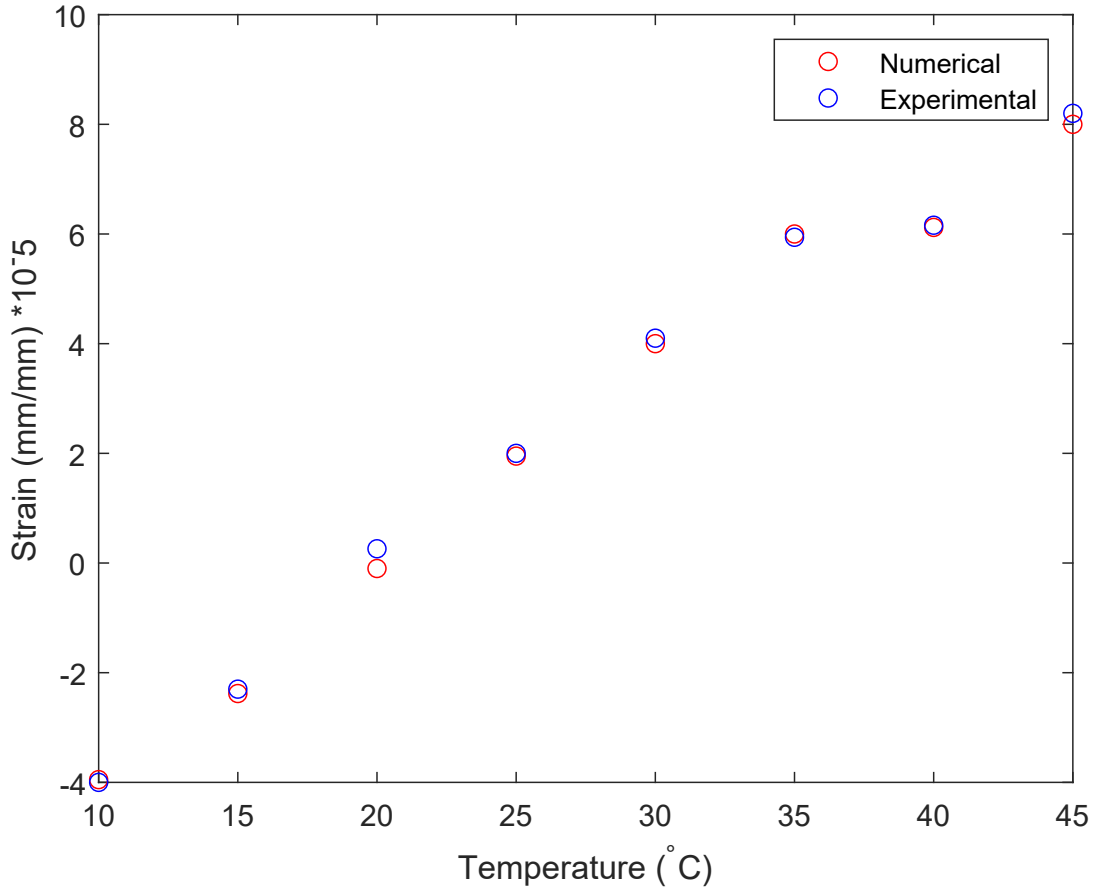

Figure 3.12 Comparison of CFRP strain for elevated temperatures

An average thermal strain obtained through numerical work for next time slot is shown in Figure. 3.13.

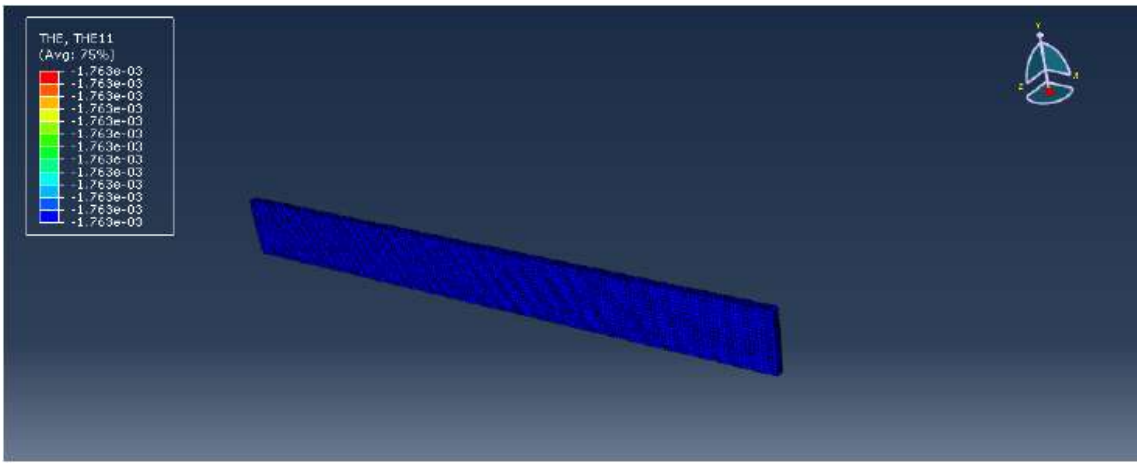

Figure 3.13 Average thermal strain for the second time-slot in elevated temperature

Table. 3.6 provides a comparison of strain values between Abaqus and experiment

for CFRP specimen for temperatures below zero. The average difference between the experimental and numerical values obtained through FBG sensor was approximately 4% which was calculated by Eq.3.8. Thus, for temperatures below zero the FBG embedded sensor could also capture the correct thermal strain values.

Table 3.6 Exp. (FBG) Vs. Num.(ABAQUS) strain values (subzero temp.)

Temperature (°C)	Num. ($\times 10^{-4}$)	Exp. ($\times 10^{-4}$)	Error (%)
	ABAQUS	FBG	
-50	-1.8	-1.78	2.5
-40	-1.6	-1.63	1.8
-30	-1.4	-1.4	0
-20	-1.18	-1.2	1.6
-10	-0.95	-1	5
0	-0.7	-0.65	7.7

Figure. 3.14 represents the values given by experimental test as well as numerical simulation for subzero temperature. The experimental results were presented for the FBG sensor as an average mechanical strain values for stable temperatures during time steps. The results were well matched between the thermal strain values provided by FBG sensors and FEM. It was shown that embedded sensors had capability to measure the correct thermal strains for CFRP samples fabricated by FDM.

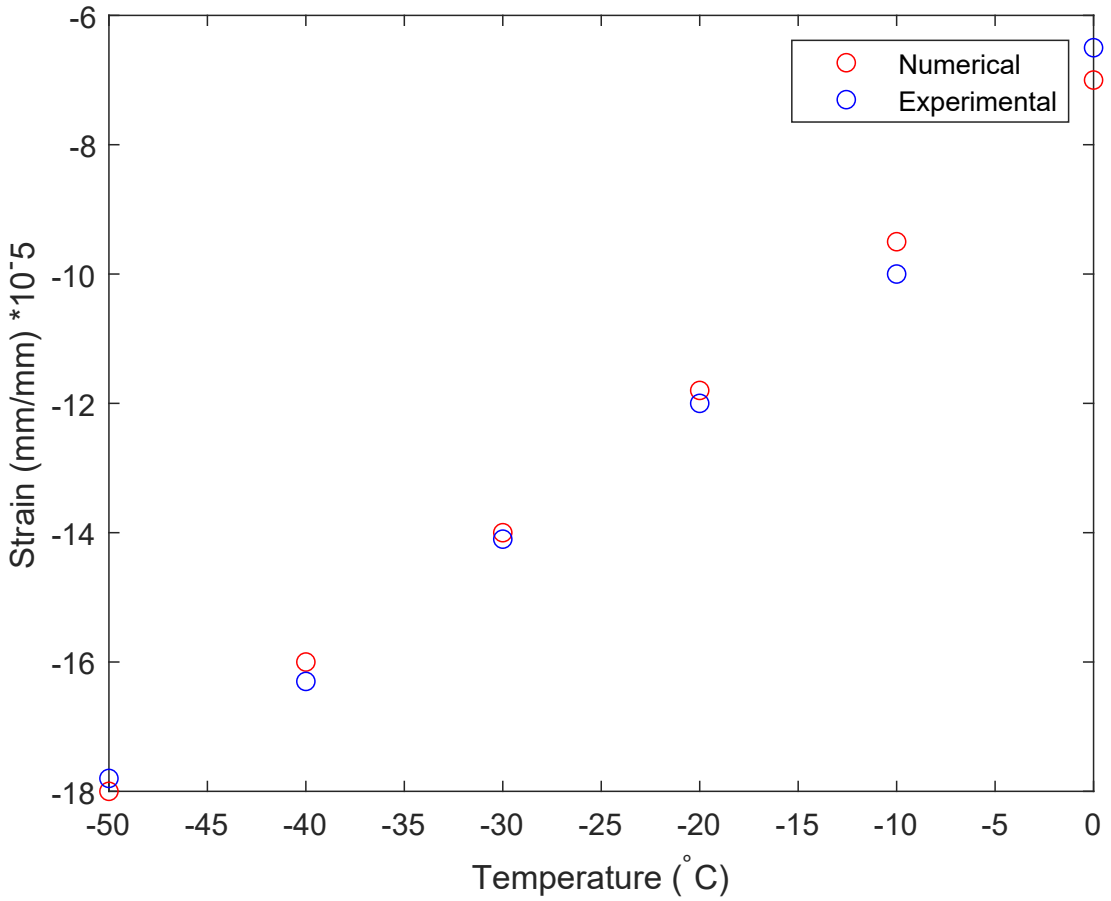

Figure 3.14 Comparison of CFRP strain for subzero temperatures

Thermal strain distribution for the CFRP sample in sub zero temperatures for -20°C is depicted in Figure. 3.15. As highlighted for the samples in elevated temperatures, the outcomes of ABAQUS software were average thermal strain. Therefore, the distribution of thermal strain throughout the sample was consistent.

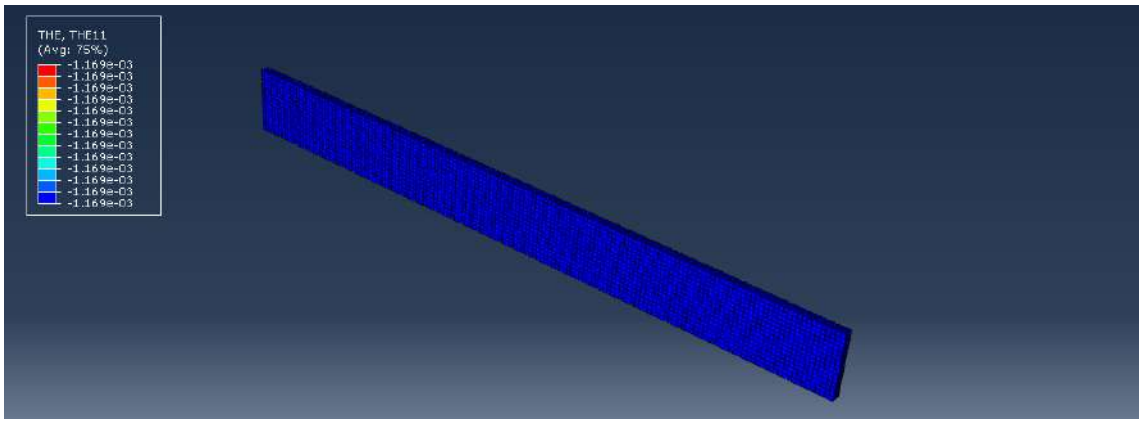

Figure 3.15 Average thermal strain for the -20°C in sub-zero temperature

3.2.2 Tensile test

In this section, the influence of FBG sensors on the mechanical structure of the AM FRP structures for elevated and sub-zero temperatures was discussed. The samples (without the thermal treatment and after the thermal treatment) were subjected to the tensile test. The tensile test was performed on groups of samples as 5 from each case. Its aim was to determine the embedded fiber optic influence on the FRP material durability. The tensile tests were performed on universal static-dynamic testing machine HT-9711-25 (Hung Ta, Korea). During the tensile test the same interrogator was used but the measurement frequency was 250 Hz.

The averaged tensile strength of FRP after the thermal test was in the range of 170 MPa to 180 MPa regardless of the FBG sensors occurrence. It was observed that the temperature positively influenced on the sample structure especially PLA matrix as it is the material that connect carbon fibre bundles together. The averaged tensile strength of FRP after manufacturing was in the range of 110 MPa to 120 MPa regardless of the FBG sensors occurrence. It was concluded that the sensors influence on the AM CFRP material is very limited. Such differences in mechanical characteristics suggests changes in CFRP material internal structure. Stress strain graph for AM FRP sample before and after thermal test were shown in Figure. 3.16.

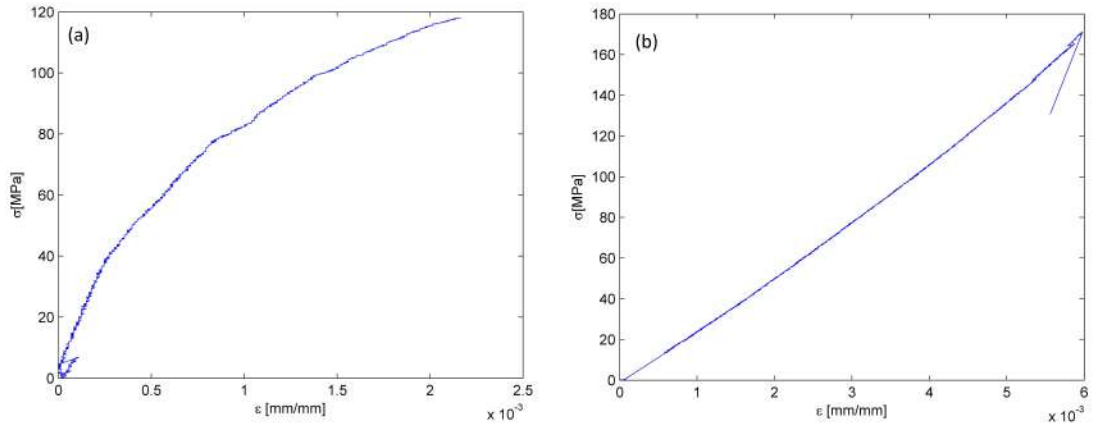

Figure 3.16 Stress-strain plot of tensile test: (a) without thermal treatment, (b) after the thermal treatment.

The strain measured by extensometer and embedded FBG sensors after manufacturing, before and after heat treatment with respect to time were shown in Figure. 3.17 (a), and (b), respectively. We can see strong similarities between FBG and extensometer for the sample after manufacturing. The main difference ca. 0.5e-3m/m was observed at the end of the process. The differences in the strain values and the angle was probably a reason of a local character of the FBG sensor and the

internal structure of AM sample. For the sample after the thermal treatment the strain curves almost overlap. The main differences between the curves was equal to 34e-5m/m. The observed in FBG sensor measurement rapid strain increasing and then decreasing was related to puling out the optical fibre. The optical signal was registered by a few seconds after the end of the test. However, the strain values for stable part of the measurements were lower than for the beginning of the test.

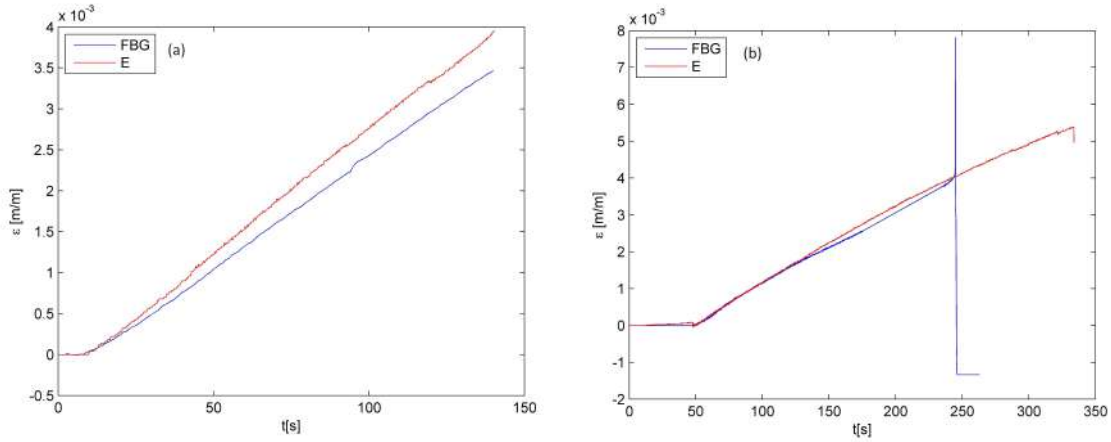

Figure 3.17 strain measured by extensometer for tensile test: (a) without thermal treatment, (b) after the thermal treatment.

Also, Figure. 3.18 compares the fracture of the sample before and after heat treatment process by providing the photo of real sample and the fractography pictures. Two different fracture mechanisms were observed. For the sample after manufacturing the breaking process of the carbon fibre bundles was observed. The sample was divided for two separated parts. While for the sample after exposition to elevated temperature, only parts of the fibres were broken while some of the carbon fibre bundles were still connected.

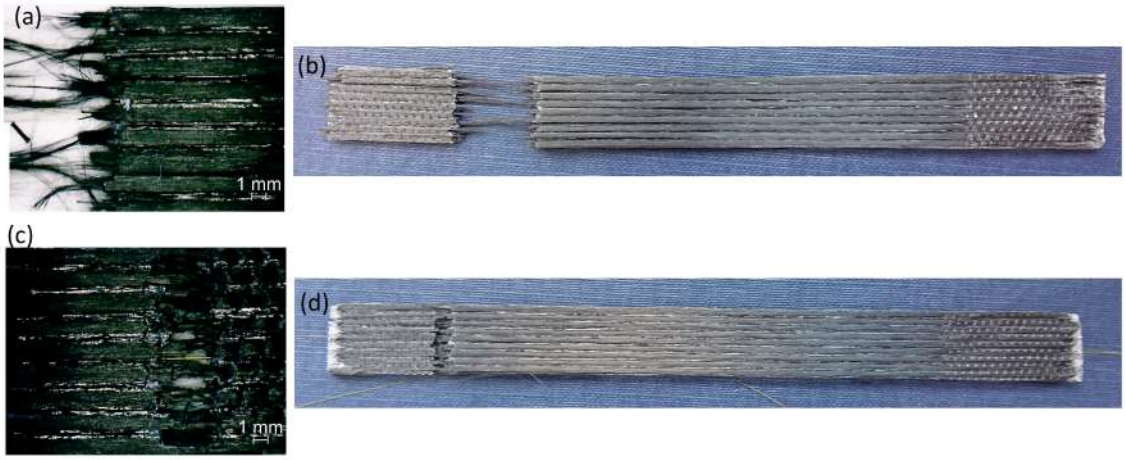

Figure 3.18 Photo of fracture of the samples and fractography for elevated temperatures, (a), (b) before treatment; (c), (d) after treatment

A comparison of the scanning electron microscopy (SEM) photograph of two samples (intact and after heat treatment) after the tensile test is presented in Figure. 3.19. The PLA layer for the sample after manufacturing does not fill the whole area between neighbouring carbon fibre bundles. Therefore, the fibre bundles are not perfectly connected. It resulted in breaking of the fibres during the tensile test. The elevated temperature resulted in filling the entire area between carbon fibre bundles by PLA matrix. It resulted in better connection between the neighbouring parts and higher ultimate strength values.

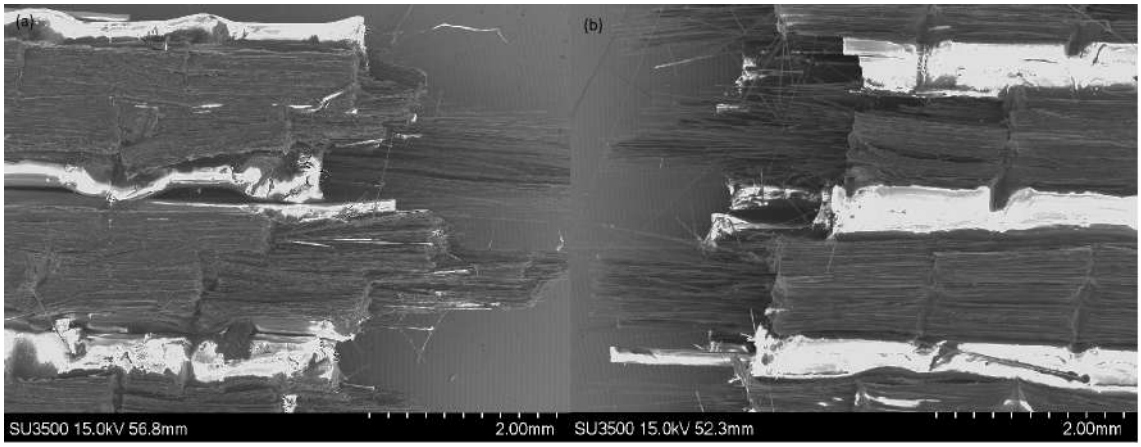

Figure 3.19 SEM results for samples after the tensile test for elevated temperature treatment: (a) without thermal test, (b) after the thermal test.

The same investigation was conducted for the heat treated samples in sub-zero temperatures. The stress-strain graph as well as the strain measured by extensometer and embedded FBG sensors after manufacturing, after heat treatment in sub-zero temperatures were shown in Figure. 3.20 (a), and (b), respectively. The mechanical stress is the lowest from all analysed groups of samples. Also for the samples exposed to subzero temperatures the FBG sensor do not influenced the stress values and were equal to 100-120 MPa. The differences in strain curves determined by extensometer and FBG sensors are probably effect of local (FBG sensor) and global (extensometer) characters of the measurement units and heterogeneity of the sample structure.

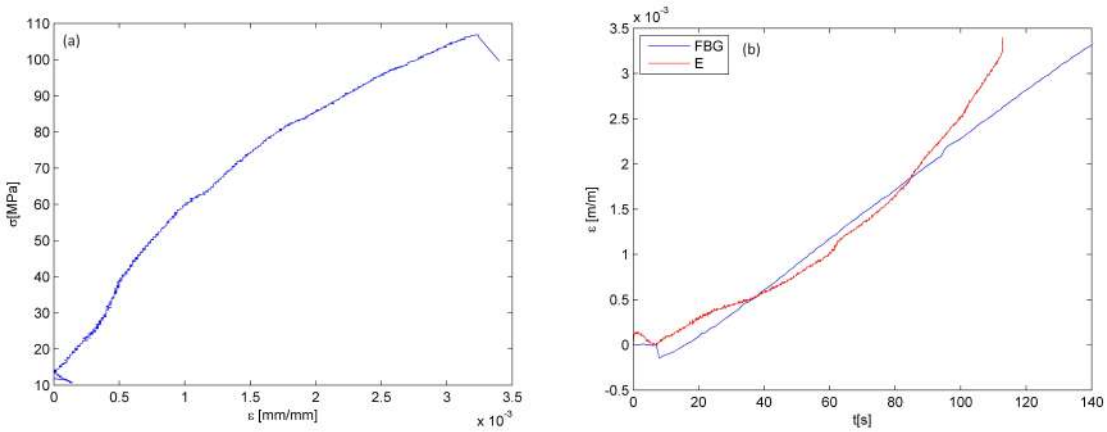

Figure 3.20 (a) Stress-strain for tensile test after exposure to subzero temperature, (b) strain measured by extensometer for tensile test after thermal treatment in subzero temperature

The SEM photograph of the sample after the sub-zero treatment and fracture (optical microscope) of sample are represented in Figure. 3.21. For such samples both carbon fibre breaking and matrix cracking were observed. The subzero temperatures, probably resulted in Crystallization occurrence in PLA matrix.

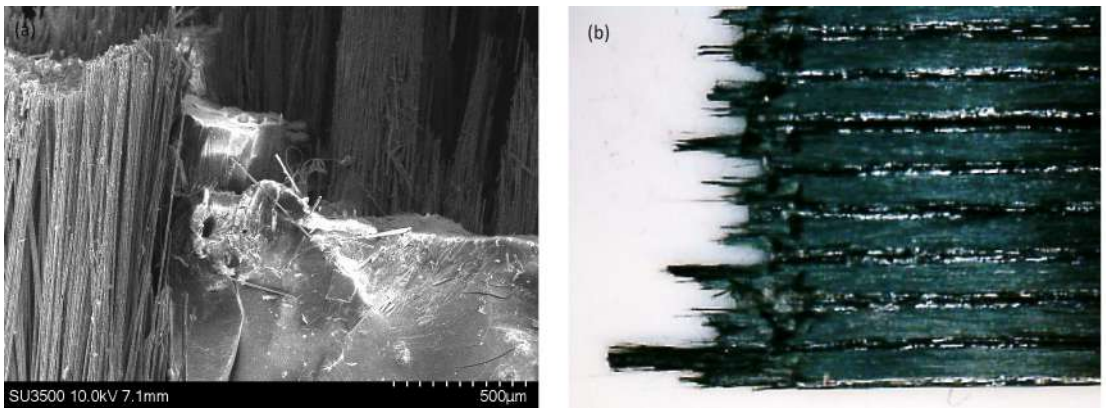

Figure 3.21 (a) SEM photograph of the sample after the sub-zero treatment, (b) fracture (optical microscope) of sample after exposure to sub-zero temperatures

The fracture happened while tensile test for the sample subjected to the sub-zero temperature is illustrated in Figure. 3.22.

Figure 3.22 Fracture of the sample subjected to sub-zero temperature

FBG sensors can be embedded into the additively manufactured CFRP material. The sensors can be applied for strain measurements during thermal loading and mechanical loading (tensile test). The influence of FBG sensors on mechanical durability of CFRP is negligible. FBG Sensors do not influence on mechanical strength and the fracture mechanism.

4. Application of multi-instrument techniques

In this chapter the application of NDT methods in the estimation of tensile strength of plain-weave composites was discussed. The numerical study was conducted and the possibility of using PSC and EPSC criteria was explained.

4.1 Materials and methods

4.1.1 Experimental work

4.1.1.1 Fabrication of plain-weave composites

The pre-impregnated plain weave carbon fabric with the raw material code "KOM10 T700 HSCF 12KT PL600 40% 1250" is purchased from KORDSA in Turkey. The corresponding tests were conducted in composite technologies center of excellence in Istanbul, Turkey. High strength carbon fiber (HSCF) T700 12KT and epoxy resin with the commercial code OM10 make up the prepreg, which is intended for autoclave or press curing. The resin amount and fiber area weight 40% and 600 g/m2, respectively.

The following steps were followed when curing prepreg in autoclave according to the manufacturer's recommendation: (1) input full vacuum; (2) implement autoclave pressure of 7 bar gauge; (3) while the autoclave pressure reaches near to 1 bar gauge, decrease the vacuum to a safety value of 0.2 bar; (4) heat-up till 120°C at 1-

3°C per minute intervals; (5) keep at 120°C for 3600 seconds; and (6) finally decrease the temperature at 2-5°C per minute. The stacking sequence and thickness of the samples were $[0,90,0]_s$ and 3.636 mm, respectively. Cutting the specimens took place on a Poysan B5490 3 axis milling machine. Five tensile samples (longitudinal and transverse) and five v-notch shear samples were cut in accordance with ASTM D3039 and ASTM D5379, respectively, for the mechanical characterization tests of the material. The dimensions of the samples were provided in Table. 4.1, in accordance with ASTM D5766.

Table 4.1 Specimen geometries

Sample	ID	L[a]	W[b]	T[c]	HD[d]	SS[e]	HA[f]
Unnotched	-	250±0.1	36±0.1	3.636±0.05	6	$[0,90,0]_s$	-
Single hole	1H	±250±0.1	36±0.1	3.636±0.05	6	$[0,90,0]_s$	-
Two-holes transverse	2H0	±250±0.1	36±0.1	3.636±0.05	6	$[0,90,0]_s$	0
Two-holes diagonal	2H45	±250±0.1	36±0.1	3.636±0.05	6	$[0,90,0]_s$	45
Two-holes longitudinal	2H90	±250±0.1	36±0.1	3.636±0.05	6	$[0,90,0]_s$	90

[a] Length
[b] Width
[c] Thickness
[d] Hole diameter
[e] Stacking sequences
[e] Hole angle

Three hole configurations, without changing the hole diameter and distance between the holes, were considered for the samples with two notches. For the holes oriented parallel and transverse to the loading direction, an angle (θ) was specified as $\theta = 90°$ and $\theta = 0$°C, respectively. While, the third hole orientation was obtained by rotating the holes, in the plane of specimen, to $\theta = 45°$. The schematic view of the specimens' geometry was illustrated in Figure 4.1.

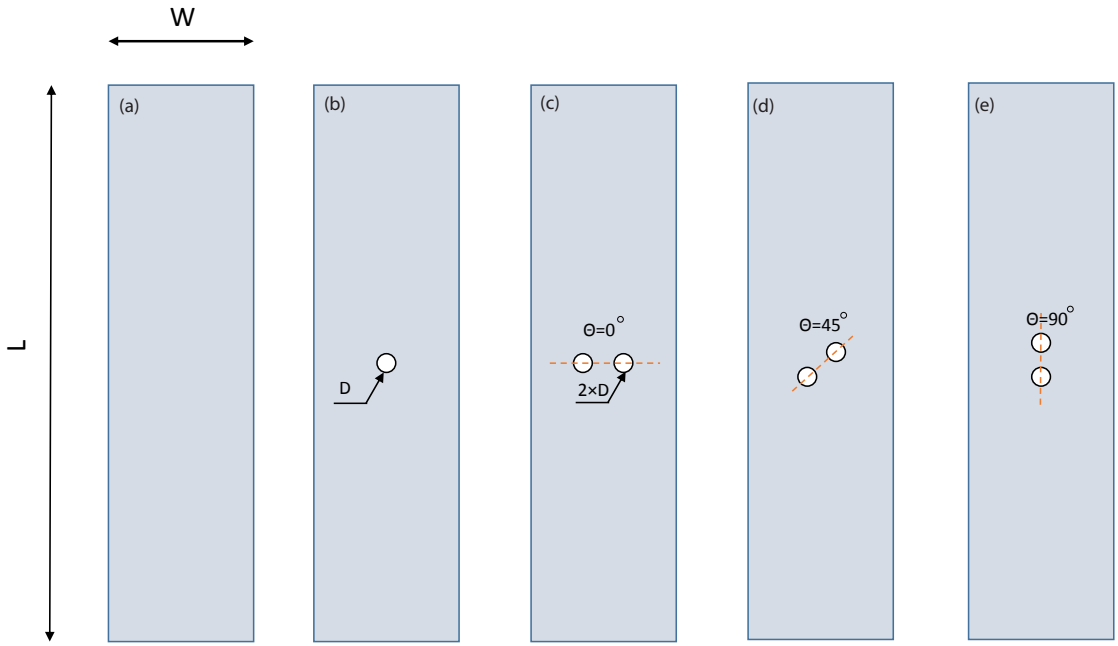

Figure 4.1 Schematic view of the geometry of fabricated samples (a) No-H, (b) 1H, (C) 2H0, (d) H45, (e) 2H90

4.1.1.2 Mechanical testing

An 8853 universal Instron testing machine with 250 kN load cell and speed of 2mm/min was utilized to test all the samples. ASTM D5766 and ASTM D3039 standards were used to carry out the tests for notched and un-notched composites, respectively. AN experimental test set up was represented in Figure. 4.2. IRT and DIC were implemented meanwhile to capture the damage evolution.

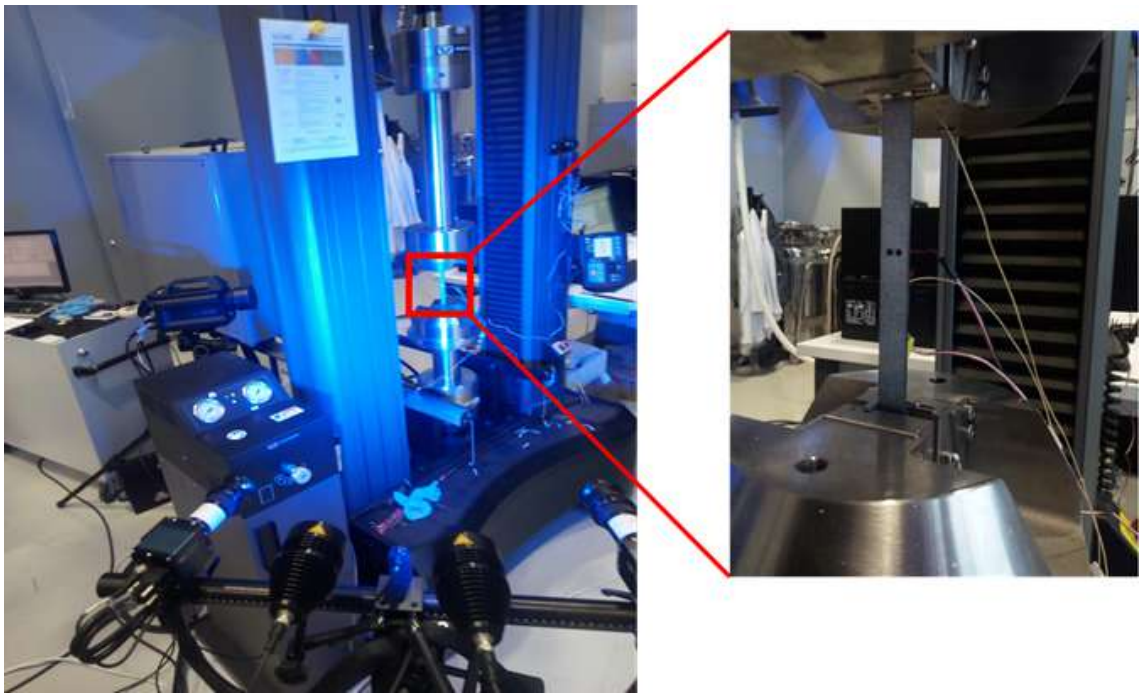

Figure 4.2 Experimental test set-up

Material attributes of the specimens were provided in Table. 4.2 wherein the E_{11}, E_{22} are longitudinal and transverse modulus, G_{12}, G_{23} are in-plane and out-of-plane shear modulus, and ν_{12} is Poisson ratio. This material represents the orthotropic material properties. All the values are based on upon the experimental workds and 5 samples were tested to ensure repeatability.

Table 4.2 Average mechanical properties of the manufactured specimens

E_{11} (MPa)	E_{22} (MPa)	G_{12} (MPa)	G_{23} (MPa)	ν_{12}
61835+/-949	53846+/-1183	3607+/-377	24475+/-2300	0.1

4.1.1.3 Digital image correlation

The local strains present throughout the tensile specimen are primarily monitored and measured using DIC. A 12 M sensor system from GOM (Braunschweig, Germany) was utilized. A white and black paint spray was employed to create speckle pattern nn the gauge length of the samples. A 150 mm by 200 mm calibration plate was utilized to calibrate the sensor. The calibration results showed 0.0018 mm scale variation and a calibration deviation of 0.03 pixels, which are between the manufacturer's upper and lower bound ranges. Before starting the tests, a pattern quality

analysis was carried out using the ARAMIS program. The analysis of the results was conducted employing the GOM inspect software.

4.1.1.4 Infrared Thermography

A non-destructive test method called IRT monitors infrared energy emitted from an object, converts it to temperature, and displays an image of temperature distribution. Passive IRT was employed to record the sample's temperature while it was being mechanically tested. During the test, the surface temperature distribution of the specimen was measured using an infrared camera (FLIR X6580sc) with 50 mm lens that was positioned approximately in 70 cm distance from the plain-weave sample. The operational temperature range of IRT camera had accuracy of 1 °C and ranges from -20 °C to 3000 °C. Images with a resolution of 640512 pixels were recorded at a sampling rate of 150 Hz. FLIR Research IR Max image analysis software was used for the analysis.

4.1.1.5 Fractography

As a complement to the IRT results, the macroscopic fracture morphology was examined. To identify the primary damage features of the fracture areas surrounding the hole(s), the fracture surfaces were also investigated by a stereo microscope. The fractography results are useful to explain the root of differences in the strength of different samples subjected to tensile loading condition.

4.1.2 Numerical study

Commercial software Abaqus/CAE was employed to carry out the numerical analysis. Ply-by-ply technique was employed in order to assign material orientation for 3D object with orthotropic mechanical attributes for each based on the layer sequences of the manufactured plane-weave composites including six plies. An eight-node linear brick, reduced integration, and hourglass control elements were implemented for all the simulations. Mesh size was decreased in the vicinity of the holes to obtain

accurate results specifically in the area of interest (region around the notches). Mesh convergence study was conducted to get the optimum element size (here 0.07mm around the holes). The mesh independency study for tensile stress was shown in Figure. 4.3.

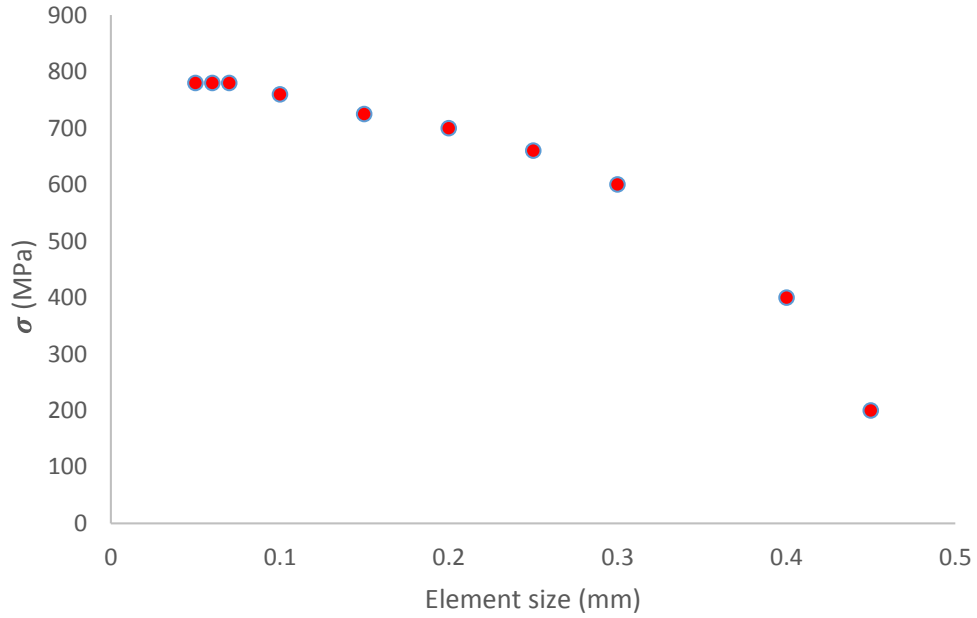

Figure 4.3 mesh independency check

The ABAQUS model has 395430 and 36096 number of nodes and elements for all the cases, respectively. Figure.4.4 shows the FEM model for one of the cases and the boundary conditions based on the experimental test. The tension load or displacement was applied to right edge while it was restricted in y-direction and the left side was restrained in all directions exactly based upon the tensile test.

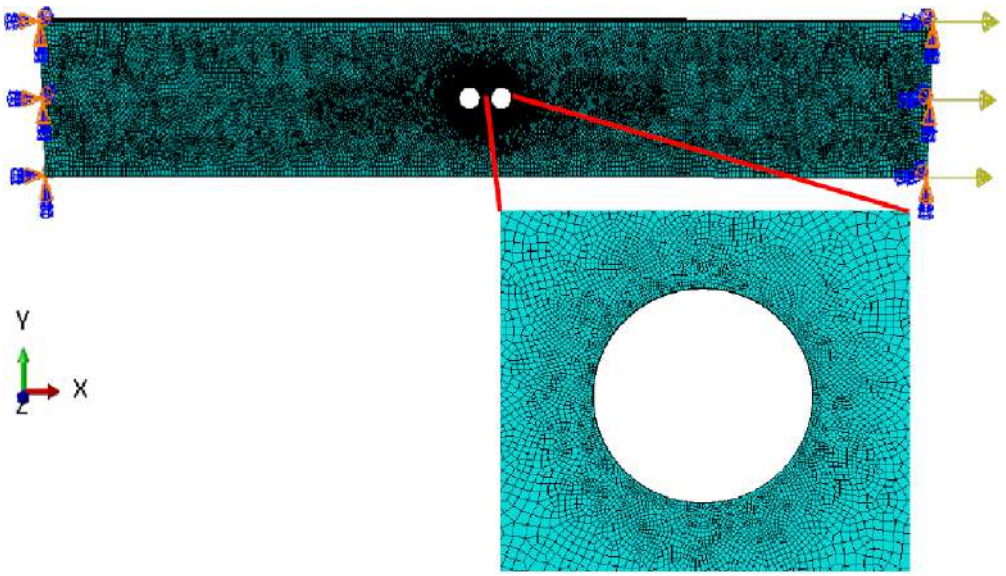

Figure 4.4 ABAQUS model with applied boundary conditions

The ABAQUS FEM model was verified with experimental results in terms of strain-stress performance. The comparison between experimental and numerical results for the samples without notch in terms of overall laminate stiffness was illustrated in Figure. 4.5. It is obvious that the numerical results are in an acceptable agreement with the tension test output. A few differences might be due to the voids, which were created during the manufacturing. Also, the experimental result was an average of five tensile tests.

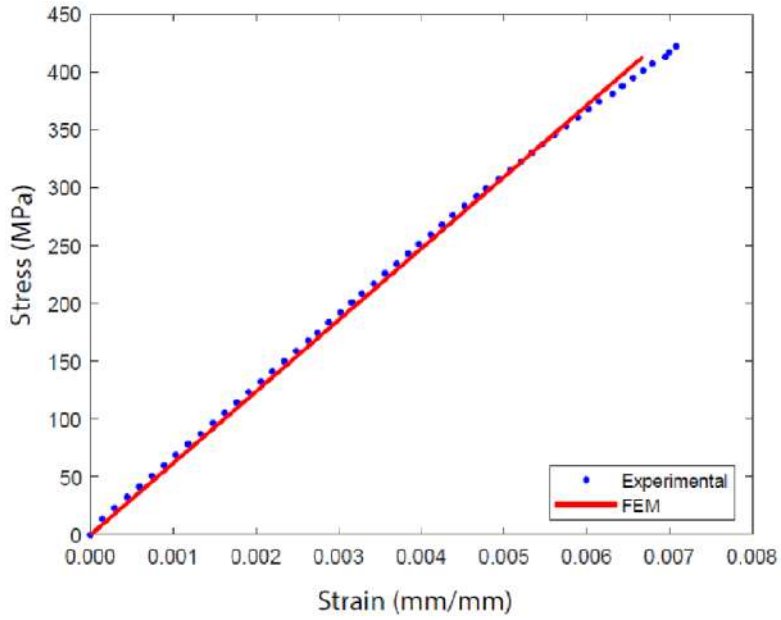

Figure 4.5 ABAQUS model with applied boundary conditions

4.1.3 Theoretical background

In order to predict the failure strength of the composite plate with hole, the Lekhnitskii formula was utilized for employing the PSC (Whitney & Nuismer, 1974):

$$\sigma^{\infty} = \frac{\sigma_0(0, r+d_0)}{\frac{1}{2}\left[2+(\frac{r}{r+d_0})^2+3(\frac{r}{r+d_0})^4-(K_t-3)[5(\frac{r}{r+d_0})^6-7(\frac{r}{r+d_0})^8]\right]} \tag{4.1}$$

in which K_t, the stress concentration factor is achieved via the numerical simulation, d_0 is the characteristic distance, and r is the radius of hole. It is assumed that the failure occurs while the stress in the loading direction at some distance away from the hole reaches the strength of un-notched sample.

Based on the principles of linear elastic fracture mechanics (Taylor, 2008), the PSC criterion requires that the critical region (damage zone), as in the case of a plate with a single notch, be constrained close to the hole. The critical region / processing zone is the place wherein the failure starts to propagate. In case of an open-hole sample subjected to tension, this region is along the horizontal line joining the periphery of the hole to the edge of the plate and high stress concentration was observed in this area. For the composite plates with two notches, critical region depends on the orientation and distance between the holes, and it could be either located within the holes or towards the outer area of one of the holes. It is worth noting that, when the discussion is about two interacting holes, the distance between center of the holes is 1.5 times the diameter (Özaslan et al., 2019). Thus, for the composite plates with two interacting notches, the location of the critical region depends solely on the hole configuration. Also, the characteristic distance in PSC should be in a location far away from the hole, outside the critical region, at a point where the stress shows linear behavior. Thus, it is possible to predict the failure strength of an open-hole plate applying PSC at the point of characteristic distance. Due to the complicated behavior of the composite plates with two interacting cut-outs, the direct application of PSC to predict the failure strength of plates with two holes is limited.

Based on the location of the critical region, Ozaslan et al. (Özaslan et al., 2019) proposed a methodology to predict the failure strength of orthotropic plate with two holes in different configurations based upon the location of the processing zone. Though the location of the critical region is dependent on both the orientation of the holes and their center-to-center distance; nevertheless, for composite plate with

interacting holes, when distance between the holes is constrained at 1.5 times of the hole diameter, the placement of the critical region depends only on the hole orientation. According to this methodology the PSC could be directly utilized if the processing zone lies at the outer periphery of the holes near to the edge. Otherwise, an extension of PSC method was proposed to predict the failure load. Extended PSC (EPSC) was therefore introduced with a new extended characteristic distance (d') and a corresponding extended strength (σ') into the Eq. 4.1. In the EPSC method the failure occurs when the stress far from the notch tip reaches the critical stress value. σ' and d' was calculated by integrating the plot of the average axial stress distribution around hole for an open-hole and one of plates with two holes to a single plot. The intersection point of these plots provides the values of σ' and d'. Therefore, in order to apply the PSC and EPSC methods for the prediction of the failure of notched plates the critical region, the SCFs, characteristic distances and critical strengths should be found.

4.2 Results and discussion

The results of the FEM simulations were compared with the experimental outcomes. Also, Fracture behavior of all specimens was discussed later by employing the stereo microscopy analysis to investigate the effect of hole orientation on the tensile stress of the specimen.

4.2.1 Mechanical test

Average tensile strength values for five samples of each hole configuration with their standard deviation are shown in Figure. 4.6. Obviously among all the sample, the highest strength was for laminate without notch. For the specimens with cut-out the 2H0 and 2H90 has the lowest and highest tensile strength (553 and 364 MPa), respectively. Interestingly, 2H90 has tensile strength more than the sample with a hole. The reasons will be discussed after explaining the fracture of each sample.

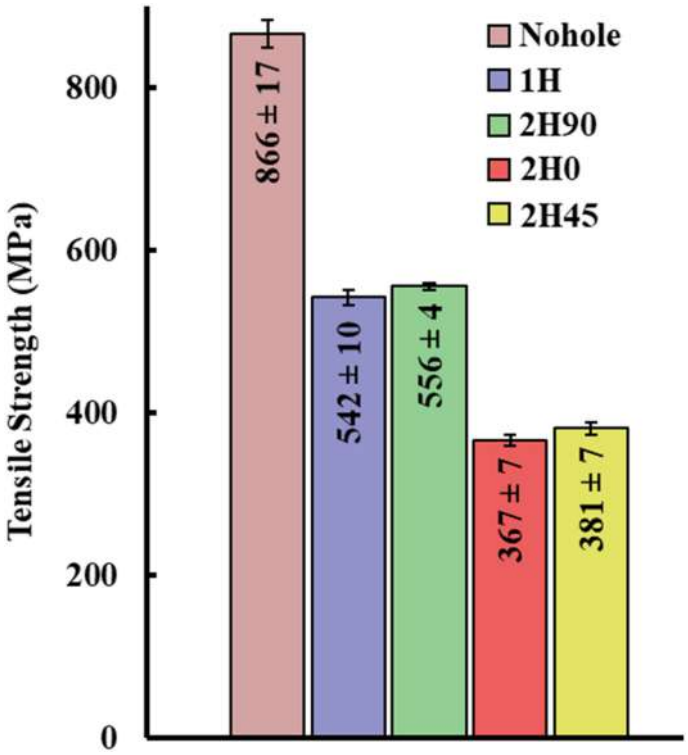

Figure 4.6 Average tensile stress for five specimens with different hole orientations

4.2.2 Numerical analysis

The numerical simulation was carried out to predict the failure strength of the samples. First, the SCF (ratio of the maximum average stress to the stress in the remote area) was calculated for each sample. The stress distribution (S11), at the failure load of each specimen, for the sample with; single hole (1H), two holes at 45° (2H45), two holes in longitudinal (2H90), and two holes in transverse (2H0), are shown in Figure. 4.7 (a), (b), (c) and (d), respectively.

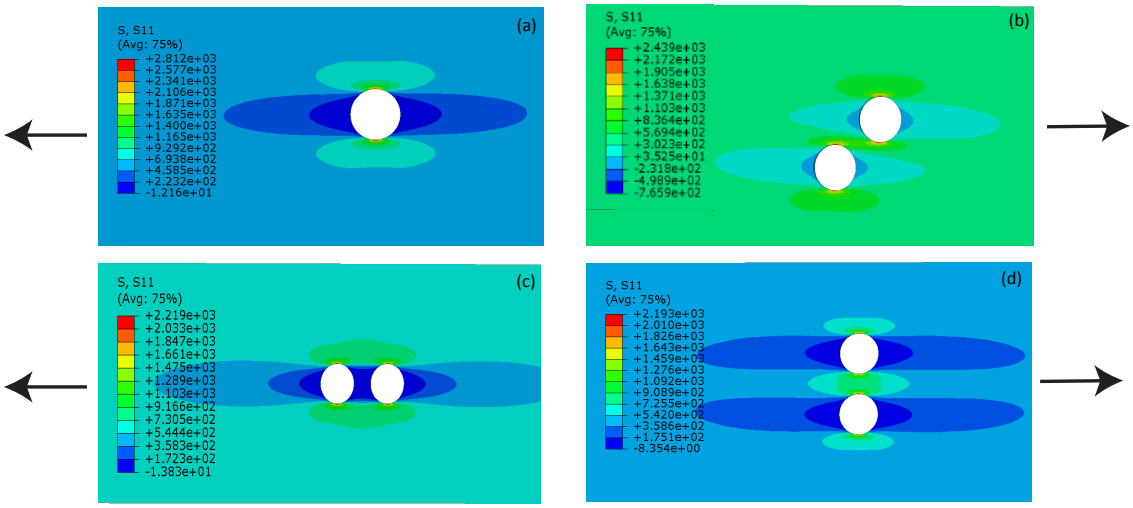

Figure 4.7 Average tensile strength for five specimens with different hole orientations (arrows show loading direction) (a) 1H, (b) 2H45, (c) 2H90, (d) 2H0

As represented in Table. 4.3, the SCF for the 2H0 sample is around 18% more than that of the sample with a single hole. Interestingly, SCF for 2H90 is the minimum among all the fabricated specimens while, the woven composite plate with 2H45 has the highest SCF. The SCF for this case is around 22% more than the single hole case. 2H90 has the least SCF with approximately 22% less than that of the 1H sample. It suggests that the design with longitudinal holes is best among all manufactured samples with respect to their load-bearing capacity.

Table 4.3 SCF for all the specimens

Sample	1H	2H45	2H90	2H0
SCF	5.3	6.48	4.16	6.03

Figure. 4.7 provides an indication about the location of the processing zone. It is indicated that the higher stress was concentrated, and the failure initiated and propagated from outer periphery of the hole(s) for 1H, 2H90, while it was in-between the holes for 2H45 and 2H0.

The longitudinal stress plotted on a horizontal path created from the outer periphery of hole to the edge of the sample in 1H laminate, and for 2H0 specimen, it was plotted along a path created between the two holes as shown in Figure.4.8. The characteristic distance $d_0 = 1.32$ mm is calculated using the stress distribution curve, achieved through the numerical simulation, around the hole for 1H sample as depicted in Figure. 4.8. The strength of 2H90 sample could be accordingly predicted by Eq. 4.1 by putting values of $r = 3$ mm, $d_0 = 1.32$ mm, and failure strength of unnotched sample and SCF (K_t)= 4.16 of 2H90.

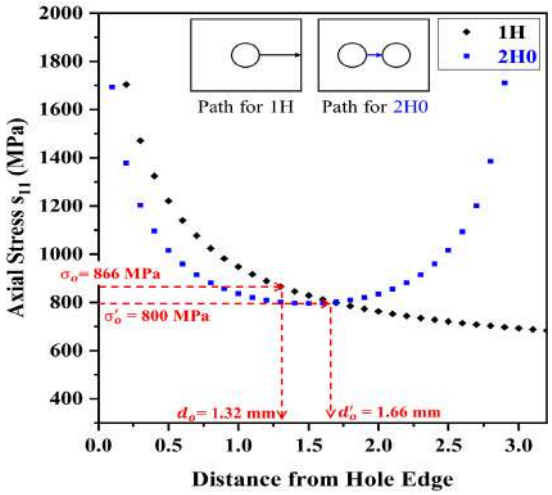

Figure 4.8 Averaged stress distributions of an open-hole and 2H0 along center-to-center (a) 1H (b) 2H45 (c) 2H90 (d)2H0

EPSC method could be applied to predict the failure strength of 2H45 since the critical region was located between two holes. The characteristic distance and critical strength for 2H0 as represented in Figure. 4.8, were $d'_0 = 1.66$ mm and $\sigma'_0 = 800$ MPa, respectively. The failure strength of 2H45 sample was then anticipated via Eq. 4.1, with $d'_0 = 1.66$ mm and $\sigma'_0 = 800$ and $k_t = 6.48$ for 2H45, as calculated by FEM.

4.2.3 Critical region determination by DIC

The processing zone for 2H0 and 2H45 was located between two holes, whereas it was located on the outer periphery of the holes for 2H90 sample as represented in Figure. 4.7. DIC technique was employed to identify the processing zone to validate the aforementioned proposition. Two points were considered on DIC surface within 1.3 mm in between the holes and at the periphery (towards the edge of the specimen) of one of the holes as represented in Figure. 4.9. The stress-strain plot given by the DIC at these points and from the total average axial strain achieved from DIC strain field were compared for each of the three specimens with two holes for each point.

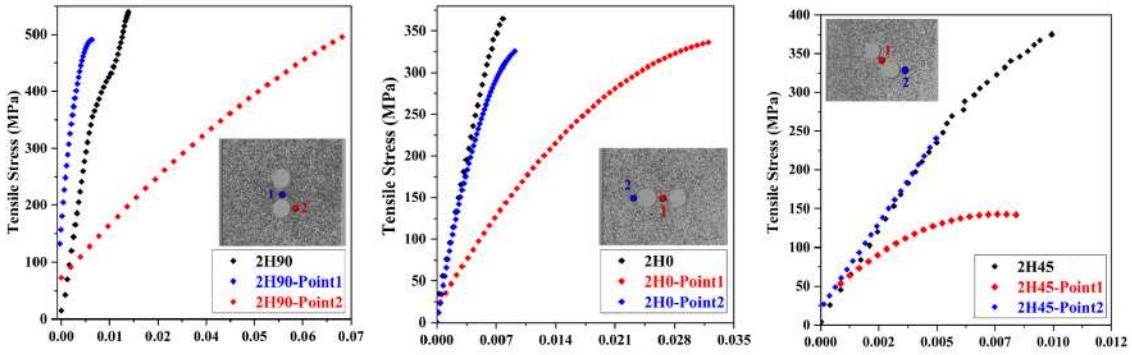

Figure 4.9 Processing zone determination utilizing DIC experimental data (total average axial strain is presented as black dotted line)

The stress vs. strain graph for point 1 in sample 2H90 was comparatively more linear than that of point 2. However, it was nearly linear at point 2 for specimens 2H0 and 2H45. Obviously, this non-linearity could be explained by an earlier stage of failure in the respective area, and it confirmed that the critical region (high scf) was lcoated at the outer edges of the holes in 2H90 specimen and between the holes in 2H0 and 2H45 samples.

In order to use PSC and EPSC criteria, identifying the characteristic distances as well as the location of critical region are both required as mentioned earlier. The characteristic distance was calculated through FEM, in literature. However, an experimental approach based on the DIC data was proposed here, further to FEM, to determine the characteristic distance. The DIC directly provides the strain map such that strain at any point of the region of interest could be captured anytime. The strain field around the hole for 1H specimen was achieved via creating a section line along the width, from the periphery of hole to the edge of the sample. This experimentally obtained strain field (axial ε_{11} and transverse ε_{22} strains) in the vicinity of the hole could be converted to axial stress distribution (σ_{11}) around the hole, assuming the overall mechanical properties to be orthotropic under the plane stress condition using the following equation Pandita, Nishiyabu & Verpoest (2003):

$$\sigma_{11} = \frac{E_{11}\varepsilon_{11}}{(1-\nu_{12}^2\frac{E_{22}}{E_{11}})} + \frac{\upsilon_{12}E_{22}\varepsilon_{22}}{(1-\nu_{12}^2\frac{E_{22}}{E_{11}})} \tag{4.2}$$

The estimated axial stress distribution around the hole for 1H and 2H0 specimens as obtained from Eq. 4.2 were shown in Figure. 4.10.

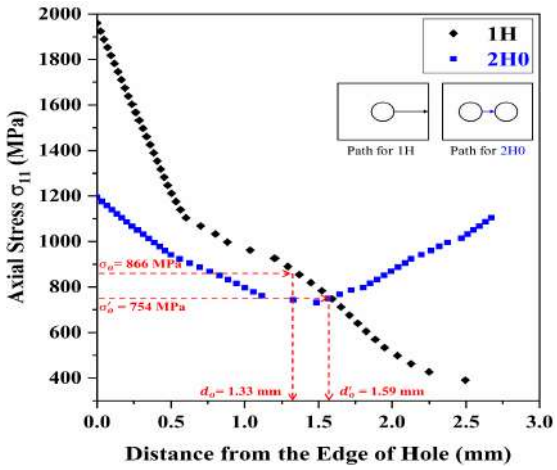

Figure 4.10 Averaged stress distributions and characteristic distance of 1H and 2H0 through DIC

It should be noted that the axial stress is based on the strain obtained by DIC, and a possible non-uniformity in the strain values could affect behavior of the curves. However, it did not affect the characteristic distance values d_0 and d_0', which were obtained through PSC and EPSC techniques as shown in Figure. 4.10. The values of these distances were in good agreement with those given by numerical simulation.

Predicted failure strength given through PSC and EPSC methods for 2H90 and 2H45 specimens is provided in Table. 4.4. For specimen 2H90 sample (critical region on outer periphery of holes) the FEM and DIC results were comparable with the value obtained by experimental test. The comparison of the FEM/DIC and experimental results indicates that the EPSC technique for 2H45 (critical region in between holes) is not applicable. The reason might be due to the difference of stacking arrangement and/or material system. Thus, the applicability of this technique for some composite structures is under question.

Table 4.4 Failure strength Prediction by PSC and EPSC methods (value is in MPa and error is in % unit)

Prediction for 2H90 (PSC method)					Prediction for 2H45 (EPSC method)				
Exp.	DIC		FEM		Exp.	DIC		FEM	
	value	error	value	error		value	error	value	error
556	584	5	583	4.5	381	620	63	663	74

4.2.4 Progressive failure analysis by IRT

For 1H and 2H90 samples, it was expected that the failure started and propagated in the outer periphery of the hole(s), towards the edge of the specimen, as the processing zone was found to be in the same location. IRT thermograms of those specimens were represented in Figure. 4.11 and 4.12, respectively.

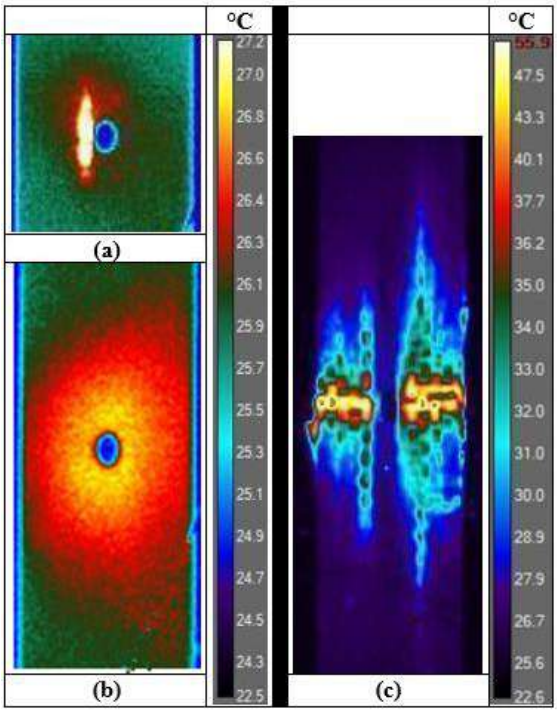

Figure 4.11 IRT thermograms for sample 1H showing (a) initial delamination (462 MPa), (b) temperature distribution around the hole (523 MPa) and (c) final failure (528 MPa)

Thereafter, numerous such events were seen, specifically for 2H90, on both sides of the holes. It is very important to note that the length of the axial split is shorter for 1h specimen as compared to the 2H90 sample. This could be because of the interaction of two holes. Axial splits typically provide a stress relieving or crack-blunting effects. Thus, initiation of catastrophic delamination by stress-redistribution was delayed. Although, the longitudinal splits were captured in 1H sample but the crack blunting influence was not as noticeable as 2H90 sample. It could be attributed to two factors: (1) the lower initial SCF for 1H than 2H90 sample and (2) the longer axial splits size in 2H90 than that of 1H. As the load increases, the extent of damage enhances and the temperature distribution around the hole(s) almost before the maximum stress level revealed a beneficial effect of the interaction between the two holes.

It was observed that the distribution of temperature was more spread in the transverse direction from the notch periphery to the edge of the 1H0 sample (Figure. 4.11). It confirmed a weaker crack-blunting effect. However, a remarkable behavior of the interaction of two holes was observed in 2H90 specimen, wherein the temperature distribution in the vicinity of the notches kept confined to a smaller portion of the width of the sample (Figure. 4.12). Also, because of the presence of two longitudinal holes, the temperature distribution was advanced more along the longitudinal direction comparing to the 1H sample. This observation was agreed with the earlier attributed crack-blunting effect which ascertained the stress concentration was effectively redistributed to reduce the transversal matrix cracking.

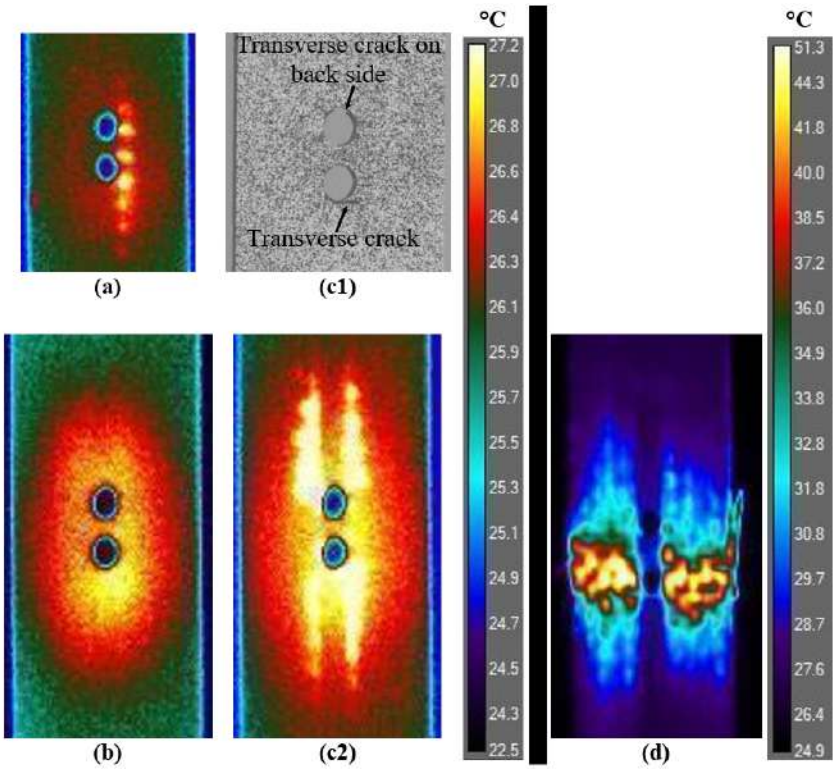

Figure 4.12 IRT for 2H90 sample (a) initial delamination (528 MPa), (b), (c2) temperature distribution around the hole before and at maximum load (540 MPa), respectively, (d) final failure (529 MPa) and (c1) complimentary DIC image at max load

The IRT thermogram for 2H90 sample at maximum stress, Figure. 4.13 (c2) showed a triangular temperature distribution provided an evidence of delamination along the length of longitudinal splits in the vicinity of two holes, which was already affirmed by the complementary DIC photo, Figure. 4.13 (c1). Moreover, 2H90 sample did not fail sharply at the highest stress level, 540 MPa, but pursued to transfer the load till the last catastrophic failure at a lower stress of 529 MPa, Figure. 4.13 (d). It could be attributed to lessening the effective cross-section of the specimen and the

final failure occurred by delamination and fiber-cracking. On the contrary, the 1H sample failed catastrophically at the highest stress of 528 MPa, as shown in Figure. 4.11 (c). The damage in 1H sample evolved with consecutive ply splits near the hole and any other feature, apart from an imbalanced stress distribution in the vicinity of the hole, was not observed. The asymmetrical stress distribution finally resulted in a delamination dominated failure on one side of the sample as represented in Figure. 4.11 (c). These observations confirmed further the effectiveness of the stress concentration blunting effect in 2H90 sample.

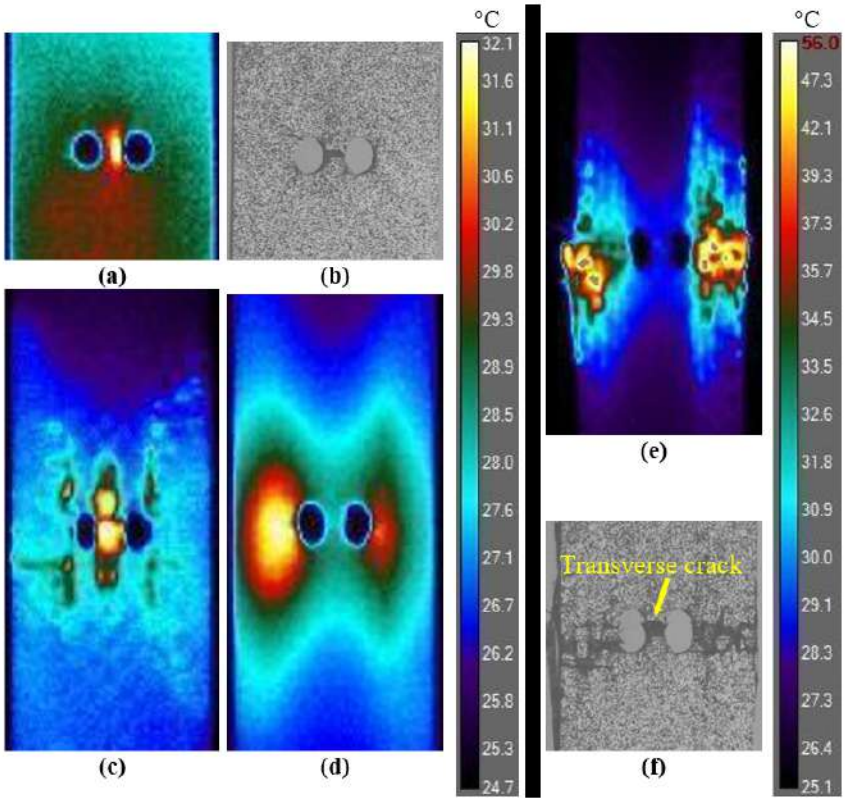

Figure 4.13 IRT for sample 2H0 (a) first delamination (309 MPa, 57.5 seconds), (b) complimentary DIC image after first failure, temperature distribution (c) at highest load (368 MPa, 76.7 seconds), (d) before final failure, (e) at final failure (339 MPa, 89.5 seconds) and (f) complimentary DIC image after failure

For the 2H0 and 2H45 specimens for which the processing zone was identified between the holes and the SCF values were 6.03 and 6.48, respectively, one might doubt that the sample with the lower SCF value should provide a higher final strength and vice versa. However, a contradiction was observed, i.e. the average maximum strength of 2H45 sample was 381 MPa while 2H0 specimen had lower strength of 367 MPa. It is crucial to study the failure dynamics in these laminates to explain this anomaly. The IRT was employed and interesting results were unveiled. Firstly, the initial failure for 2H0 and 2H45 occurred at 309 MPa (at 57.5 seconds) and 235 MPa

(at 41.8 seconds) as shown in Figure. 4.13 (a) and Figure. 4.14 (a), matched well with the SCF values. The complementary images Figure. 4.13 (b) and Figure. 4.14 (b), given by DIC, also represent the initial damage of the outer surface ply. These DIC images also showed that the initial failure is along the line joining the centers of the holes, in-accordance with the stress distribution around the holes obtained from FEM. After this initial failure, the specimen 2H0 continues to carry the load in a traditional manner such that the critical region remains in between the two holes. Eventually, as seen in Figure. 4.13 (c), the specimen reaches its maximum strength of 368 MPa (76.7 seconds) with the damage, as expected, being mostly accumulated within the central area of the holes.

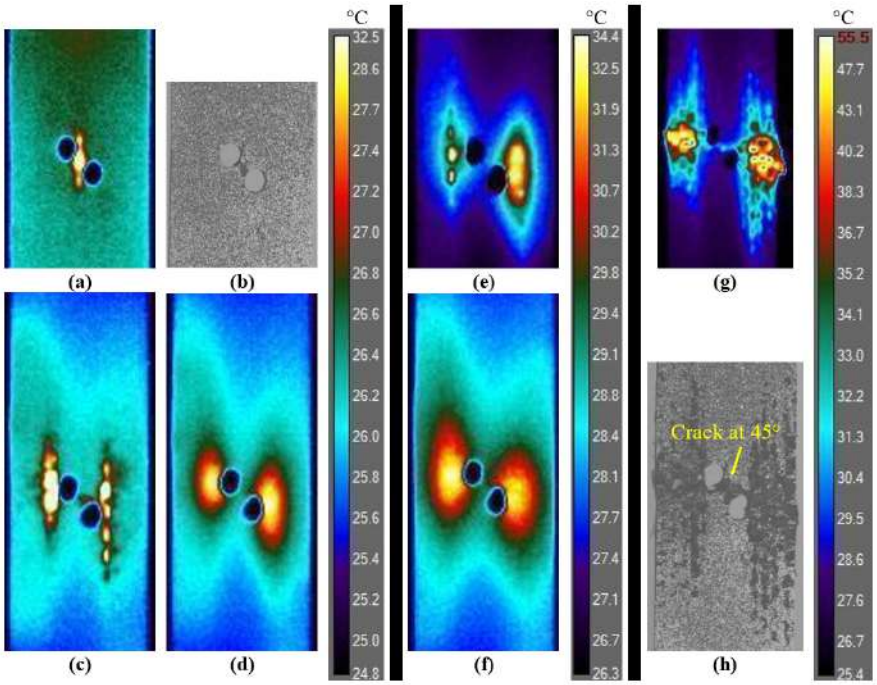

Figure 4.14 IRT thermograms for sample 2H45 showing (a) initial delamination (235 MPa, 41.8 seconds), (b) complimentary DIC image after first failure, (c) second delamination event, temperature distribution (d) before maximum load, (e) at maximum load (376 MPa, 89.7 seconds), (f) before final failure, (g) at final failure (353 MPa, 102.7 seconds) and (h) complimentary DIC image after failure

Entirely unconventional failure progression was observed after initial failure for 2H45 sample. After the first delamination between the holes, the progression of failure was not confined to the central portion between them. But instead, the failure progression continues at the outer edge of the two holes as depicted from the delamination events shown in Figure. 4.14 (c). The reason for this transformation of the critical area from the central region between the notches to an outer periphery, might be the influence of the holes configuration. It could be understood through carefully observing the initial failure as shown in Figure. 4.13 (b) and Figure. 4.14 (b). It is

obvious that the initial failure in 2H45 the propagated at an angle of 45°, whereas for the 2H0 sample it was perpendicular to the loading direction. Although because of the higher values of SCF for 2H45, the failure started sooner but the accumulation of failure along the 45° angle was difficult in comparison to that of a transverse failure. Thus, the critical region shifted, from the central area between the holes to the outer periphery, to make the accumulation of damage easy. The distribution of stress on the outer edges supported the transversal damage as depicted in Figure. 4.14 (d). The specimen 2H45 then continued to bear the load till it reached to maximum strength of 376 MPa (89.7 seconds) while accumulating the damage on the outer edges of the cut-outs Figure.4.14 (e).

Both 2H45 and 2H0, remained intact and carried the load further after reaching the maximum strength. The distribution of stress was concentrated on the outer edges of the holes as indicated by the temperature distribution in IRT thermograms, Figure. 4.13 (d) and Figure. 4.14 (f). At the final failure point both the specimens failed abruptly accompanying interfacial and transversal matrix failure and fiber breakage as depicted in IRT thermograms and complementary DIC images in Figure. 4.13 (e, f) and Figure. 4.14 (g, h). Here, wide axial delamination events were seen in the 2H45 sample comparing with the specimen 2H0. It is attributed to the difference in the holes configuration and the temperature distribution, equivalently stress distribution around the notches almost before the last failure.

4.2.5 Fracture surface analysis

Fracture morphology of the all the fabricated samples including 1H, 2H90, 2H0 and 2H45 is illustrated in Figure. 4.15 (a), (b), (c), and (d), respectively. All the samples represented a specific level of delamination morphology as well as the fiber failure and transverse matrix cracking. The fracture surfaces of 1H and 2H90 specimens with processing zones at the outer periphery of the hole(s), indicated that in 1H sample transversal matrix cracks dominated the failure. However, in 2H90 large-region delamination fracture was captured. This observation is consistent with IRT results where large-area delamination at edges of the holes in 2H90 while transversal fracture in 1H are apparent, Figure. 4.12(c2) and Figure. 4.11 (c), respectively. As mentioned earlier, the strength of 2H90 specimen was higher than 1H sample for all 5 samples reaped tests. This could possibly be due the more active delamination in a fiber-dominated failure led to higher notched strength. A slanted through the thickness delamination growth extending across two holes was revealed in fracture

surface of 2H90 as shown in Figure. 4.15 (b1). This was only possible due to the interaction between two holes. On the contrary, fewer delamination fracture events could be observed for 1H, Figure. 4.15 (a1), which was matched with IRT results.

For 2H0 and 2H45 samples with processing zone between two holes, provides interesting reasons for the higher maximum strength of 2H45 as compared to that of 2H0 was complemented. On large scale, the fracture of 2H0 was mostly due to the transverse matrix cracking, Figure. 4.15 (c). However, the fracture surface of 2H45, Figure. 4.15 (d), demonstrated features such as rotation of weft fibers and more amount of delamination fracture. Furthermore, the change in the orientation of fibers towards the loading direction also suggest a higher load carrying capability of laminates with 2H45 with respect to the 2H0. The magnified photos between the two holes of samples 2H0 and 2H45 are shown in Figure 4.15 (c1) and (d1), respectively. This fracture surface morphology of the processing zone showed a delayed damage propagation in 2H45 comparing with the 2H0 specimen. The fracture at critical region was controlled by transverse matrix crack in 2H0 specimen, while in 2H45 the damage propagated across the holes at 45° angle, which also verifies the IRT results. Furthermore, the rotation of weft fiber tow was visible in the central region of 2H45 sample. These observations justified the higher failure strength of 2H45, though the SCF of 2H0 was lower than 2H0 specimen.

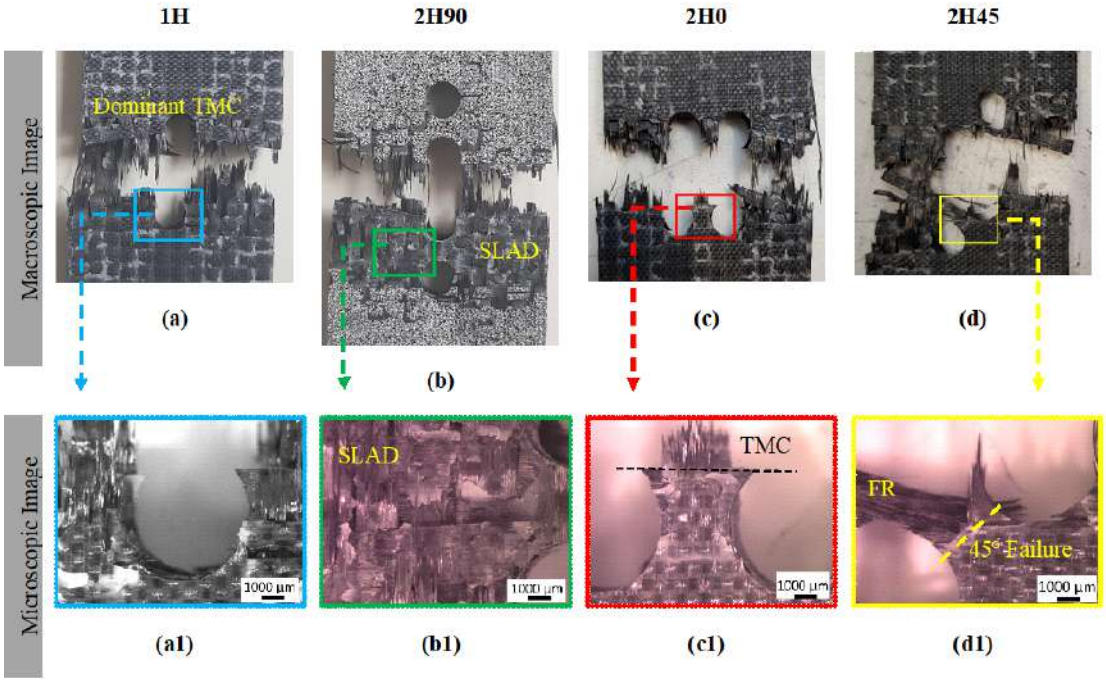

Figure 4.15 Fracture surface morphology (Note: SLAD: Slanted Large Area Delamination, TMC – Transverse Matrix Crack, FR – Fiber Rotation)

5. Stacked ML model

In this chapter, the developed Stacked ML model saw thoroughly discussed and the results and discussion provided as a comparative study.

5.1 Materials and methods

FEM model and data generation following with the data preprocessing and model development were provided in this section.

5.1.1 Finite Element Model and data generation

The FEM technique was utlized to generate the data-rich framework. Following the descriptions of each ML technique, pre-processing algorithms and model metrics were explain in detail in this section. The Python code was used for the automation of parametric studies in ABAQUS. Plate width, length, thickness, hole configuration, hole radius, lay-ups, and forces were among the parameters that were altered in order to obtain the data. The statistical data analysis of the data-rich framework is represented in Table. 5.1. The data-rich framework was produced using a total of 8960 FE simulations. In order to investigate the maximum stress that concentrated close to the holes, a range of force took into account failure point, was provided. Different layer orientations, such as Cross-ply, symmetric, unidirectional, etc. were used to further investigate the effect of layup on the strength of the material.

Table 5.1 Dataset statistical description

	Input								Output
	W[a] (mm)	L[b] (mm)	T[c] (mm)	HA[d] (°)	HR[e] (mm)	CR[f] (mm)	F[g] (N)	SS[h] (°)	Max.Stress (MPa)
Max	36	250	3.636	90	3	4.5	40000	-	9087
Min	24	100	1.818	0	1.5	2.25	10000	-	308
Std	4.47	175	0.90	45.58	1.75	1.12	11309	-	1431
Mean	30	55.90	2.72	30.09	2.25	3.37	25112	-	2252

[a] Width
[b] Length
[c] Thickness
[d] Hole angle
[e] Hole radius
[f] Circle radius
[g] Force
[h] Stacking sequence ([0, 90, 45, -45, 90, 0], [0, 0, 0, 0, 0, 0], [0, 45, 0, -45, 90, 0], [0, 90, 0, 0, 90, 0], [45, 45, 0, 0, 45, 45])

5.1.2 Pre-processing methods

Data preprocessing is the modification or removal of data before use in order to ensure or improve the quality of the dataset. This is a significant step in developing data mining and ML models. Dataset normalization is a common requirement for many ML algorithms. Two steps were performed to preprocess the dataset structure.

5.1.2.1 Robust scaler

The median is taken out by the robust scalers to unit variance and scales the data according to the quantile range, which was by default IQR (Interquartile Range). The IQR is in the range of the first quartile (25th quantile) and the third quartile (75th quantile). Median and IQR range stored to be employed on later data through the transform method in order to achieve more accurate results. However, outliers almost always affect the sample mean/variance in a negative way. Thus, IQR and median often give better results (Ahsan, Mahmud, Saha, Gupta & Siddique, 2021).

5.1.2.2 MinMax scaler

MinMaxScaler subtracts the minimum value for each value in a feature, and then divides by the range, which is the difference between the original and minimum values (Ahsan et al., 2021). The range for the feature returned by MinMaxScaler is between 0 to 1.

5.1.3 Feature selection methods

In case all of the available data used for the training of the dataset, the model accuracy is reduced and the possibility of overfitting problem is enhanced. Thus, unnecessary features of the dataset should be eliminated to train ML algorithms efficiently. Feature selection (FS) methods were utilized to omit the redundant dimensions of the dataset meanwhile keeping the most relevant features. Also, the complexity of the models are generally reduced by implementing FS methods. Moreover, it enables the ML to train faster. The relevancy is related to the contribution of the feature to enhance the ML model accuracy. Different FS methods were implemented which are divided into three main types: filter, wrapper, and embedded.

In the wrapper method, a subset of features is used to train an algorithm while in the filter technique, features are selected based upon their scores in different statistical tests for their correlation with the target value. In embedded features, both wrapper and filter algorithms are integrated. Both the Filter & wrapper approach were employed here.

Pearson's correlation coefficient known as pairwise correlation is the covariance of the two variables divided by the product of their standard deviations Sedgwick (2012). The form of the definition involves a product moment, which is the mean of the product of the mean-adjusted random variables; Hence, the modifier product-moment in the name. Pearson correlation is defined by:

$$r = \frac{\sum (x_i - \bar{x})(y_i - \bar{y})}{\sqrt{\sum (x_i - \bar{x})^2 \sum (y_i - \bar{y})^2}}, \tag{5.1}$$

where the x_i, $\bar{x}$, y_i, $\bar{y}$, and r are values of the x-variable in a sample, average of the values of x-variable, values of the y-variable in a sample, average of the values of

y-variable, and the correlation coefficient, respectively.

5.1.4 Machine Learning methods

5.1.4.1 Ridge Cross-Validation (RidgeCV)

Ridge regression is considered a linear regression accompanied by regularization which is defined by:

$$I(\beta) = MSE(\beta) + \lambda \sum_{i=1}^{n} \beta_i^2 \tag{5.2}$$

The value of the model regularization is controlled through the hyperparameter λ, which is the intensity of regularization. L2-norm is a square regularization which is employed in Ridge regression. The term β is a model feature and n is the number of parameters/coefficients in the model. $\lambda \sum_{i=1}^{n} \beta_i^2$ is incorporated into the cost function. This parameter is not applied for performance assessment in a test set or predicting an actual sample. The larger the value of λ, the higher possibility of zero weights. Generally, RidgeCV is defined as a Ridge regression with a built-in cross-validation estimator. The optimal hyperparameters are chosen automatically via an estimator with built-in cross-validation ability (Melkumova & Shatskikh, 2017).

5.1.4.2 Least absolute shrinkage and selection operator (Lasso)

The Linear regression which uses shrinkage is called Lasso regression. Ridge regression is almost similar to the Lasso algorithm. However, the Lasso algorithm utilizes L1-norm (absolute regularization). The lasso algorithm creates sparse models containing a few parameters. Lasso regression could conveniently handle high multicollinear models. Furthermore, automating specific parts of model selection, such as parameter elimination and/or variable selection could be conducted by the Lasso model.

Lasso, as quadratic programming problems is implemented to minimize:

$$\sum_{i=1}^{n}(y_i - \sum_{j} x_{ij}\beta_j)^2 + \lambda \sum_{j=1}^{p} \mid \beta_j \mid . \tag{5.3}$$

The left side indicates the loss function. x_{ij} is an actual training data for i'th observation and y_i is an actual target value. The term β is the model feature and n is the number of parameters or coefficients in the model. The amount of shrinkage (dataset values are shrunk towards a central point like the mean) are represented by the tuning parameter λ. Identifying the parameter that Minimizes the sum of Mean Squared Error (MSE) and penalty terms is the final purpose of Lasso. No parameters are taken out when λ=0. Therefore, the prediction found by the linear regression technique is equal to the prediction conducted through assigning the tuning parameter to zero.

More coefficients are set to zero while increasing the tuning parameter. Theoretically, when $\lambda = \infty$, all coefficients are removed. It is worth mentioning that the bias and variance are increased as the value of λ enhances. In case of the low coefficient of the characteristic, the effect of property on the model increases the bias to prevent overfitting.

5.1.4.3 Polynomial Features

Addition of complexity to an algorithm through considering nonlinear features of the input data could be generally helpful in solving problems. Polynomial features provide a feature matrix containing all polynomial combinations of the features. Two possibilities are proposed based upon polynomials: piece-wise polynomials and pure polynomials. A pure polynomial model is an algorithm with only a single polynomial, while a piece-wise polynomial could include non-polynomial terms. The pure polynomial takes a single polynomial term unlike the Lasso and Ridge which makes a linear relationship between input and output.

5.1.4.4 Decision Tree (DT)

A DT predicts through imposing tests on input datasets. This technique is extensively employed for both regression and classification problems since it is not complicated and explainable (Kim & Hong, 2017). A CART (classification and regression tree) algorithm has been widely used to construct DT model. Training is conducted recursively similar to an inverted tree structure with a root node, internal nodes and leaf nodes. Splitting rules are applied to create a split into subtrees, at each node. In this method, the goal is to minimize total error sum of squares given by:

$$\sum_{i \in C_1} (y_i - y_1^*)^2 + \sum_{i \in C_2} (y_i - y_2^*)^2 \tag{5.4}$$

in which, y_1^* and y_2^* are predicted values, C_1 and C_2 are two split subtrees, and y_i is true value. Decision split and depth, as hyperparameters, are being decided .

5.1.4.5 Gradient Boosting Regression (GBR)

GBR is a combination of gradient descent and decision trees. Each successive shallow tree in the ensemble learns from the previous one. (Bagherzadeh, Mehrani, Basirifard & Roostaei, 2021). Initiating with a weak model, gradient boosting consecutively improves the performance via building new trees which adjust the residuals from the previous tree through least squares. Thus, each new tree resolves the poor regression from the previous one repeatedly. The residuals are typically assessed through the loss function, e.g. MAE, which could be minimized via gradient descent.

5.1.4.6 K-Nearest Neighbors Regressor (KNN)

KNN algorithm is employed for classification and regression and problems. 'Feature similarity' is generally utilized in this technique to predict the values of each new data points. A value is assigned to a new point based on how nearly it resembles the points in the training subset. Observations near the space of data attributes are near to each other in the space of outputs. In order to predict the output

values, a predefined function of the nearest neighbor's response value is utilized Feng, González & Casero (2021). Conducting KNN requires the following steps: (i) calculation of the distance between the new data point and each training point. (ii) The closest k data points are chosen. The value of k is non-parametric and generally is equal to $\sqrt{N}/2$, and N represents the number of samples in the training set. (iii) Final prediction for the new point is the mean of these data points. It should be highlighted that this algorithm is not highly affected by the possible noise in learning data. Thus, KNN is helpful for large amounts of learning data.

5.1.4.7 Stochastic Gradient Descent (SGD)

Stochastic gradient descent (SGD) is an iterative technique which is utilized to optimize a function with an acceptable smoothness characteristics initiates from a random point on a function and goes down on slope until reaching the lowest point of that function. It could be employed to fit linear regressors under convex loss functions SVR. Training a model is a purpose of this algorithm and typically it is an optimization method (Sun & Li, 2022).

5.1.4.8 Artificial Neural Network (ANN)

The performance of the complex systems could be assessed by ANN. ANNs are a type of data-driven model that could resolve highly non-linear problems. Pre-existing patterns (historical dataset on the input and output variables) of the large-scale problems are utilized to detect the correlation between input and output variables. This relation is encoded via hidden layers, between the input and output patterns (Guessasma, Montavon & Coddet, 2004). The efficiency of artificial networks is influenced by the process of activities transmission through the neural network, type of neural connections, and computations performed by the neurons. Those layers are interconnected by weighted values which indicate the significance of the inputs while predicting desired outputs. There are interconnected nodes or neurons in each layer.

This neural network with modified weight magnitudes was used to compute the approximated mathematical nonlinear relationship between the input (I_{mi}) and output (O_{ni}) layers. The inputs were multiplied by these weights (w_{ij}) and the results for

each layer of neurons combined with the biases (B_i), wherein the final outcome was multiplied with an activation function as following:

$$O_{mi} = g(\sum_{i=1}^{n} w_{ij} I_{mi} + B_i). \tag{5.5}$$

Most popular activation functions were shown in Table. 5.2. Sigmoid activation function was adopted for the present study.

Table 5.2 Different activation functions employed in ANN

Activation function	Formulation
SELU	$\sigma(x) = \lambda \begin{cases} x & \text{if} \quad x > 0 \\ \alpha e^x - \alpha & \text{if} \quad x \leq 0 \end{cases}$
Tanh	2Sigmoind($2x$)-1
ReLU	$\sigma(x) = \lambda \begin{cases} x & \text{if} \quad x > 0 \\ 0 & \text{if} \quad x \leq 0 \end{cases}$
Softplus	$\sigma(x) = ln(1 + e^x)$
Sigmoid	$\frac{1}{1+e^{-x}}$

A schematic view of the ML models used for prediction is shown in Figure 5.1.

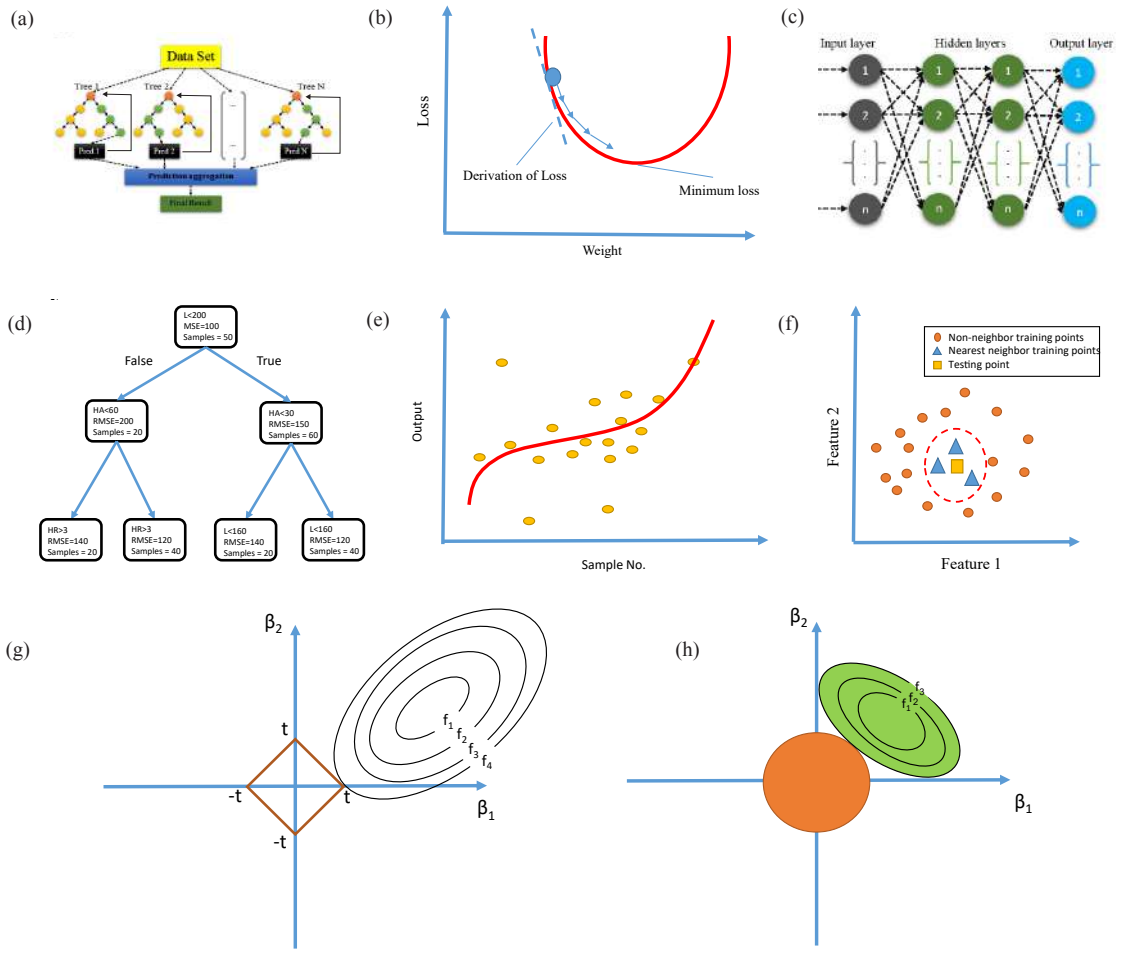

Figure 5.1 Schematic view of the ML models (a) ANN, (b) SGD, (c) GBR, (d) ET, (e) PolyFeatures, (f) KNN, (g) Lasso, (h) Ridge

5.1.4.9 Stacked ML

Various ML models are integrated to select the suitable ML model well-suited to the input data since one ML model could not provide the best solution (Bagherzadeh & Shafighfard, 2022b; Shafighfard, Bagherzadeh, Rizi & Yoo, 2022).

5.1.4.10 Grid search

The grid search is a thorough search method that defines uniform grids in the space of the searched parameters. The global minimum is then determined by assessing

each node in the grid. Thereafter, the grid search identifies the global minimum of all the nodes in the parameter grid (Abbaszadeh, Soltani-Mohammadi & Ahmed, 2022). The model performance could be enhanced through detecting the optimum model parameters, which is the final aim of the grid search technique.

Research in Automated ML is noticeably diverse and various types including but not limited to AutoGluon, H2O AutoML, and Tree-based Pipeline Optimization Tools (TPOT) have been developed. An evolutionary algorithm TPOT was selected wherein the genetic algorithms programming was employed to optimize the ML pipelines. Different number of seeds were used in the TPOT code to ensure that the accuracy of the developed model was not influenced by the selection of the training dataset.

5.1.5 Model Metrics

Well-known model metrics have been calculated to measure the accuracy of the ML algorithms. The accuracy of model predictions on the train and test dataset could be measured through the model metrics. RMSE, MAE, and coefficient of determination (R^2) were applied.

$$R^2 = 1 - \frac{\sum(a_i - p_i)^2}{\sum(a_i - \mu_a)^2} \tag{5.6}$$

$$\text{RMSE} = \sqrt{\frac{1}{n}\sum_{i=1}^{n}(a_i - p_i)^2} \tag{5.7}$$

$$\text{MAE} = \frac{1}{n}\sum_{i=1}^{n} \mid a_i - p_i \mid \tag{5.8}$$

in which, n is the total number of records and $i = 1, 2, ..n$ is the number of observations. Also, p_i, a_i and μ_a are real, predicted, and mean values, respectively.

5.2 Results and Discussion

The results of data-pre-processing, feature selection as well as the comparative study were explained in this section.

5.2.1 Data pre-processing

The pairwise correlation (Figure 5.2) proposed that the circle radius (distance between holes) was highly related to the hole radius. Therefore, this feature was taken out in pre-processing. The force and holes configuration had the highest positive correlation with the maximum tensile stress (target variable) in the vicinity of the holes according to Figure 5.2. As the hole orientation deviated from the longitudinal (along the loading direction) alignment, the maximum stress in the proximity of the holes enhanced. Moreover, the stress concentration shifted from the outer edge of the holes to the space between the holes. Thus, the failure happened sooner when the two holes were oriented transverse to the loading direction than in the longitudinal configurations. An inverse correlation of the depth and width of the specimens associated with the output variable. Hence, the larger width and depth, the lower stress concentration near the holes. This resulted in the belated failure of the sample. Considering the composite stacking sequences, the first and the last layers had the highest correlation with the maximum stress of the sample. It should be mentioned that the overall influence of five different stacking sequences was evaluated via the developed ML models. Thus, care should be given while designing these layers in samples with different hole orientations and sample geometries. It should be also noted that since the correlation between features was in the range of -0.5 and 0.7, capturing the patterns between data features was a complex task and they did not have a linear relation with the target variable. Therefore, ML could be an efficient tool for the prediction of the output value.

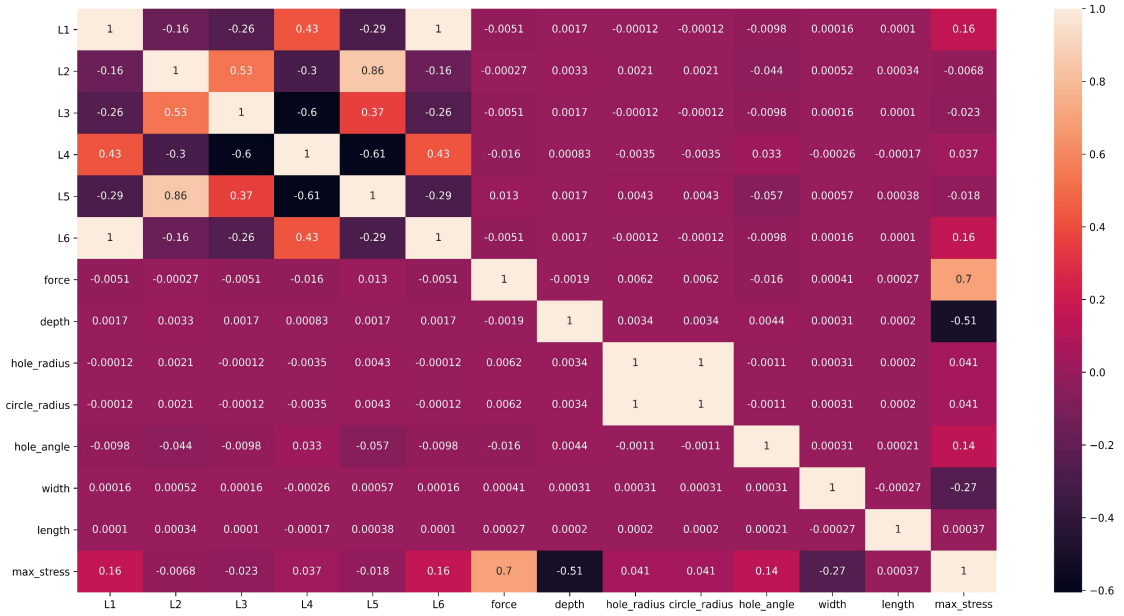

Figure 5.2 Pearson correlation heat map

The RF feature score is represented in Figure 5.3. The significance of the applied force, depth, orientation of the holes, hole radius, and width was highlighted by the bar graph. Hence, it is very important to assess the contribution of these features in the design process of the plain-weave composite with two cut-outs. Also, all these features were ranked based upon the tensile experimental test while for other mechanical tests, separate evaluation is needed to identify the significant features, which have an influence on the structural integrity of the woven laminates. The bottom and top layers were important features in the structural behavior of composite structures with hole/s subjected to tension as also verified by the Pearson map. Thus, the designer should pay attention to them. Length of the specimen had nearly the same effect on the target variable as the middle layers. The importance of the width was also highlighted by the Pearson map. Based on the comparisons of the hole radius and hole configuration the latter was more significan less important than the first considering the stress concentration near the holes.

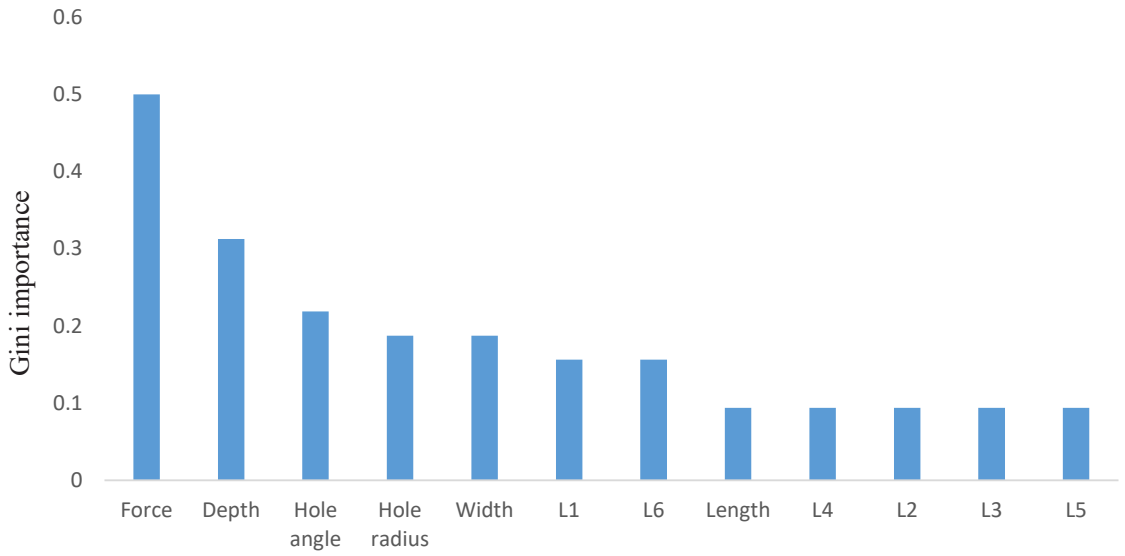

Figure 5.3 Random Forest feature score

5.2.2 Models' evaluation

Dataset were randomly shuffled by the SkLearn library test train selection, after the dataset pre-processing, through various seed values. It was shown here that with the least number of FEM simulations, i.e. 89, the models could be trained. On the other hand, the model should be tested on all the possible combinations of the material and geometry to have affirmed evidence from a mechanical perspective. Thus, 1% of these shuffled data were used for training the ML model (grid search with AutoML (TPOT)) and AutoKeras, while rest (99%) were employed for testing. The grid search was carried out 8 times with random shuffling of the dataset in order to ensure that grid search was not biased to the train data choosing. The full grid search (9000 different combinations of stacked models) was performed carefully and models were tested against the test dataset. Table 5.3 shows the most efficient models and their accuracy. Among all the models, one most complicated (Model-I) and one most accurate (Model-II) model were chosen and the architectural network of these models was shown in Figure. 5.4.

AutoKeras was employed to conduct a grid search among neural networks. Various model architectures evolved with the trials factor of 100 (factor of AutoKeras) and 5 times with data shuffling. This selection was integrated with the framework to identify the most accurate ANN model. The results are given in Table. 5.3. Model-III, with specified characteristics provided in Table. 5.5, was chosen.

Table 5.3 Grid search leaderboard

type	Seed values	R^2	Pre-processing	ML models	Metamodel
Stk	12	0.96	PCA	PolyFeatures, ETR, DTR, GBR	LassoLarsCV
Stk	14	0.93	ZeroCount, MinMaxScaler	DT, ETR, Ridge	XGB
Stk	17	0.96	ZeroCount,RobustScaler	RidgeCV	XBG
Stk (Model-II)	**18**	**0.98**	**MinMaxScaler, RobustScaler**	**GBR, PolyFeatures, LassoLarsCV**	**RidgeCV**
Stk(Model-I)	**19**	**0.89**	**-**	**GBR, PolyFeatures, SGD, DTR**	**LassoLarsCV**
Stk	20	0.95	-	RF, F_regression[a], PolyFeatures	LassoLarsCV
Stk	75	0.96	-	F_regression, XGB	XGB
Stk	100	0.95	ZeroCount, RobustScaler, MaxAbsScaler	XGB, Ridge	GBR
ANN (Model-III)	**12**	**0.80**	**MinMaxScaler**	**[13,32,32,1]**	**-**
ANN	16	0.53	MinMaxScaler	[13,512,128,1]	-
ANN	22	0.71	MinMaxScaler	[13,64,512,1]	-
ANN	100	0.77	MaxScaler	[13,128,1024,16,1]	-

[a] linear model for testing the effect of a single regressor, sequentially for many regressors.

Model-I had a MinMax scaler for pre-processing and contained 5 ML algorithms (GB, DT, KNN, SGD, and PolyFeatures), which were controlled by the Metamodel LassoLarsCV as represented in Figure 5.4. This scaler was incorporated into the Robust scaler in order to pre-process the data. It contained 3 different ML models (Lasso, GB, and PolyFeatures) which were controlled by the RidgeCV.

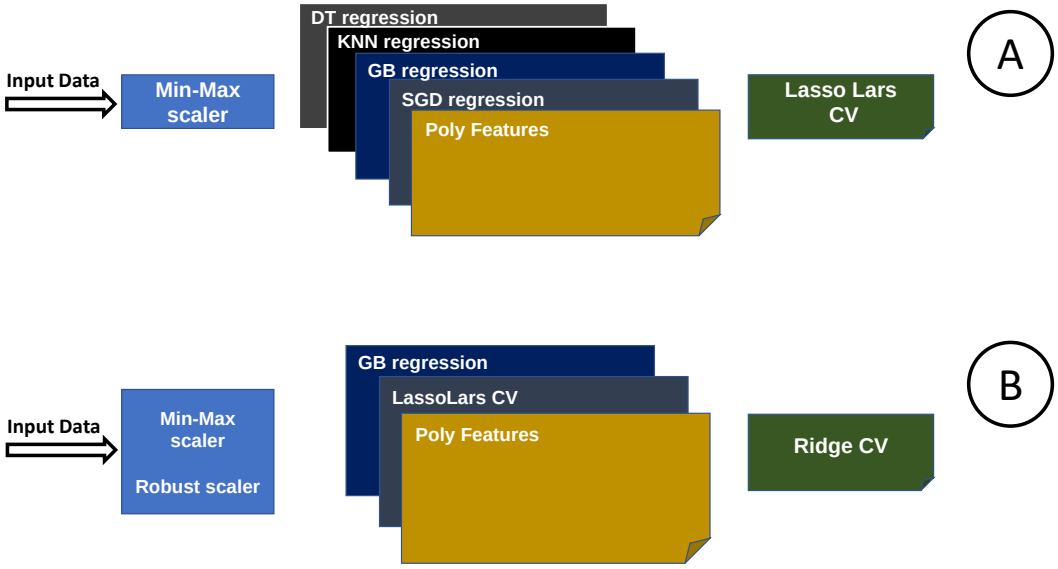

Figure 5.4 Proposed stacked models and hyper-parameters A) Model-I, B) Model-II

Table 5.4 Hyperparameters of stacked models

Model No.	Sub-model	Hyper parameters
Model I	DT	max_depth=7, min_samples_leaf=4, min_samples_split=14
	KNN	n_neighbors=32, p=1, weights="uniform"
	SGD	l1_ratio=0.25, penalty="elasticnet", loss="epsilon_insensitive", power_t=1.0
	GB	n_estimators=100, learning_rate=0.1, max_depth=6, max_features=0.15
		alpha=0.8, min_samples_leaf=13, min_samples_split=5
	PolyF	degree=2, include_bias=False, interaction_only=False
Model II	GB	n_estimators=100, alpha=0.9, learning_rate=0.1, loss="huber", max_depth=2
		max_features=0.55, min_samples_split=13, min_samples_leaf=4, subsample=0.45
	PolyF	degree=2, include_bias=False, interaction_only=False
	LL CV	max_iterant, default=500

Model-III was a neural network with 13 neurons in an input layer and 2 dense layers with 32 neurons in each which were connected to the ReLU with a neuron in an output layer and it consisted of 1537 total trainable parameters.

Table 5.5 Network architecture (Model-III)

Layer(type)	Output shape	Param#
Input_1(Inputlayer)	(None,13)	0
Multi_Category_encoding	(None,13)	0
dense (Dense)	(None,32)	448
re_lu (ReLU)	(None,32)	0
dense_1 (Dense)	(None,32)	1056
re_lu_1 (ReLU)	(None,32)	0
regression_head_1 (Dense)	(None,1)	33
Total Params:1537		
Trainable Params:1537		
Non-Trainable Params:0		

Table 5.6 provided the performance of developed algorithms on the highest stress of the plain-weave composite structures as model metrics. Model-II showed the best performance on the test dataset among those models, with an MAE of 175 and RMSE of 253. Interestingly, the R^2 of the testing data of the ANN model (Model-III) was less than the R^2 value of this metric against train data, which indicates that the model-III has an overfitting issue. ANN could be a helpful algorithm for predicting the maximum stress of the plain-weave composite structures with two interacting cut-outs. However, it was not the best model for this goal. The difference between values of R^2 (between train and test) was less than the ANN model for the other developed stacked algorithms. Model-II had the minimum difference for R^2 between train and test data.

Table 5.6 Model Metrics for the three proposed models

	Training data			Test data			
Model	R^2	RMSE	MAE	R^2	RMSE	MAE	Inference time(s)
Model-I	0.99	137	101.3	0.95	318	219.5	0.13
Model-II	**0.995**	**100.4**	**78.7**	**0.97**	**253**	**175**	**0.030**
Model-III	0.94	343.2	267.1	0.8	654.1	465.1	1.480

The real versus predicted for the testing (blue points) and training (orange points) dataset was depicted in Figure. 5.5 for (a) Model-I, (b) Model-II, and (c) Model-III,

respectively. Whisker plots for each model are shown in Figure. 5.5 (d), Figure. 5.5(e), and Figure. 5.5(f). The major part of the training dataset was accumulated between 0 and 4000 MPa where most of the records of dataset gathered. Obviously, as the points gathered around the red line (45°) for the model, the accuracy of that algorithm was high. It was understood from these figures that the values predicted by the ML and the numerical dataset points matched well in Model-II, but were not well-suited in others two models. The accuracy of the predictions for the numerical investigation was approximately 95%. By increasing the target values (Maximum stress) in Model-III, the error of estimation enhanced and this occurred symmetrically (overestimation and underestimation).

All models in a range of the maximum stress between 0-6k MPa, were relatively accurate considering the error mean values (error mean near zero), according to the whisker plots. most part of high errors were accumulated in the range of 6k-8k MPa. All three proposed models underestimated target values between 6k-8k MPa with an average error of approximately -1000, -600, and -500 for Model-III, Model-II, and Model-I, respectively. It is worth to note that the Model-III, developed by ANN algorithm was more vulnerable to overfitting problem. Moreover, in training 1% of the dataset, the range of randomly chosen output variables might not be similar to that of the test dataset. In the range of 6k-8k MPa, the difference between the minimum and maximum error values was more balanced around zero in Model-II in comparison to other algorithms. It is important to mention that the material behavior alters irregularly as tensile stress enhanced. It made the prediction process much harder than lower values of target variables. Although Model-II performed more accurate than other models, underestimation in the range of 6k-8k MPa was seen which is undesirable from a mechanical perspective.

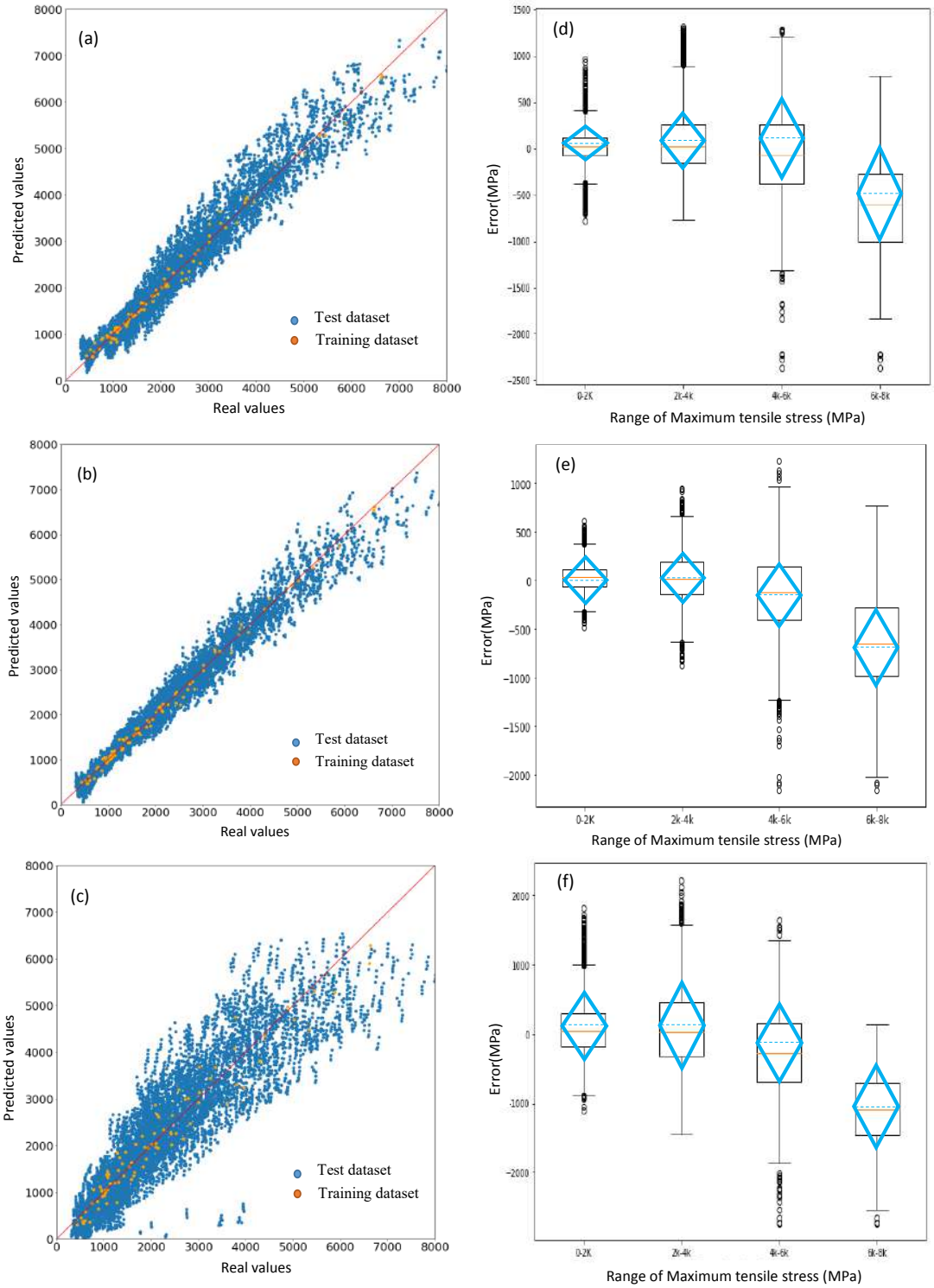

Figure 5.5 Real versus Predicted values and corresponding prediction errors (a) Model-I, (b) Model-II, (c) Model-III, (d) Whisker plot (Model-I), (e) Whisker plot (Model-II), (f) Whisker plot (Model-III)

Polar plot was used in Figure. 5.6 to demonstrate the prediction errors of each model considering the target values. The angle depicted the maximum tensile stress

and the radius shows the error values. The upper limit value of most of the positive errors was 500 MPa, 1000 MPa, and 1500 MPa for Model-II, Model-I, and Model-III, respectively. The lower bond for each suggested algorithm was -500 MPa, -500 MPa, and -1000 MPa, respectively. Negative range of errors was mostly accumulated in model-III. For all the proposed models the errors were large (negatively) for the maximum stress above 7.875k MPa. Model-I had a few negative range while the majority of large negative errors was attributed to the Model-III.

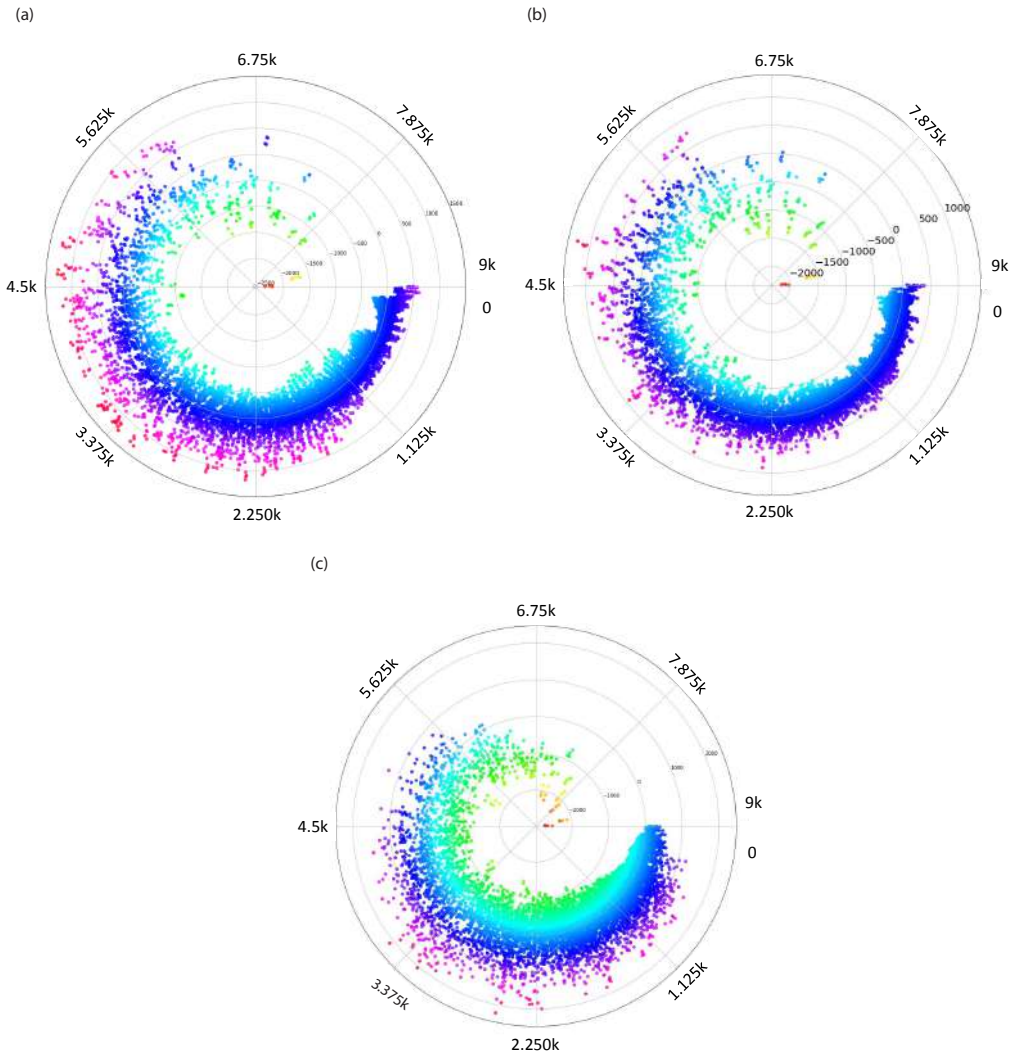

Figure 5.6 Prediction error versus target values (a) Model-I, (b) Model-II, (c) Model-III

Figure. 5.7 represents the prediction error distribution of the target value for the composite laminate with two interacting notches for (a) Model-I, (b) Model-II, and (c) Model-III. The normal distribution of the residuals showed that the models were valid with an acceptable performance. Model-III had wider dispersion of the errors in comparison to the others. Moreover, the frequency of the errors in the mean range for Model-I and Model-II was more than Model-III.

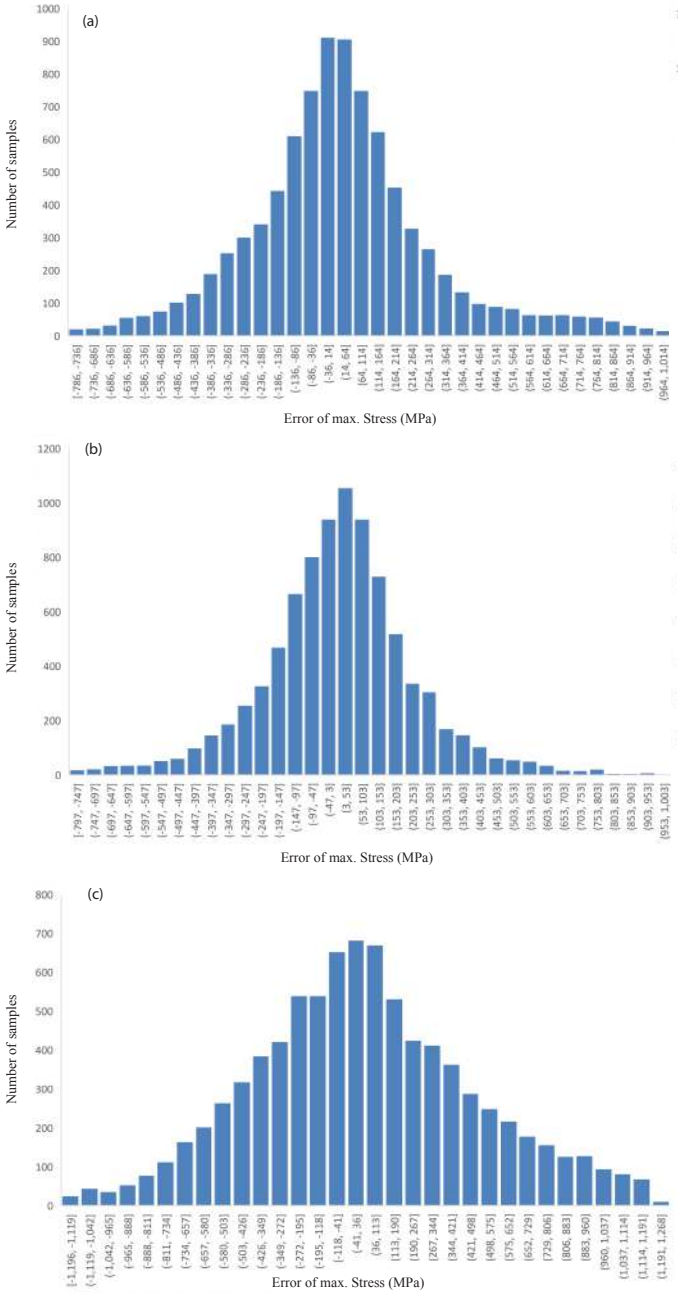

Figure 5.7 Error histogram for maximum tensile stress

Figure. 5.8 (a) shows the prediction error against hole orientation. The error median value near zero was observed for most of the orientations. 0° configuration (transverse to the tension) had a median error larger than zero. It indicated that the accuracy of the ML technique was reduced for this type of orientation and it is more difficult to generalize the pattern in this orientation. Figure. 5.8 (b) represents the prediction error versus force. Nearly all the force ranges provided the zero error median. However, as the force reached 50 kN, the median error moved below zero. This was in well agreement with the maximum stress underestimation prediction given in Figure. 5.9.

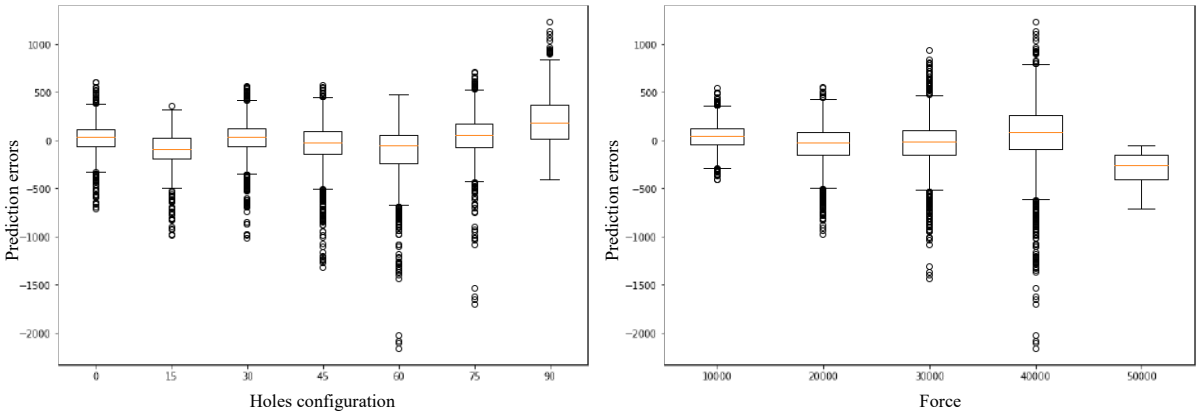

Figure 5.8 Box whisker plot of errors (a) Hole configuration (b) Force

The prediction error of target variables versus maximum stress and force is represented in Figure. 5.9. It Revealed that enhancing the force did not necessarily increase the error of prediction. In large target values, the error of prediction enhanced and resulted in the underestimation which indicated that the stress change patterns were changed in large output values. High ranges of output values imposed irregular deformations on the sample which made it difficult for the ML algorithm to generalize the material behavior. This behavior could be associated with the unpredictable mechanical behavior of the heterogeneous materials on the high target values around the notches that caused the failure of the composite samples.

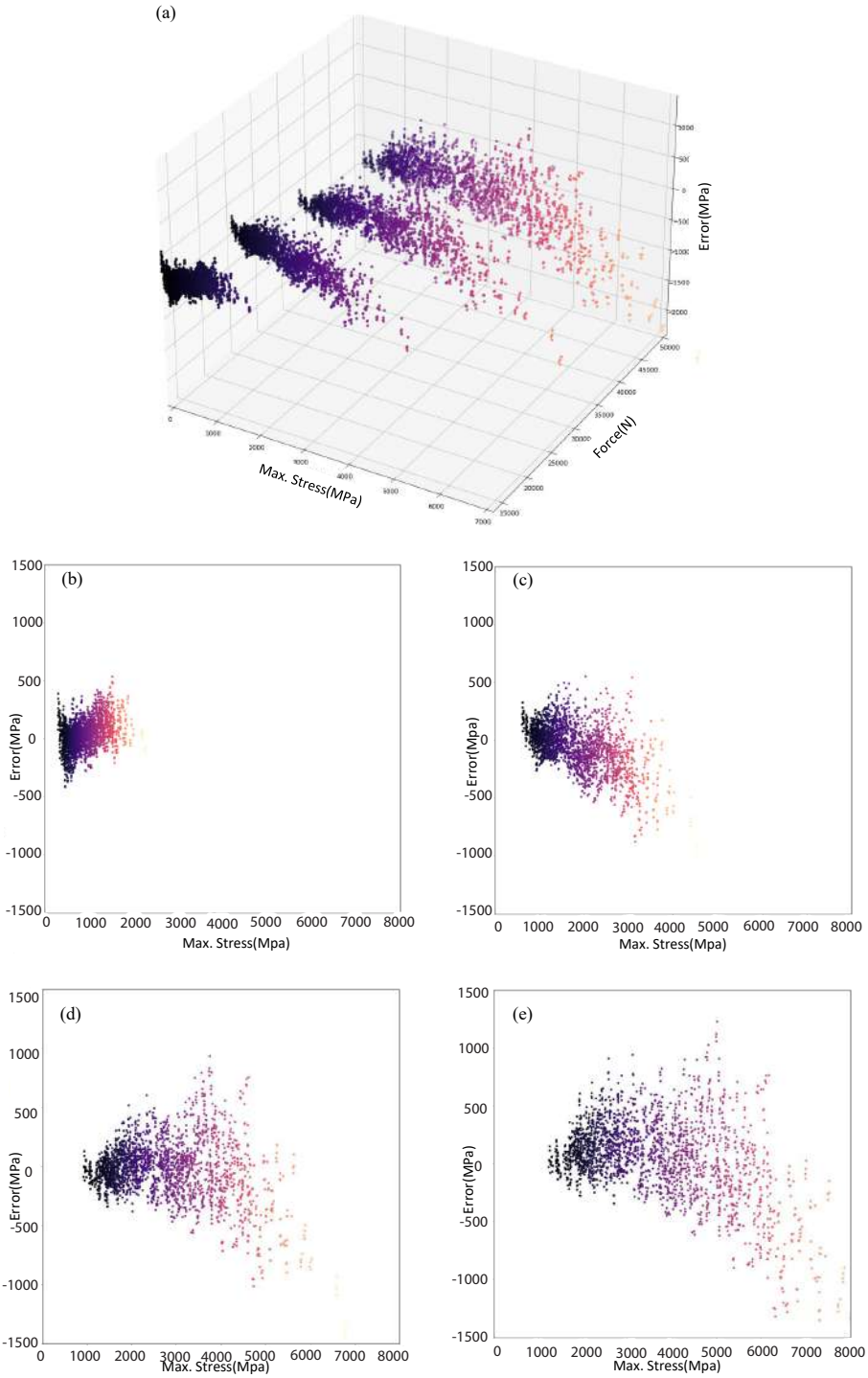

Figure 5.9 Prediction error against maximum stress and applied force (a) 3D plot, (b) Force = 10kN, (c) Force = 20kN, (d) Force = 30kN, (e) Force = 40kN

Maximum tensile stress prediction based on the stacking sequences and geometry variation for plain-weave composite with two interacting holes in different configurations was not studied thoroughly in the literature. There were several key points highlighted here compared to previous works, which were given as followings :

- The data-rich framework constructed was much larger than other research works.
- The geometrical features were investigated in detail which had an important role in different applications.
- The motivation of such division (1% for training) is to train a model with the least amount of data possible that can accurately predict all sorts of combinations.
- The accuracy of the suggested model (Stacked ML) was high enough to be claimed as a representative of the state-of-the-art.

6. Summary and Conclusion

The aim of the PhD thesis was achieved because 4 diagnostic methods (SHM and NDT) for selected FRP materials were analysed. The analyses were focused on ranges of applications of the methods and their limitations. FBG sensors based method was applied for continuous loadings (mechanical and thermal) monitoring of AM CFRP material. While IRT and DIC were applied for analyses of degradation processes that occur in woven composites with hole(s). ML was later on applied for prediction of the stress conditions and fracture process in woven composites with interacting notches for the first time.

The thesis of the dissertation has been proven because the work presents the results of successfully conducted experimental and numerical analyses related to selected diagnostic methods (SHM and NDT) with their application to continuous monitoring and degradation processes of FRP structure. First of all, the FBG sensors were successfully embedded in the 3D printed composite structures to measure the thermal strain of material exposed to elevated and sub zero temperatures without affecting the durability and structural performance of the material. Secondly, the PSC and EPSC were shown to be not sufficient to provide the strength prediction of woven composites including interacting holes with balanced stacking sequences, though they were shown to be applicable in quasi-isotropic composites. Therefore, NDT techniques such as DIC and IRT were further required to predict the strength and damage evolution of these materials. Finally, novel stacked ML models were developed which outperform other algorithms in providing the maximum tensile stress prediction accurately.

Referring to the thorough literature review as well as the results of numerical and experimental analysis, several innovative elements can be identified in the thesis. These are as following:

- Development of a numerical model of FRP structure with holes under loading
- Investigation on the application of theoretical models for strength prediction of woven structures with holes

- Construction of a measurement stand for analyses of thermal loading influence on FRP structure with embedded FBG sensor
- Modification of the test stand for tensile tests by adding a measurement system developed on the basis of FBG sensors
- Analysis of the degradation processes of FRP structures with holes and determination the dominant type (matrix cracking, etc.)
- Developing novel method to accurately predict the maximum tensile stress of the woven composites with interacting holes under tension

It should be emphasized that the research related to embedding FBG sensors into AM FRP structure and application for continuous monitoring of strain due to thermal and mechanical loading is a pioneering task at the Institute of Fluid Flow Machinery the Polish Academy of Sciences in Gdańsk. All the works in this thesis were conducted for the first time and it is a comprehensive and thorough work which highlights the importance of defect diagnosis techniques, i.e. utilization of-embedded FBG sensors, using NDT techniques on damage diagnosis of woven composites with notches, and application of ML models on prediction of the structural performance of composite structures with interacting holes.

The Institute of Fluid-Flow Machinery of the Polish Academy of Sciences in Gdańsk is one of the few research units in Poland dealing with this topic. Undertaking research on this topic required an in-depth analysis of the global state of knowledge in the field covered by this thesis, the design and creation of a measurement system, and the development of procedures for recording and processing the collected measurement data.

6.1 Conclusion

This PhD thesis study aimed firstly at exploring the application of AM on the fabrication of CFRP samples embedded FBG sensors and the ability of FBG sensors to detect the thermal strain correctly. Secondly, the effect of drilling two interacting holes on the plain-weave composite structures was explained thoroughly due to their various industrial applications. Finally, ML techniques were developed to predict the maximum tensile stress in the vicinity of the holes for different notch configuration and composite geometry.

6.1.1 AM for CFRP embedded FBG

FDM techniques was employed to fabricate a 4-layer ($[0,0]_s$) laminate. Numerical simulation outcomes given by ABAQUS were compared with experimental results of mean value of three different samples. An effect of increase and reduction in temperature on the thermal strain induced by temperature gradient was investigated at stable humidity level. Environmental chamber used for experimental validation. The following conclusion could be drawn:

- 3D printing could be used as a green manufacturing technique to fabricate CFRP sample with embedded FBG sensors possesses good quality.
- Thermal strains given by the ABAQUS FEM model were well-matched with that of FBG sensors embedded in CFRP material.
- The difference between numerical and experimental outcomes for elevated and subzero temperatures were approximately 6% and 4%, respectively.
- The difference between numerical and experimental works could be attributed to the voids/gaps inside the sample while fabrication. The specimen was considered to be ideal in numerical simulation
- The thermal strain values given by embedded FBG sensors in the specimens were nearly same. Thus, the averaged strain of the CFRP specimens were taken into account in comparative study.

6.1.2 Plain-weave composites with two interacting holes

FEM techniques integrated with the DIC and IRT were carried out to assess the SCF of woven composite specimens including one single hole or two interacting holes, at different configurations (0°, 45°, and 90°), subjected to tensile loading. The strength prediction as well as stress analysis was conducted. It was shown that adding one more hole with the same size in the same loading direction led to increase of failure strength and reduction in SCF near the hole. The processing zone of specimens with two interacting notches was determined by DIC method. The prediction of strength for sample with critical region outside and/or between cut-outs was performed with the PSC and EPSC techniques. Also, the characteristic distances were found through the DIC and FEM, which were well-matched. Finally,

progressive failure analysis was performed using IRT method to find the effect of two interacting notches on the failure progression

The following conclusion were provided:

- The PSC technique could be employed directly to predict the failure strength of the specimen with processing zone at the outer periphery of holes
- It was concluded that the EPSC approach could not be utilized for woven composites, whereas it could for quasi-isotropic materials.
- Earliest initial axial-splitting in the vicinity of the notche(s) was occurred for 2H45 sample while the latest was identified for 2H90 specimen, which was directly related with the SCF values.
- Axial splitting proposed a more precise crack blunting influence for 2H90 with respect to an open-hole sample.
- Delamination dominated failure was happened for 2H90 in comparison to an open-notch specimen, where the failure was mostly controlled by transverse matrix cracking.
- The damage was accumulated in area between the holes but later a processing zone was shifted towards the outer side of notches in 2H45 sample, which led to a higher maximum strength of 2H45 specimen comparing with the 2H0 sample.
- A slanted through the thickness large area delamination morphology for 2H90 sample was observed with respect to a matrix dominated failure in 1H specimen with minor interfacial failure, as shown by fracture surfaces inspection.
- The major damage was transverse matrix cracking for 2H0 sample which kept confined in the area between the holes. Whereas, high amount of interfacial failure, fiber rotation, and damage growth was seen between the holes as shown in 2H45 specimen.

6.1.3 Machine Learning methods on composites with hole/s

A comparative study was carried out to predict the maximum tensile stress near the interacting notches in the plain-weave composite structures. The data-rich framework was constructed via the Python library within the ABAQUS FEM software.

various FEM numerical simulations were performed for different cases of geometry and configuration of holes. The stress behavior for all the cases of composite plate was predicted the and compared with the target values obtained by the suggested models. Three ML approaches were chosen for prediction of the target variable. The algorithm was based on the maximum tensile stress values for each layer given by the numerical work.

- The stacked model was performed for comparison through a full-grid search. Model-II, a combination of the PolyFeatures, GB regression, and LassoLarsCV provided the best performance among all developed algorithms with respect to the tensile stress achieved through the FEM simulations.
- Suggested ANN model (Model-III) was not more accurate than the other proposed models. On the other hand, the most complex developed model of ML did not necessarily detect the outcomes accurately.
- The bottom/top layers was the most important factor in the design process of composites with two notches verified by the pairwise correlation heat map.
- The designer should carefully design for the up/bottom layers of the woven composite structures with two cut-outs in order to make sure the structural integrity.
- The strength of the proposed model was shown by using 60 training data to predict 8900 output values achieved by the numerical simulations with high accuracy.
- The preciseness of the prediction by the suggested model was reduced for the large tensile stress values,
- Stacked model could be generalized to other composite laminates with hole/s with different orientations and plate with various geometries.

  The provided ML model eased the obtaining of the maximum stress for composites with two interacting notches with different configurations, holes diameter, and plate geometry. Thus, exhaustive simulations and labor work could be neglected led to the reduction of final costs associated with design and test. It was concluded that the stacked model with 60-80 different simulations were enough to predict the maximum stress for the samples under tension.

6.2 Plans and prospective developments

Several suggestions for future work were proposed, which could make a strong contribution for the analysis of the composite structures fabricated by AM, through SHM technique. Also, more works should be conducted to understand the failure process of the composite plates with two interacting holes. Finally, more applicability of ML methods on the composite structures with two interacting holes were discussed.

6.2.1 AM for CFRP embedded FBG

The results of the first section could be taken into account as motivation for more developing AM techniques of composite structures including FBG sensors. It will be required to consider different stacking sequences while 3D printing the CFRP specimen. The results of FBG sensor might be affected by the orientation of them with respect to the layer orientation. Also, different fiber material, e.g. glass, natural, and etc. could be employed in composite structures to understand whether the FBG sensor could detect the thermal strain correctly. Also, mechanical tests such as three point bending should be further implemented on CFRP samples to verify the applicability of FBG sensors on the correct evaluation of mechanical behavior of Additively Manufactured composite structures.

6.2.2 Plain-weave composites with two interacting holes

There are several works that are required to be conducted in order to thoroughly understand the failure and damage mechanisms in composite structures with two interacting holes. The continuation of this work will be applying various failure criterion to investigate the influence of holes in different configuration on the fracture behavior of woven composite materials. Also, SHM technique could be added to precisely measure mechanical attributes and compare it with numerical simulation. Stacking sequences, as discussed earlier, might have a noticeable effect on the failure behavior of composite structures. Thus, it will be required to take into account the layer orientation while analyzing those structures.

6.2.3 Machine Learning methods on composites with hole/s

Although, the proposed model could accurately predict the maximum stress for the samples under tension, it should be further investigated in other loading conditions. Therefore, future works will be required to study the effect of inputs in different output values associated with mechanical loading. Also, in order to further verify the prediction accuracy, an extended work should be conducted wherein the stress patterns given by the digital image correlation, for specific input combinations will be compared with the results given by the most accurate model developed ML model.

BIBLIOGRAPHY

Abbaszadeh, M., Soltani-Mohammadi, S., & Ahmed, A. N. (2022). Optimization of support vector machine parameters in modeling of iju deposit mineralization and alteration zones using particle swarm optimization algorithm and grid search method. *Computers & Geosciences*, *165*, 105140.

Achache, H., Boutabout, B., & Ouinas, D. (2013). Mechanical behavior of laminated composites with circular holes. In *Key Engineering Materials*, volume 550, (pp. 1–8). Trans Tech Publ.

Ahmed, O., Wang, X., Tran, M.-V., & Ismadi, M.-Z. (2021). Advancements in fiber-reinforced polymer composite materials damage detection methods: towards achieving energy-efficient shm systems. *Composites Part B: Engineering*, *223*, 109136.

Ahsan, M. M., Mahmud, M. P., Saha, P. K., Gupta, K. D., & Siddique, Z. (2021). Effect of data scaling methods on machine learning algorithms and model performance. *Technologies*, *9*(3), 52.

Alencar, M., Rambo, M., Botelho, G., Barros, P., Sergio, R., Borges, M., & Bertuol, D. (2023). Feasibility study of incorporation of bamboo plant fibers in cement matrices. *Sustainable Chemistry for the Environment*, *2*, 100020.

Amaro, A. M., Reis, P., De Moura, M., & Neto, M. (2013). Influence of open holes on composites delamination induced by low velocity impact loads. *Composite Structures*, *97*, 239–244.

Ataş, A., Arslan, N., & Sen, F. (2009). Failure analysis of laminated composite plates with two parallel pin-loaded holes. *Journal of Reinforced Plastics and Composites*, *28*(10), 1265–1276.

Avci, O., Abdeljaber, O., Kiranyaz, S., Hussein, M., Gabbouj, M., & Inman, D. J. (2021). A review of vibration-based damage detection in civil structures: From traditional methods to machine learning and deep learning applications. *Mechanical systems and signal processing*, *147*, 107077.

Azami, M., Siahsarani, A., Hadian, A., Kazemi, Z., Rahmatabadi, D., Kashani-Bozorg, S. F., & Abrinia, K. (2023). Laser powder bed fusion of alumina/fe–ni ceramic matrix particulate composites impregnated with a polymeric resin. *Journal of Materials Research and Technology*, *24*, 3133–3144.

Bagherzadeh, F., Mehrani, M.-J., Basirifard, M., & Roostaei, J. (2021). Comparative study on total nitrogen prediction in wastewater treatment plant and effect of various feature selection methods on machine learning algorithms performance. *Journal of Water Process Engineering*, *41*, 102033.

Bagherzadeh, F. & Shafighfard, T. (2022a). Ensemble machine learning approach for evaluating the material characterization of carbon nanotube-reinforced cementitious composites. *Case Studies in Construction Materials*, *17*, e01537.

Bagherzadeh, F. & Shafighfard, T. (2022b). Ensemble machine learning approach for evaluating the material characterization of carbon nanotube-reinforced cementitious composites. *Case Studies in Construction Materials*, *17*, e01537.

Balcıoğlu, H. E. & Seçkin, A. Ç. (2021). Comparison of machine learning methods and finite element analysis on the fracture behavior of polymer composites. *Archive of Applied Mechanics*, *91*(1), 223–239.

Brahim, A. O., Belaidi, I., Khatir, S., Le Thanh, C., Mirjalili, S., & Wahab, M. A. (2023). Strength prediction of a steel pipe having a hemi-ellipsoidal corrosion defect repaired by gfrp composite patch using artificial neural network. *Composite Structures*, *304*, 116299.

Brischetto, S. & Torre, R. (2020). Tensile and compressive behavior in the experimental tests for pla specimens produced via fused deposition modelling technique. *Journal of Composites Science*, *4*(3), 140.

Califano, A., Chandarana, N., Grassia, L., D'Amore, A., & Soutis, C. (2020). Damage detection in composites by artificial neural networks trained by using in situ distributed strains. *Applied Composite Materials*, *27*(5), 657–671.

Caminero, M., Chacón, J., García-Moreno, I., & Rodríguez, G. (2018). Impact damage resistance of 3d printed continuous fibre reinforced thermoplastic composites using fused deposition modelling. *Composites Part B: Engineering*, *148*, 93–103.

Chan, T. H., Yu, L., Tam, H.-Y., Ni, Y.-Q., Liu, S., Chung, W., & Cheng, L. (2006). Fiber bragg grating sensors for structural health monitoring of tsing ma bridge: Background and experimental observation. *Engineering structures*, *28*(5), 648–659.

Chandarana, N., Sanchez, D. M., Soutis, C., & Gresil, M. (2017). Early damage detection in composites during fabrication and mechanical testing. *Materials*, *10*(7), 685.

Christ, S., Schnabel, M., Vorndran, E., Groll, J., & Gbureck, U. (2015). Fiber reinforcement during 3d printing. *Materials Letters*, *139*, 165–168.

Compton, B. G., Post, B. K., Duty, C. E., Love, L., & Kunc, V. (2017). Thermal analysis of additive manufacturing of large-scale thermoplastic polymer composites. *Additive Manufacturing*, *17*, 77–86.

Cristea, M., Ionita, D., & Iftime, M. M. (2020). Dynamic mechanical analysis investigations of pla-based renewable materials: How are they useful? *Materials*, *13*(22), 5302.

Daghigh, V., Lacy Jr, T. E., Daghigh, H., Gu, G., Baghaei, K. T., Horstemeyer, M. F., & Pittman Jr, C. U. (2020). Machine learning predictions on fracture toughness of multiscale bio-nano-composites. *Journal of Reinforced Plastics and Composites*, *39*(15-16), 587–598.

Deane, S., Avdelidis, N. P., Ibarra-Castanedo, C., Zhang, H., Nezhad, H. Y., Williamson, A. A., Mackley, T., Davis, M. J., Maldague, X., & Tsourdos, A. (2019). Application of ndt thermographic imaging of aerospace structures. *Infrared Physics & Technology*, *97*, 456–466.

Dizon, J. R. C., Espera Jr, A. H., Chen, Q., & Advincula, R. C. (2018). Mechanical characterization of 3D-printed polymers. *Addit. Manuf.*, *20*, 44–67.

Dong, Y. & Li, Y. (2022). A review on the mechanical property evaluation and optimization design of fabric rubber composite structure. *Composites Part C: Open Access*, *8*, 100289.

Economidou, S. N. & Karalekas, D. (2016). Optical sensor-based measurements of thermal expansion coefficient in additive manufacturing. *Polymer Testing*, *51*, 117–121.

Feng, K., González, A., & Casero, M. (2021). A knn algorithm for locating and quantifying stiffness loss in a bridge from the forced vibration due to a truck crossing at low speed. *Mechanical Systems and Signal Processing*, *154*, 107599.

Ford, S. & Despeisse, M. (2016). Additive manufacturing and sustainability: an exploratory study of the advantages and challenges. *Journal of cleaner Production*, *137*, 1573–1587.

Galos, J. (2020). Thin-ply composite laminates: a review. *Composite Structures*, *236*, 111920.

Gardner, L. (2022). Metal additive manufacturing in structural engineering–review, opportunities and outlook. *Current Perspectives and New Directions in Mechanics, Modelling and Design of Structural Systems*, *47*, 3–8.

Ghezzo, F., Giannini, G., Cesari, F., & Caligiana, G. (2008). Numerical and experimental analysis of the interaction between two notches in carbon fibre laminates. *Composites Science and Technology*, *68*(3-4), 1057–1072.

Ghobadi, A. (2017). Common type of damages in composites and their inspections. *World Journal of Mechanics*, *7*(2), 24–33.

Giaccari, P., Dunkel, G. R., Humbert, L., Botsis, J., Limberger, H. G., & Salathé, R. P. (2004). On a direct determination of non-uniform internal strain fields using fibre bragg gratings. *Smart materials and structures*, *14*(1), 127.

Groves, R. (2018). 3.12 inspection and monitoring of composite aircraft structures. In *Reference Module in Materials Science and Materials Engineering: Comprehensive Composite Materials II* (pp. 300–311). Elservier.

Guessasma, S., Montavon, G., & Coddet, C. (2004). Modeling of the aps plasma spray process using artificial neural networks: basis, requirements and an example. *Computational Materials Science*, *29*(3), 315–333.

Hakim, I. A., Donaldson, S. L., Meyendorf, N. G., & Browning, C. E. (2017). Porosity effects on interlaminar fracture behavior in carbon fiber-reinforced polymer composites. *Materials Sciences and Applications*, *8*(2), 170–187.

Hao, W., Liu, Y., Wang, T., Guo, G., Chen, H., & Fang, D. (2019). Failure analysis of 3d printed glass fiber/pa12 composite lattice structures using dic. *Composite Structures*, *225*, 111192.

Hassen, A. A., Betters, E., Tsiamis, N., West, J., Smith, T., Billah, K. M. M., Nuttall, D., Kumar, V., Smith, S., & Kunc, V. (2022). Joining technique for in-oven/autoclave molds manufactured by large scale polymer additive manufacturing. *Manufacturing Letters*, *32*, 77–82.

Haywood-Alexander, M., Dervilis, N., Worden, K., Cross, E. J., Mills, R. S., & Rogers, T. J. (2021). Structured machine learning tools for modelling characteristics of guided waves. *Mechanical Systems and Signal Processing*, *156*, 107628.

Heidari-Rarani, M., Rafiee-Afarani, M., & Zahedi, A. (2019). Mechanical characterization of fdm 3d printing of continuous carbon fiber reinforced pla composites. *Composites Part B: Engineering*, *175*, 107147.

Hill, K. O., Malo, B., Bilodeau, F., Johnson, D., & Albert, J. (1993). Bragg gratings fabricated in monomode photosensitive optical fiber by uv exposure through a phase mask. *Applied Physics Letters*, *62*(10), 1035–1037.

Hofer, A.-K., Kocjan, A., & Bermejo, R. (2022). High-strength lithography-based additive manufacturing of ceramic components with rapid sintering. *Additive Manufacturing*, *59*, 103141.

Hosseini, V. A., Cederberg, E., Hurtig, K., & Karlsson, L. (2021). A physical simulation technique for cleaner and more sustainable research in additive manufacturing. *Journal of Cleaner Production*, *285*, 124910.

Hosseinpour, M., Daei, M., Zeynalian, M., & Ataei, A. (2023). Neural networks-based formulation for predicting ultimate strength of bolted shear connectors in composite cold-formed steel beams. *Engineering Applications of Artificial Intelligence*, *118*, 105614.

Hou, Z., Tian, X., Zhang, J., & Li, D. (2018). 3d printed continuous fibre reinforced composite corrugated structure. *Composite Structures*, *184*, 1005–1010.

Hu, Y., Ladani, R. B., Brandt, M., Li, Y., & Mouritz, A. P. (2021). Carbon fibre damage during 3d printing of polymer matrix laminates using the fdm process. *Materials & Design*, *205*, 109679.

Kamath, G., Sundaram, R., Gupta, N., & Subba Rao, M. (2010). Damage studies in composite structures for structural health monitoring using strain sensors. *Structural Health Monitoring*, *9*(6), 497–512.

Karakuzu, R., Taylak, N., İçten, B. M., & Aktaş, M. (2008). Effects of geometric parameters on failure behavior in laminated composite plates with two parallel pin-loaded holes. *Composite structures*, *85*(1), 1–9.

Kaveh, A., Eslamlou, A. D., Javadi, S., & Malek, N. G. (2021). Machine learning regression approaches for predicting the ultimate buckling load of variable-stiffness composite cylinders. *Acta Mechanica*, *232*(3), 921–931.

Kim, K. & Hong, J.-s. (2017). A hybrid decision tree algorithm for mixed numeric and categorical data in regression analysis. *Pattern Recognition Letters*, *98*, 39–45.

Kodama, H. (1981). Automatic method for fabricating a three-dimensional plastic model with photo-hardening polymer. *Review of Scientific Instruments*, *52*(11), 1770–1773.

Koh, T. Y. & Sutradhar, A. (2022). Untethered selectively actuated microwave 4d printing through ferromagnetic pla. *Additive Manufacturing*, *56*, 102866.

Kouka, M. A., Abbassi, F., Demiral, M., Ahmad, F., Soula, M., & Al Housni, F. (2021). Behaviour of woven-ply pps thermoplastic laminates with interacting circular holes under tensile loading: An experimental and numerical study. *Engineering Fracture Mechanics*, *251*, 107802.

Kousiatza, C., Tzetzis, D., & Karalekas, D. (2019). In-situ characterization of 3d printed continuous fiber reinforced composites: A methodological study using fiber bragg grating sensors. *Composites Science and Technology*, *174*, 134–141.

Krajangsawasdi, N., Blok, L. G., Hamerton, I., Longana, M. L., Woods, B. K., & Ivanov, D. S. (2021). Fused deposition modelling of fibre reinforced polymer composites: a parametric review. *Journal of Composites Science*, *5*(1), 29.

Kumar, L. J., Pandey, P. M., & Wimpenny, D. I. (2019). *3D printing and additive manufacturing technologies*, volume 311. Springer.

Lai, M., Friedrich, K., Botsis, J., & Burkhart, T. (2010). Evaluation of residual strains in epoxy with different nano/micro-fillers using embedded fiber bragg grating sensor. *Composites Science and Technology*, *70*(15), 2168–2175.

Lee, H., Lim, H. J., Skinner, T., Chattopadhyay, A., & Hall, A. (2022). Automated fatigue damage detection and classification technique for composite structures using lamb waves and deep autoencoder. *Mechanical Systems and Signal Processing*, *163*, 108148.

Li, Q., Zhao, W., Li, Y., Yang, W., & Wang, G. (2019). Flexural properties and fracture behavior of cf/peek in orthogonal building orientation by fdm: Microstructure and mechanism. *Polymers*, *11*(4), 656.

Liang, Z., Liu, D., Wang, X., Zhang, J., Wu, H., Qing, X., & Wang, Y. (2022). Fbg-based strain monitoring and temperature compensation for composite tank. *Aerospace Science and Technology*, *127*, 107724.

Liao, M., Liang, S., Luo, R., & Xiao, Y. (2022). The cooperative deformation test of an embedded fbg sensor and strain correction curve verification. *Construction and Building Materials*, *342*, 128029.

Liu, Y., Lei, Z., Zhu, R., Shang, Y., & Bai, R. (2022). Artificial neural network prediction of residual compressive strength of composite stiffened panels with open crack. *Ocean Engineering*, *266*, 112771.

Liu, Y., Zhang, L., Li, Z., Chen, Z., Huang, K., & Guo, L. (2022). Investigation on damage evolution of open-hole plain woven composites under tensile load by acoustic emission signal analysis. *Composite Structures*, *305*, 116481.

Lu, L., Hou, J., Yuan, S., Yao, X., Li, Y., & Zhu, J. (2023). Deep learning-assisted real-time defect detection and closed-loop adjustment for additive manufacturing of continuous fiber-reinforced polymer composites. *Robotics and Computer-Integrated Manufacturing*, *79*, 102431.

Lu, L., Yuan, S., Yao, X., Li, Y., Zhu, J., & Zhang, W. (2023). In-situ process evaluation for continuous fiber composite additive manufacturing using multisensing and correlation analysis. *Additive Manufacturing*, *74*, 103721.

Luan, C., Yao, X., Zhang, C., Wang, B., & Fu, J. (2019). Large-scale deformation and damage detection of 3d printed continuous carbon fiber reinforced polymer-matrix composite structures. *Composite Structures*, *212*, 552–560.

Ma, S., Fu, S., Wang, Q., Xu, L., He, P., Sun, C., Duan, X., Zhang, Z., Jia, D., & Zhou, Y. (2022). 3d printing of damage-tolerant martian regolith simulant-based geopolymer composites. *Additive Manufacturing*, *58*, 103025.

Maksymovych, O. & Illiushyn, O. (2017). Stress calculation and optimization in composite plates with holes based on the modified integral equation method. *Engineering Analysis with Boundary Elements*, *83*, 180–187.

Mazumdar, S., Karthikeyan, D., Pichler, D., Benevento, M., & Frassine, R. (2017). State of the composites industry report for 2017. *Composites Manufacturing Magazine*, *2*.

Measures, R. M. & Abrate, S. (2002). Structural monitoring with fiber optic technology. *Appl. Mech. Rev.*, *55*(1), B10–B11.

Melkumova, L. & Shatskikh, S. Y. (2017). Comparing ridge and lasso estimators for data analysis. *Procedia engineering*, *201*, 746–755.

Meltz, G., Morey, W. W., & Glenn, W. H. (1989). Formation of bragg gratings in optical fibers by a transverse holographic method. *Optics letters*, *14*(15), 823–825.

Mieloszyk, M., Andrearczyk, A., Majewska, K., Jurek, M., & Ostachowicz, W. (2020). Polymeric structure with embedded fiber bragg grating sensor manufactured using multi-jet printing method. *Measurement*, *166*, 108229.

Mieloszyk, M., Majewska, K., & Andrearczyk, A. (2022). Embedded optical fibre with fibre bragg grating influence on additive manufactured polymeric structure durability. *Materials*, *15*(7), 2653.

Mieloszyk, M., Majewska, K., & Ostachowicz, W. (2020). Studies of fibre reinforced polymer samples with embedded fbg sensors. In *Proceedings of the 13th International Conference on Damage Assessment of Structures*, (pp. 926–936). Springer.

Mieloszyk, M., Majewska, K., & Ostachowicz, W. (2021). Application of embedded fibre bragg grating sensors for structural health monitoring of complex composite structures for marine applications. *Marine Structures*, *76*, 102903.

Mieloszyk, M., Shafighfard, T., Majewska, K., & Andrearczyk, A. (2023). An influence of temperature on fiber bragg grating sensor embedded into additive manufactured structure. In *European Workshop on Structural Health Monitoring*, (pp. 495–501). Springer.

N'dri, K., Charpentier, N., Hirsinger, L., Gilbin, A., & Barriere, T. (2023). Highly loaded magnetocaloric composites by la (fe, si) 13h powder dedicated to extrusion-based additive manufacturing applications. *Powder Technology*, *425*, 118616.

Nguyen, M. H. & Waas, A. M. (2020). A novel mode-dependent and probabilistic semi-discrete damage model for progressive failure analysis of composite laminates-part i: Meshing strategy and mixed-mode law. *Composites Part C: Open Access*, *3*, 100073.

Oromiehie, E., Prusty, B. G., Compston, P., & Rajan, G. (2018). Characterization of process-induced defects in automated fiber placement manufacturing of composites using fiber bragg grating sensors. *Structural health monitoring*, *17*(1), 108–117.

Özaslan, E., Güler, M. A., Yetgin, A., & Acar, B. (2019). Stress analysis and strength prediction of composite laminates with two interacting holes. *Composite Structures*, *221*, 110869.

Özaslan, E., Yetgin, A., Acar, B., & Güler, M. A. (2021). Damage mode identification of open hole composite laminates based on acoustic emission and digital image correlation methods. *Composite Structures*, *274*, 114299.

Pal, P. & Ray, C. (2002). Progressive failure analysis of laminated composite plates by finite element method. *Journal of reinforced plastics and composites*, *21*(16), 1505–1513.

Pandita, S. D., Nishiyabu, K., & Verpoest, I. (2003). Strain concentrations in woven fabric composites with holes. *Composite Structures*, *59*(3), 361–368.

Park, S. & Fu, K. K. (2021). Polymer-based filament feedstock for additive manufacturing. *Composites Science and Technology*, *213*, 108876.

Peng, W., Bin, Z., Shouling, D., Lei, L., & Huang, C. (2021). Effects of fdm-3d printing parameters on mechanical properties and microstructure of cf/peek and gf/peek. *Chinese Journal of Aeronautics*, *34*(9), 236–246.

Pokkalla, D. K., Hassen, A. A., Nuttall, D., Tsiamis, N., Rencheck, M. L., Kumar, V., Nandwana, P., Joslin, C. B., Blanchard, P., Tamhankar, S. L., et al. (2023). A novel additive manufacturing compression overmolding process for hybrid metal polymer composite structures. *Additive Manufacturing Letters*, *5*, 100128.

Quan, Z., Wu, A., Keefe, M., Qin, X., Yu, J., Suhr, J., Byun, J.-H., Kim, B.-S., & Chou, T.-W. (2015). Additive manufacturing of multi-directional preforms for composites: opportunities and challenges. *Materials Today*, *18*(9), 503–512.

Rajpal, R., Lijesh, K., & Gangadharan, K. (2018). Parametric studies on bending stiffness and damping ratio of sandwich structures. *Additive Manufacturing*, *22*, 583–591.

Rimašauskas, M., Kuncius, T., & Rimašauskienė, R. (2019). Processing of carbon fiber for 3d printed continuous composite structures. *Materials and Manufac-*

turing Processes, *34*(13), 1528–1536.

Safaee, S., Schock, M., Joyee, E. B., Pan, Y., & Chen, R. K. (2022). Field-assisted additive manufacturing of polymeric composites. *Additive Manufacturing*, *51*, 102642.

Saleh, M., Anwar, S., Al-Ahmari, A. M., & Alfaify, A. (2022). Compression performance and failure analysis of 3d-printed carbon fiber/pla composite tpms lattice structures. *Polymers*, *14*(21), 4595.

Santo, J., Penumakala, P. K., & Adusumalli, R. B. (2021). Mechanical and electrical properties of three-dimensional printed polylactic acid–graphene–ca rbon nanofiber composites. *Polymer Composites*, *42*(7), 3231–3242.

Sedgwick, P. (2012). Pearson's correlation coefficient. *Bmj*, *345*.

Sezer, H. K. & Eren, O. (2019). Fdm 3d printing of mwcnt re-inforced abs nanocomposite parts with enhanced mechanical and electrical properties. *Journal of manufacturing processes*, *37*, 339–347.

Shaffer, G. D. (1993). An archaeomagnetic study of a wattle and daub building collapse. *Journal of Field Archaeology*, *20*(1), 59–75.

Shafighfard, T., Bagherzadeh, F., Rizi, R. A., & Yoo, D.-Y. (2022). Data-driven compressive strength prediction of steel fiber reinforced concrete (sfrc) subjected to elevated temperatures using stacked machine learning algorithms. *Journal of Materials Research and Technology*, *21*, 3777–3794.

Shafighfard, T., Cender, T. A., & Demir, E. (2020). Additive manufacturing of compliance optimized variable stiffness composites through short fiber alignment along curvilinear paths. *Additive Manufacturing*, *37*, 101728.

Shafighfard, T., Demir, E., & Yildiz, M. (2019). Design of fiber-reinforced variable-stiffness composites for different open-hole geometries with fiber continuity and curvature constraints. *Composite Structures*, *226*, 111280.

Shafighfard, T. & Mieloszyk, M. (2022). Experimental and numerical study of the additively manufactured carbon fibre reinforced polymers including fibre bragg grating sensors. *Composite Structures*, *299*, 116027.

Shibata, N., Shibata, S., & Edahiro, T. (1981). Refractive index dispersion of lightguide glasses at high temperature. *Electronics letters*, *8*(17), 310–311.

Shirazi, M. I., Khatir, S., Benaissa, B., Mirjalili, S., & Wahab, M. A. (2023). Damage assessment in laminated composite plates using modal strain energy and yuki-ann algorithm. *Composite Structures*, *303*, 116272.

Solis, A., Barbero, E., & Sánchez-Sáez, S. (2020). Analysis of damage and interlaminar stresses in laminate plates with interacting holes. *International Journal of Mechanical Sciences*, *165*, 105189.

Sun, T. & Li, D. (2022). Sign stochastic gradient descents without bounded gradient assumption for the finite sum minimization. *Neural Networks*, *149*, 195–203.

Tambrallimath, V., Keshavamurthy, R., Saravanabavan, D., Koppad, P. G., & Kumar, G. P. (2019). Thermal behavior of pc-abs based graphene filled polymer nanocomposite synthesized by fdm process. *Composites Communications*, *15*, 129–134.

Taylor, D. (2008). The theory of critical distances. *Engineering Fracture Mechanics*, *75*(7), 1696–1705.

Tofail, S. A., Koumoulos, E. P., Bandyopadhyay, A., Bose, S., O'Donoghue, L., & Charitidis, C. (2018). Additive manufacturing: scientific and technological challenges, market uptake and opportunities. *Materials today*, *21*(1), 22–37.

Udd, E. & Spillman Jr, W. B. (2011). *Fiber optic sensors: an introduction for engineers and scientists*. John Wiley & Sons.

Whitney, J. M. & Nuismer, R. J. (1974). Stress fracture criteria for laminated composites containing stress concentrations. *Journal of composite materials*, *8*(3), 253–265.

Wickramasinghe, S., Do, T., & Tran, P. (2020). Fdm-based 3d printing of polymer and associated composite: A review on mechanical properties, defects and treatments. *Polymers*, *12*(7), 1529.

Xu, X., Man, H. C., & Yue, T. M. (2000). Strength prediction of composite laminates with multiple elliptical holes. *International journal of solids and structures*, *37*(21), 2887–2900.

Xu, Y., Zhu, J., Wu, Z., Cao, Y., Zhao, Y., & Zhang, W. (2018). A review on the design of laminated composite structures: constant and variable stiffness design and topology optimization. *Advanced Composites and Hybrid Materials*, *1*, 460–477.

Yang, C., Kim, Y., Ryu, S., & Gu, G. X. (2020). Prediction of composite microstructure stress-strain curves using convolutional neural networks. *Materials & Design*, *189*, 108509.

Yang, L., Li, S., Zhou, X., Liu, J., Li, Y., Yang, M., Yuan, Q., & Zhang, W. (2019). Effects of carbon nanotube on the thermal, mechanical, and electrical properties of pla/cnt printed parts in the fdm process. *Synthetic Metals*, *253*, 122–130.

Yuan, S., Li, S., Zhu, J., & Tang, Y. (2021). Additive manufacturing of polymeric composites from material processing to structural design. *Composites Part B: Engineering*, *219*, 108903.

Zhang, K., Ma, L.-h., Song, Z.-z., Gao, H., Zhou, W., Liu, J., & Tao, R. (2022). Strength prediction and progressive damage analysis of carbon fiber reinforced polymer-laminate with circular holes by an efficient artificial neural network. *Composite Structures*, *296*, 115835.

Zhang, W., Wu, A. S., Sun, J., Quan, Z., Gu, B., Sun, B., Cotton, C., Heider, D., & Chou, T.-W. (2017). Characterization of residual stress and deformation in additively manufactured abs polymer and composite specimens. *Composites Science and Technology*, *150*, 102–110.

Zhang, Y., Liu, T., Lan, X., Liu, Y., Leng, J., & Liu, L. (2022). A compliant robotic grip structure based on shape memory polymer composite. *Composites Communications*, *36*, 101383.

Zhou, X.-Y., Qian, S.-Y., Wang, N.-W., Xiong, W., & Wu, W.-Q. (2022). A review on stochastic multiscale analysis for frp composite structures. *Composite Structures*, *284*, 115132.

Zimmerling, C., Dörr, D., Henning, F., & Kärger, L. (2019). A machine learning assisted approach for textile formability assessment and design improvement of composite components. *Composites Part A: Applied Science and Manufacturing*, *124*, 105459.

Zou, X., D'Antino, T., & Sneed, L. H. (2021). Investigation of the bond behavior of the fiber reinforced composite-concrete interface using the finite difference method (fdm). *Composite Structures*, *278*, 114643.